The Design of a Subtalar Joint Prosthesis Wear Testing Mechanism

by

Jonelle M Jn Baptiste

A thesis submitted in partial fulfillment of the requirements for the degree of

Master of Science

in

Structural Engineering

Department of Civil and Environmental Engineering
University of Alberta

ABSTRACT

The subtalar joint forms part of the triple joint complex in the foot and is primarily responsible for inversion and eversion of the hind foot and ankle. Injury to the subtalar joint typically arises as a result of primary osteoarthritis or sequelae of injury. When non-invasive treatments are no longer a viable option for treatment, subtalar arthrodesis is performed on the joint. Arthrodesis, also known as fusion, entails the removal of existing joint tissue to fuse the mating surfaces of bones. While fusion reduces discomfort, and improves the overall function of the foot and ankle, it totally eliminates joint motion. It is widely known that total joint replacements have been successful in the hip, knee and ankle. However, there have been no publications on the wear testing of subtalar joint prostheses to date. Therefore, there is a need to test the feasibility of subtalar joint prostheses, which will maintain some degree of motion in addition to relieving discomfort. The long-term objective of this study is to develop and apply a testing protocol for wear of subtalar joint prostheses. To date, no protocols exist for wear testing of ankle joint prostheses. Therefore, the ISO standards for wear testing of total hip-joint prostheses forms the basis for developing that of the subtalar joint. The short-term goal is to design and build a wear testing simulator specifically for subtalar joint prostheses and test one pair of potential carbon fiber reinforced polyether-ether-ketone (CFR PEEK) subtalar joint prostheses for wear. While fatigue-testing machines for hip and knee implants exist, they are costly. A four-bar mechanism applies rotary displacement to replicate eversion and inversion while a fatigue tester applies cyclic loading simultaneously. This simulator is optimized to withstand the applied fatigue loading without failure after a minimum of 5 million cycles. To replicate physiological conditions, the implants are submerged in bovine serum diluted with deionized water. Joint implants are typically tested at 1 Hz. However, in the interest of time,

expedited testing at 3 Hz was done in this study. This corresponds to the high loss in mass of the implants tested. As experimental studies on subtalar joint prostheses have not yet been published, the results of this procedure will allow future persons interested in continuing this research to determine how the setup can be improved and which materials will be best suited for use as subtalar joint prostheses.

DEDICATION

In loving memory of my grandfather,
Earl Lindsay,
the biggest higher education enthusiast in my life.
Without his unfailing willingness to help all his grandchildren
no matter the cost,
I would not have been where I am today.
I am eternally grateful to you.

To:
My grandmother,
My parents,
My brothers,
My sister,
And the newest addition to our family -
Jhanai

"Being confident of this very thing, that he which hath begun a good work in you will perform it until the day of Jesus Christ."
Philippians 1:6

ACKNOWLEDGEMENTS

First and foremost, I would like to thank God for blessing me with this opportunity and giving me the grace that I needed to overcome some of the most difficult situations in my life these last two years. I would like to thank my mother, Lucia, for staying up with me every late night and encouraging me relentlessly. If I ever become a mother, I hope that I will be all that you are to me, to my children. Thanks to my father, John, for always praying for me and being there for me. My siblings, Jonathan, Jovan, Jacqui and Jade, thank you for always being there. I hope that you all do not give up on your dreams. It is never too late. Jovan, thank you for Jhanai. She is the one who puts 90% of all the smiles on my face.

A warm thank you goes out to all the friends and family that I had before I came to Edmonton and all those who entered my life since then. You all have been such a blessing to me. Thank you for extending your time, patience, and most importantly, kindness, towards me. It humbles me to know how much you all would sacrifice for me. If it weren't for Keller George, I would not have been as prepared as I was for my research and defense. A special thank you goes out to Andy, who encouraged me to pursue this degree in the first place and never hesitated to offer help when it was needed.

I would not have been able to turn my project into a reality without the help of Andrew Wong, Joseph Sabbagh, Stephen Andrews, the guys from the MecE Shop (Roger, Dan and Andrew), Greg and Cameron from the I.F. Morrison Structures Lab, Stefan James, Tao Liu and Carlos Darder. Thanks to Leila Laouar for assisting me at the last minute and always accommodating me. A big thank you goes out to all the students who helped me with testing, especially Ibrahim El-Jabali who always availed himself no matter what day or time it was.

I would like to thank my supervisors, Dr. Samer Adeeb and Dr. Nadr Jomha, for their support and imparting their wisdom upon me throughout this research. Thank you, Samer, for accepting me as your student. If you did not challenge and push me, I would not know what I am capable of. You possess all the qualities of an exemplary supervisor and never hesitated to lend a hand in times of need. I would also like to thank Dr. Douglas Tomlinson for agreeing to be a part of my examining committee.

Funding for this research is provided by the National Sciences and Engineering Research Council of Canada (NSERC) and the Edmonton Orthopaedic Research Committee.

TABLE OF CONTENTS

LIST OF FIGURES

LIST OF TABLES

Chapter 1 Introduction

1.1 Problem Statement

The subtalar joint is the articulation between the talus and calcaneus bones of the hind foot, below the true ankle joint. Its main function is to assist the foot and ankle with stability on uneven surfaces and side-to-side motion, scientifically termed inversion and eversion. To date, the standard method of treatment available for severe injury to the subtalar joint is subtalar arthrodesis. With this procedure, the existing joint tissues are removed and the surfaces of the talus and calcaneus bones are fused together to heal as a unit (American Orthopaedic Foot & Ankle Society, n.d.). While this procedure alleviates pain, it eliminates the articulation of the joint. There have been successful cases of total joint replacement of the ankle (Prissell et al, 2017), hip and knee. Therefore, there is a need to create and test prostheses for the subtalar joint to maintain some motion in addition to alleviating the pain of injury.

By replicating the surfaces of the talus and calcaneus bones, a design for subtalar joint prostheses can be made (Figure 1-1). Suggested materials which can be used for such implants include polyether-ether-ketone (PEEK), carbon fibre reinforced polyether-ether-ketone (CFR PEEK), and ultra-high molecular weight polyethylene (UHMWPE). These materials have been used for total hip and ankle replacements. Wear testing will determine which material is best suited for subtalar joint prostheses *in vivo*.

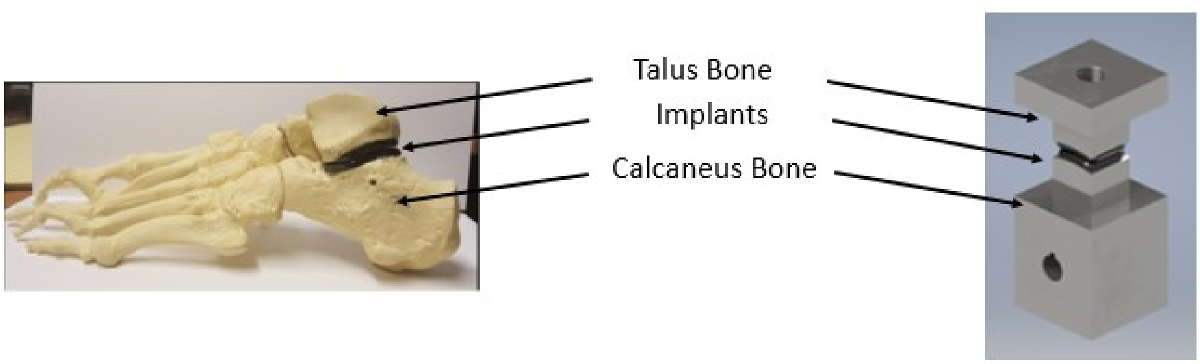

Figure 1-1: Proposed design for subtalar joint prostheses

Presently, there are no standards for wear of ankle joint prostheses. Therefore, the standards for wear of total hip-joint prostheses (ISO 14242-1 & 2) can be modified to suit the kinematic loading conditions of the subtalar joint. For total hip-joint replacement, the applied load is described by a fourth order polynomial ranging from 300-3000 N (Figure 1-2). The displacement follows a different sinusoidal curve for inward/outward rotation, abduction/adduction and flexion/extension. The subtalar joint is mainly responsible for eversion/inversion, which is comparable to the inward/outward rotation of the hip joint. While researchers have found it difficult to establish a standard force pattern for the ankle joint, the load is typically four to seven times that of body weight (Pal & Roupal, 1998). With this information, parameters for practical loading and rotary displacement for the subtalar joint can be determined. While there are machines specifically created for testing implants for wear, this thesis focuses on the creation of a more cost-effective option that replicates the motion of the subtalar joint.

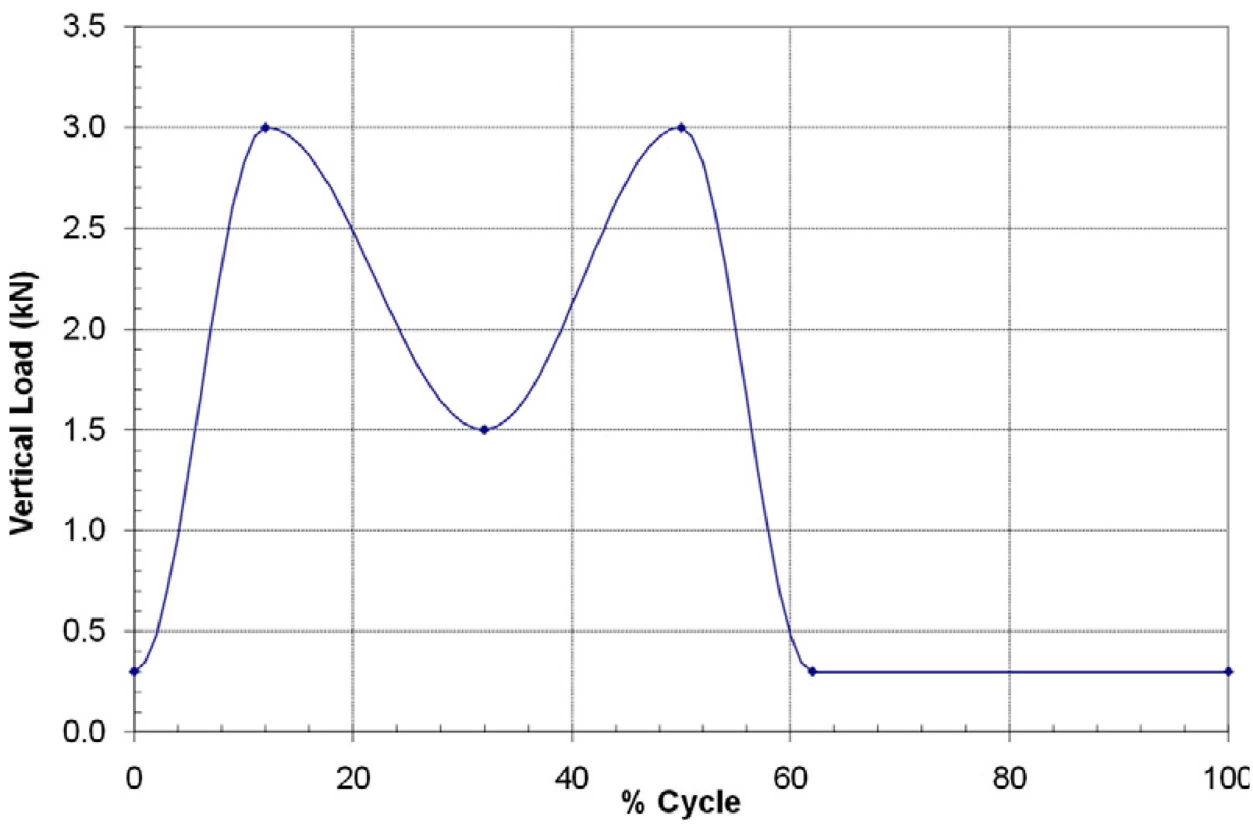

Figure 1-2: Hip joint loading as per ISO 14242-1 (Bandhyopadhya & Bose, 2013)

1.2 Objectives

The main objective of this thesis is to create a subtalar joint prosthetic that is durable and able to maintain some degree of motion. This will be done by testing the applicability of carbon reinforced polyether-ether-ketone (PEEK) as a surface reconstruct for the facets of the talus and calcaneus bones which form the subtalar joint.

Objective 1: Design an apparatus which enables rotary displacement and can be easily detached from a fatigue testing machine (*Bose ElectroForce 3510 Test Instrument*).

Specific aim 1: Create 3D models of different designs for rotary displacement mechanisms. Use the design criteria to select the best mechanism for the experiment.

Specific aim 2: Design the mechanical components, and verify that the required rotary displacement is achieved. Use Finite Element Analysis (FEA) to verify that the mechanism will not fail from fatigue.

Specific aim 3: Select the required electrical components and verify the torque required using FEA.

Specific aim 4: Build the apparatus and test it to ensure that it will work before testing with the actual implants.

Objective 2: Perform wear testing on CFR PEEK subtalar joint prostheses

Specific aim 1: Subject one pair of subtalar joint implants to wear for 4 million cycles in 20 g/l bovine serum diluted with deionized water.

Specific aim 2: Observe the surfaces of the implants, measure the roughness and the mass lost after every 0.5 million cycles, 1 million cycles, and every 1 million cycles until the completion of testing.

1.3 Limitations

While the subtalar joint is mainly responsible for eversion/inversion of the foot and ankle, this is not the only articulation provided by this joint. In addition, the compressive load used is very small in comparison to the forces felt by the ankle joint during normal gait, approximately five times the body weight. Thus, the rotary displacement and sinusoidal load that the implants are subjected to in this experiment do not replicate the true loading conditions that the implants will be subject to *in vivo*. Future studies should look into subjecting these implants to a load pattern that is more akin to the true kinematic loading of the subtalar joint during gait.

The test rig also presented different issues with each test. Manufacturing errors such as the misalignment of holes resulted in the unprecedented premature failure of some mechanical parts. Thus, there were delays between testing for repairing failed parts. Delays could have affected the change in mass of the implants. Finally, a loaded non articulating control specimen was not tested since there is only one fatigue-testing machine available.

1.4 Research Contribution

The findings of this research is the first step towards the implementation of subtalar joint prostheses in orthopaedic surgery. Adults and athletes form the consensus of people who typically incur severe injury to the subtalar joint. These persons will now be presented with the option of having a joint replacement surgery instead of subtalar arthrodesis only; the long term goal of this study. Their quality of life would be greatly improved since this joint is responsible for stability of the foot on uneven surfaces during gait. The development of a subtalar joint wear testing simulator offers a more affordable solution for wear testing of these specialized prostheses instead of the wear testing simulators readily available on the market.

While numerous studies have been carried out on hip and knee joint prostheses, there still needs to be more work done to improve the long term outcome of total ankle replacements. Literature confirms that there have been no published articles on wear testing of subtalar joint prostheses to date. Thus, this research revolves around the wear testing of a novel product. The findings of this study will be submitted to a peer-reviewed journal.

1.5 Outline of Thesis

This thesis consists of eight chapters.

Chapter 1

This chapter introduces the reader to the content of this thesis. The problem statement, objectives, limitations, contribution to the field of research and a summary of each chapter thereafter is provided.

Chapter 2

Background information on the function of the subtalar joint, subtalar arthrodesis and subtalar fusion is provided in this chapter. Previous studies that tested for wear of other joint prostheses such as the ankle, knee and hip are reviewed and the loading conditions best suited for the subtalar joint are determined.

Chapter 3

A detailed discussion of the concepts behind the design of the mechanical and electrical components of the test rig are covered in this chapter. Instructions for assembly of the mechanism are also provided.

Chapter 4

Finite element analysis of the rotating mechanism in the test rig is conducted to properly size some of its components designed in Chapter 3. This is necessary to ensure that none of the parts fail from fatigue and that they can withstand the total duration of testing. The size of the motor required to drive the experiment is also determined.

Chapter 5

In this chapter, the traditional method for selecting the size of the motor is performed to validate the results from FEA in Chapter 4. The angular displacement of the linkages is also validated.

Chapter 6

The wear testing method used for the experiments carried out is fully described in this chapter. This encompasses the preparation of the immersion fluid, conditioning of implants for testing, operation of the machine, methods to prepare the implants for wear analysis, and the methods used for wear analysis. Details of the equipment used for wear analysis are also provided.

Chapter 7

The results after wear testing are presented in this chapter. It includes observations made by the researcher, comments on the performance of the machine, images of the mating surfaces of the implants, the mass lost and roughness measurements after each stage of testing.

Chapter 8

A summary of the design and experimental findings of this thesis are summarized in this chapter. Conclusions are drawn and recommendations for future improvements to the design of the test setup are suggested.

Chapter 2 Literature Review

2.1 Diarthrodial Joints

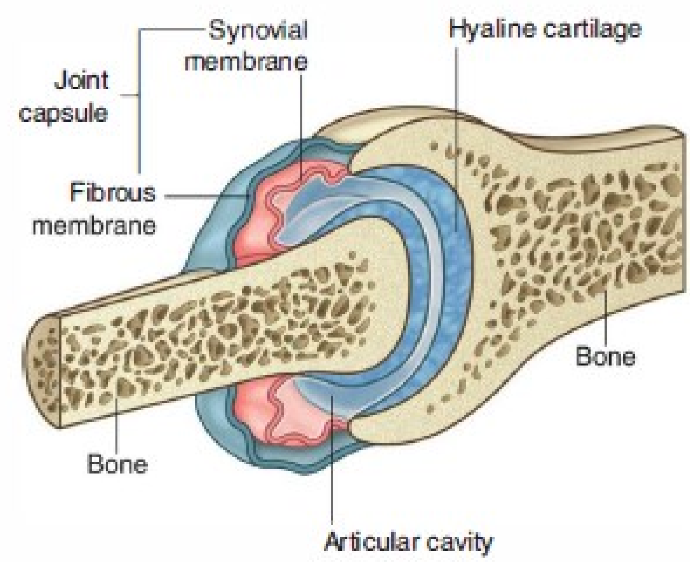

Figure 2-1: Diarthrodial joint (Drake et al, 2014)

Diarthrodial joints (Figure 2-1), also known as synovial joints, are points of contact between two bones. The bones involved are never in direct contact with each other. Instead, these bones are separated by a narrow articular cavity. At the articulating ends of each bone is a layer of articular cartilage, usually hyaline cartilage. Articular cartilage is a soft, white, dense connective tissue. It is necessary to transmit forces between the bones and reduce friction. This is confirmed by the gap seen between bones in radiographs (Drake et al, 2014).

A two-layer joint capsule encloses the ends of the articulating bones. The outer layer is a fibrous membrane and the inner layer is a synovial membrane. The function of the synovial membrane is to enclose the articular cavity and produce synovial fluid, which is vascular in nature. Synovial fluid fills the articular cavity and provides lubrication for the articulating surfaces. There may also be occurrences of closed sacs of synovial membrane, which form synovial bursae or tendon sheaths, outside synovial joints. Both bursae and tendon sheaths are responsible for reducing friction from one structure over the surface of another (Drake et al, 2014).

The fibrous membrane is comprised of dense, connective tissue and is responsible for stabilizing the joint. Some parts of the fibrous membrane thicken and result in the formation of ligaments. Ligaments are innervated, therefore they are able to sense strain felt by the joint. They are also responsible for stabilizing the joint. Further reinforcement is provided by restraining the motion of one bone relative to another. Due to the abundant supply of blood to ligaments, minor injuries to some ligaments can be repaired (Adeeb, 2005). Other components of some synovial joints include articular discs, fat pads and tendons. These may be found within the area inside the joint capsule or the synovial membrane.

Synovial joints can be uniaxial, biaxial or multiaxial depending on the geometry of the joint. These joints can be further classified into seven types based on the shapes of their articulating surfaces. These are plane (flat), hinge, pivot, bicondylar, condylar (ellipsoid), saddle, and ball and socket joints (Figure 2-2). Table 2-1 summarizes the function and an example of each type of synovial joint.

Table 2-1: Types of Diarthrodial Joints

Joint Type	Function	Example
Plane (Flat)	Provides sliding or gliding movements of one bone across the surface of another	Acromioclavicular joint
Hinge	Allows for flexion and extension about one axis that runs transversely through the joint	Elbow joint
Pivot	Permits rotation about one axis that runs longitudinally along the shaft of the bone	Atlanto-axial joint
Condylar (Ellipsoid)	Allows flexion, extension, abduction, adduction, and limited circumduction around two perpendicular axes	Wrist joint
Bicondylar	Permits the majority of movement about one axis and limited rotation about a second axis. This motion is as a result of two convex condyles articulating with concave or flat surfaces	Knee joint
Saddle	Permits flexion, extension, abduction, adduction and circumduction about two perpendicular axes	Carpometacarpal joint of the thumb
Ball and Socket	Allow flexion, extension, abduction, adduction, circumduction and rotation about multiple axes.	Hip joint

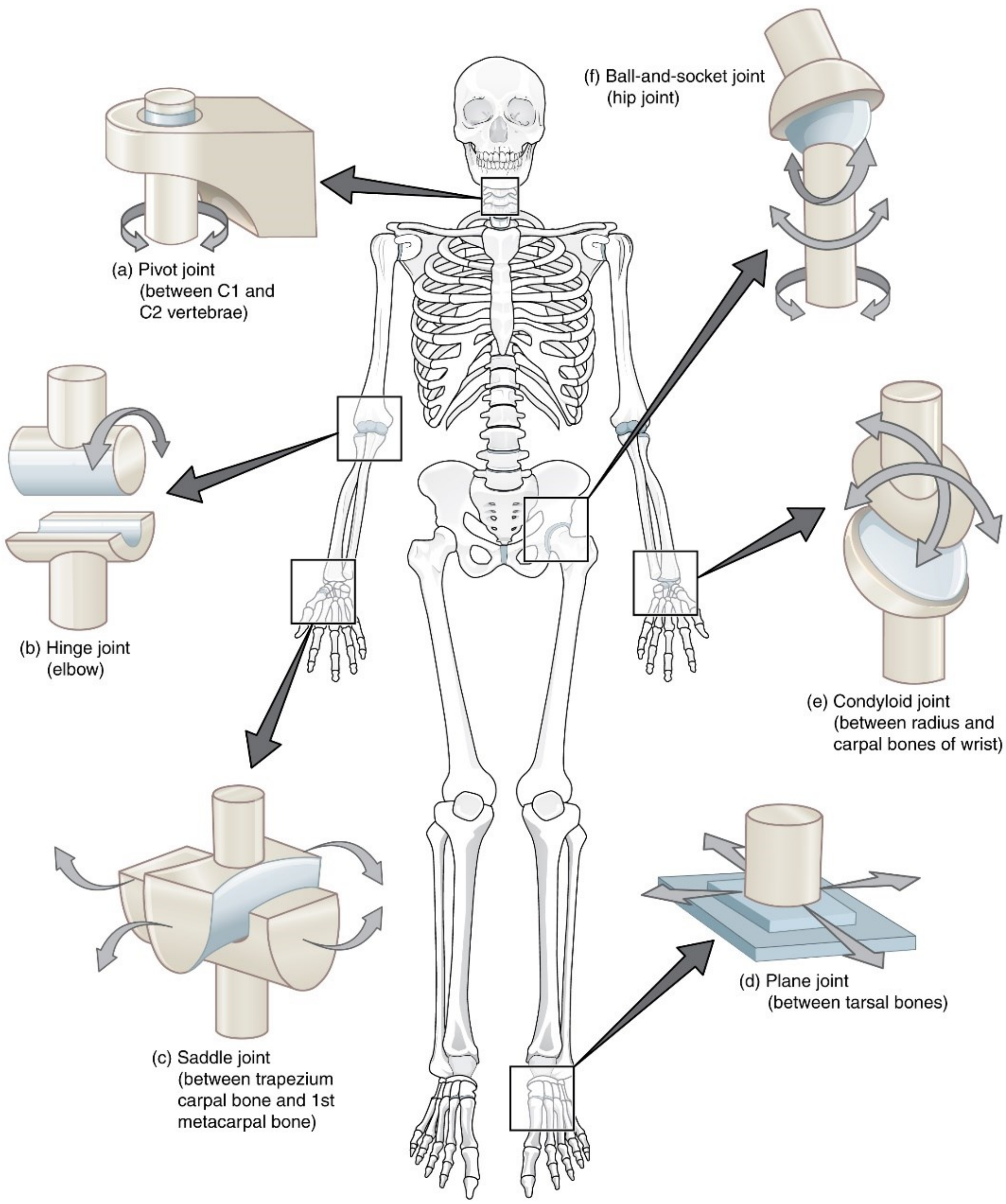

Figure 2-2: Types of diarthrodial joints (cnx.org)

2.2 The Foot and Ankle

The bones of the foot fall under three divisions; the tarsal bones, metatarsals and phalanges (Figure 2-3). Tarsal bones consist of seven bones that are in two rows with an intermediate bone between the two rows that is located on the medial side. Joints between the tarsal bones are primarily responsible for eversion and inversion of the foot and ankle. The tarsal bones articulate with the metatarsals at tarsometatarsal joints, allowing limited sliding motion only (Drake et al, 2014).

The metatarsals are restricted from independent motion by ligaments that connect the distal heads of the bones at the metatarsophalangeal joints. Each digit is connected to a metatarsal bone, and each digit has three phalanges except for digit I, which has two. Metatarsophalangeal joints allow flexion, extension, abduction and adduction of the digits. Interphalangeal joints effectively act as hinge joints and allow flexion and extension (Drake et al, 2014).

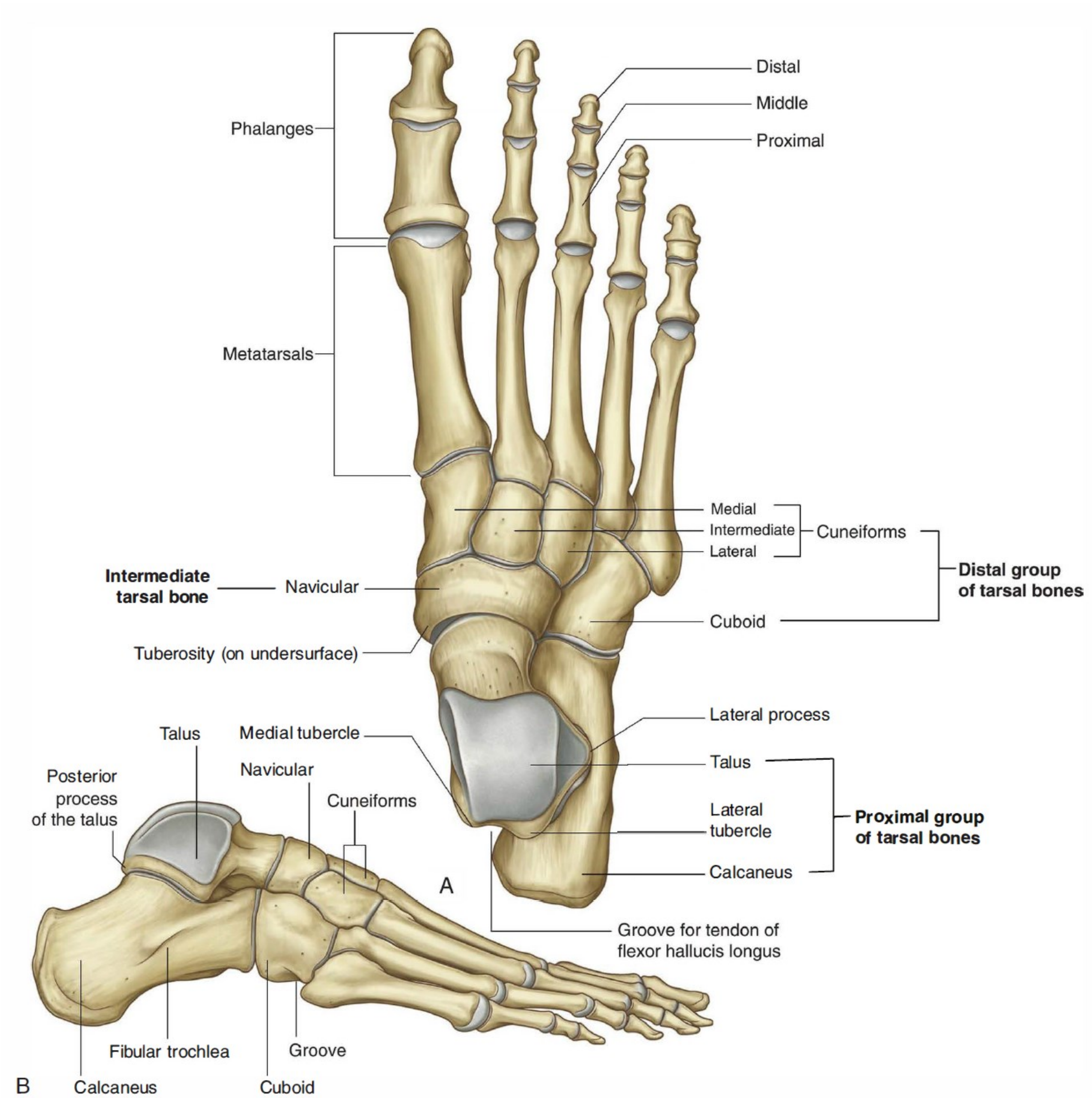

Figure 2-3: Bones of the foot A. Dorsal view, B. Lateral view of the right foot. (Drake et al, 2014)

2.3 The Subtalar Joint

The third edition of Gray's anatomy for students (2014) defines the subtalar joint as the articulation between the large posterior calcaneal facet on the inferior surface of the talus and the corresponding posterior talar facet on the superior surface of the calcaneus (Figure 2-4). A layer of synovial membrane, which is below a fibrous membrane, encompass the articular cavity of the subtalar joint. Ligaments including the lateral, medial, posterior and interosseous talocalcaneal ligament support the joint. This joint is primarily responsible for eversion and inversion of the foot and ankle and allows gliding and rotation. Inversion and eversion is done in conjunction with the talocalcaneonavicular and calcaneocuboid joints. Since these joints have a common axis of motion, the motion of these joints are congruent (Rockar, 1995). The range of motion of the subtalar joint is critical to the normal function of the hindfoot as it also enables the foot to adapt to irregular surfaces.

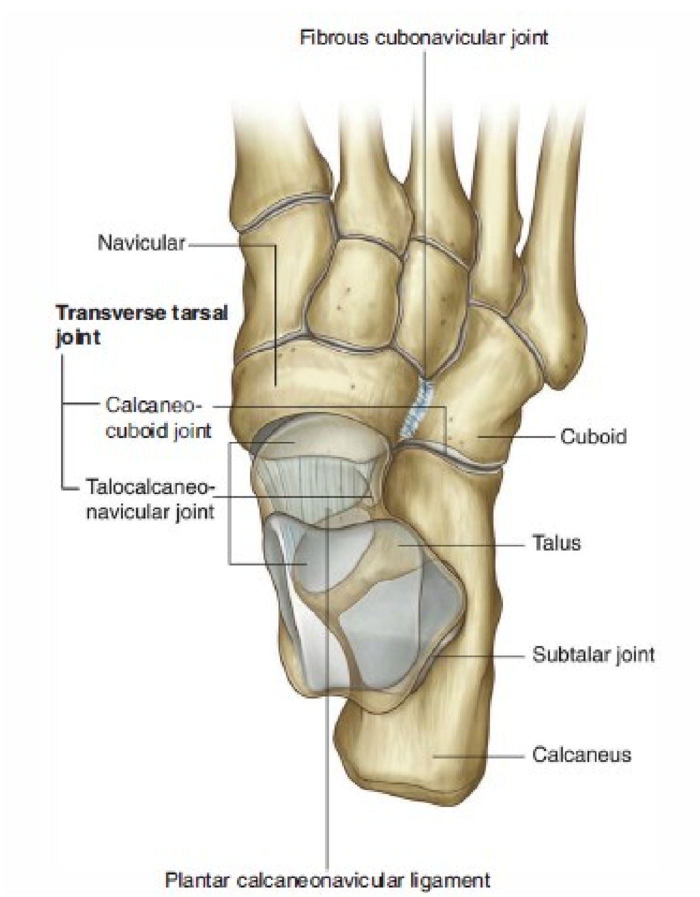

Figure 2-4: Intertarsal joints (Drake et al, 2014)

2.3.1 Components of the Subtalar Joint

2.3.1.1The Talus

Due to its many functions, the talus (Figure 2-5) acts as the mechanical keystone of the foot (Rockar, 1995). The talus is a small, irregularly shaped bone that resembles a snail when viewed medially or laterally (Drake et al, 2014). This bone is critical to the ankle joint since it controls the motion and interaction of the ankle and subtalar complex joints (Early, 2008) (Kapandji, 2011). Apart from controlling the motion of the hindfoot, the talus is also responsible for weight distribution over the entire foot (Chi and Schmitt, 2005) (Mahato and Murthy, 2012). More than half of its surface is covered with articular hyaline cartilage (Rockar, 1995). The talus consists of a rounded head, short broad neck and an expanded body. The articulating surfaces on this bone are responsible for interactions with the tibia and fibula, calcaneus and navicular (Drake et al, 2014).

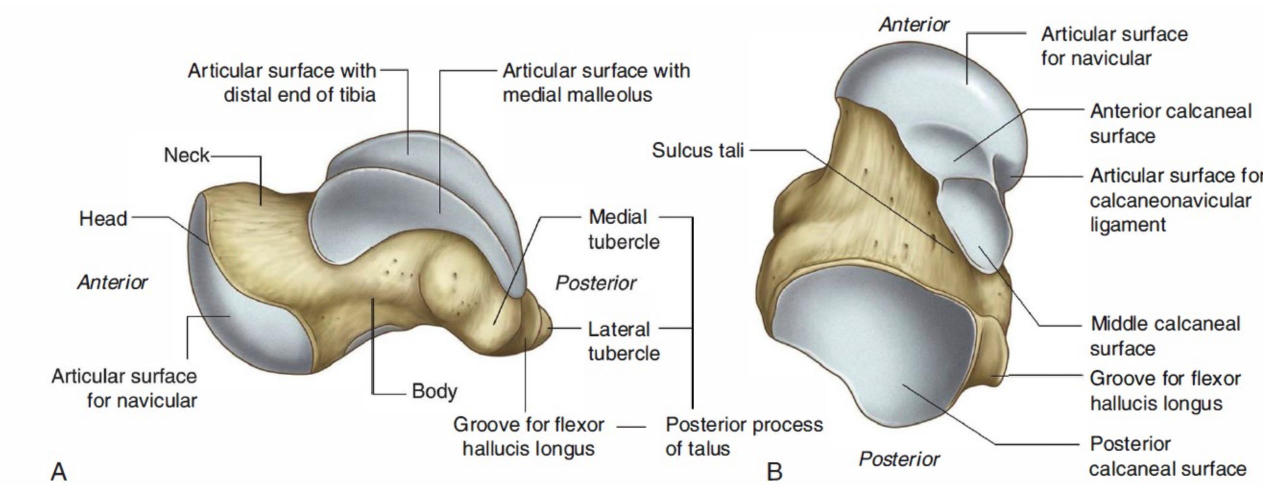

Figure 2-5: Medial (A) and inferior (B) views of the talus (Drake et al, 2014)

The talus has no muscular attachment and is sustained by blood vessels from ligament insertions and a few direct blood vessels. This blood supply is just adequate under regular conditions, so talar fractures can compromise it and result in pseudarthrosis or avascular necrosis (AVN) (Kapandji, 2011).

2.3.1.2 The Calcaneus

The calcaneus (Figure 2-6) is the largest of the tarsal bones. It known as the heel bone and is responsible for supporting the talus and transferring the majority of body weight from the talus to the ground (Martini, Timmons and Tallitsch 2006). This is an irregular, box shaped bone with six surfaces – superior, inferior, medial, lateral, posterior and anterior. The medial and anterior surfaces provide the facets for articulation with the talus and cuboid. Articulation with the cuboid occurs at the anterior surface of the calcaneus, which is the smallest of the six surfaces (Rockar, 1995). The medial surface has a shelf of medial bone projection called the sustentaculum tali, which supports the posterior portion of the talus. On the superior surface of the sustentaculum tali is a facet for articulation with the talus, the middle talar articular surface. However, the anterior and posterior talar articular surfaces are directly on the superior surface of the calcaneus (Drake et al, 2014).

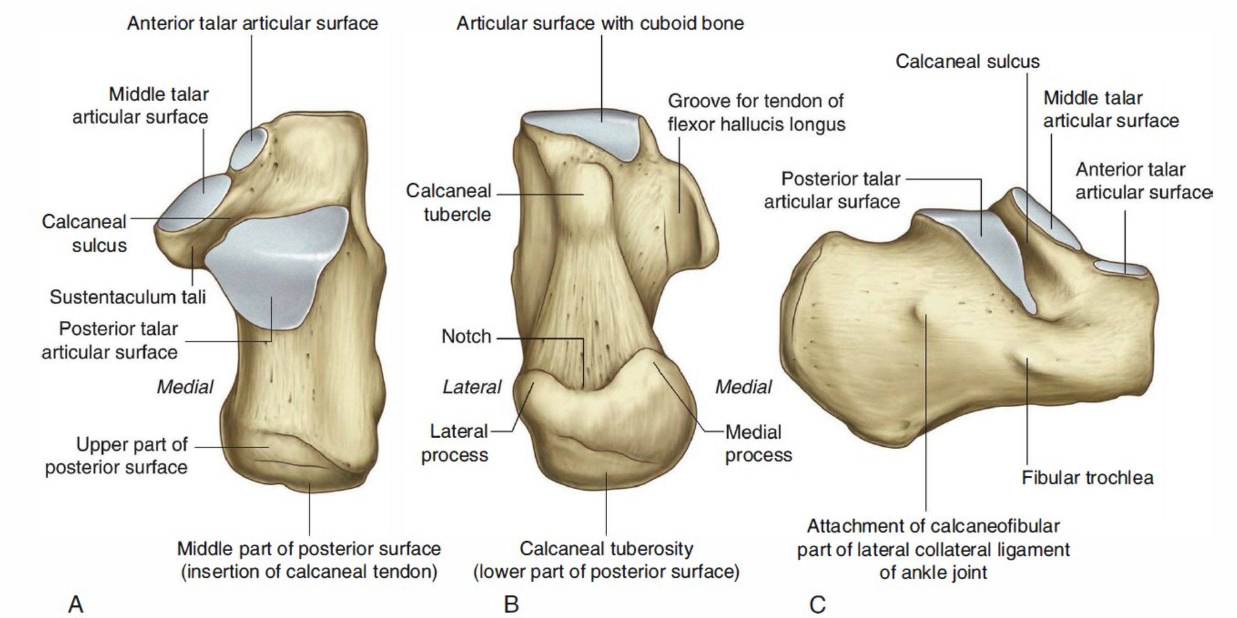

Figure 2-6: Superior (A), inferior (B) and lateral (C) views of the calcaneus (Drake et al, 2014)

2.4 Injury

Injuries to the foot and ankle come about because of birth deformities, sequelae of injury or arthritis to name a few. The types of arthritis that most commonly affect the foot and ankle are osteoarthritis, posttraumatic arthritis and rheumatoid arthritis. Dislocations and fractures typically observed in the young, active population, lead to posttraumatic arthritis. With posttraumatic arthritis, cartilage between joints are worn out and cause debilitating pain. Injury to a joint increases the chances of it becoming arthritic. Statistics point towards the talus and calcaneus having the highest occurrence of fractures among all tarsal bones (Bhandari and Adili, 2011).

Like posttraumatic arthritis, osteoarthritisis is a result of wear of the cartilage between joints. It may occur in both the middle age and young adult population. Obesity and family history may also put a person at risk for developing osteoarthritis (Sellam & Berenbaum, 2013). Reduction in the layer of cartilage causes bones to rub against each other and form osteophytes. Rheumatoid arthritis is an autoimmune disease that is typical of the older population. It often affects joints of the foot and ankle initially and may attack multiple joints throughout the body. This type of arthritis entails the immune system attacking the synovial layer of joints and results in swelling and deformity of the joint (Aaos.org).

2.5 Current Treatment

Depending on the level of progression of arthritis, both non-invasive and surgical methods are available to alleviate the pain of arthritis. Non-invasive techniques include physiotherapy, the use of braces and foot inserts and anti-inflammatory drugs. Surgical techniques include arthroscopy, arthrodesis and arthroplasties of the ankle joint. The most common surgical option in caring for arthritis of the subtalar and joint is arthrodesis (fusion). In this procedure, any existing cartilage is removed and the articulating surfaces of the ankle or subtalar joints are fused together (Figure 2-7). Although arthrodesis alleviates pain, the procedure eliminates the motion and normal function of the joint (Barton, Lintz and Winson 2011) (Haddad, et al. 2007). In the case of subtalar arthrodesis, the ability to walk on uneven surfaces is affected and degeneration of the joint may occur (Yang et al, 2016).

Figure 2-7: Subtalar arthrodesis (Ziegler et al, 2017)

There have been successes with ankle arthroplasties, which have become the preferred alternative to arthrodesis (Gougoulias et al, 2013). Arthroplasties restore some joint function and improve the overall quality of life. However, revision surgeries may be required as implants are prone to failure from loosening for example. When fractions of the talus bone result in avascular necrosis, an arthroplasty is not a viable option since the talus bone is not healthy enough to attach prostheses to it. To date, subtalar joint arthroplasties have not been explored.

2.6 Arthroplasties of the hip, knee and ankle

Literature indicates that there have been significant successes in arthroplasties of the hip, knee and ankle. Approximately 80% of ankle arthroplasties have reported a survival rate of 10 years (Gougoulias et al, 2010). Hip and knee arthroplasties have been in existence long before that or ankle arthroplasties and have a higher survival rate.

2.6.1 Hip

Studies show that total hip arthroplasties (THA) have a survival rate of more than 95% after 10 years and more than 80% after 25 years (Pivec et al, 2012). As the hip joint is a ball and socket joint, the implants used for a total hip replacement are typically of the same nature. Standard implants consist of a femoral head articulating against an acetabular cup (Figure 2-8). Wear tests have been carried out on various materials for the femoral head. These include a metal alloy such as CoCr, alumina, zirconia (Wang et al, n.d.) or ceramic material (Brockett et al, n.d.). The acetabular cups are synthesized from a plastic such as polyethylene or variations of PEEK (Scholes et al, 2007) (Chyr et al, 2014).

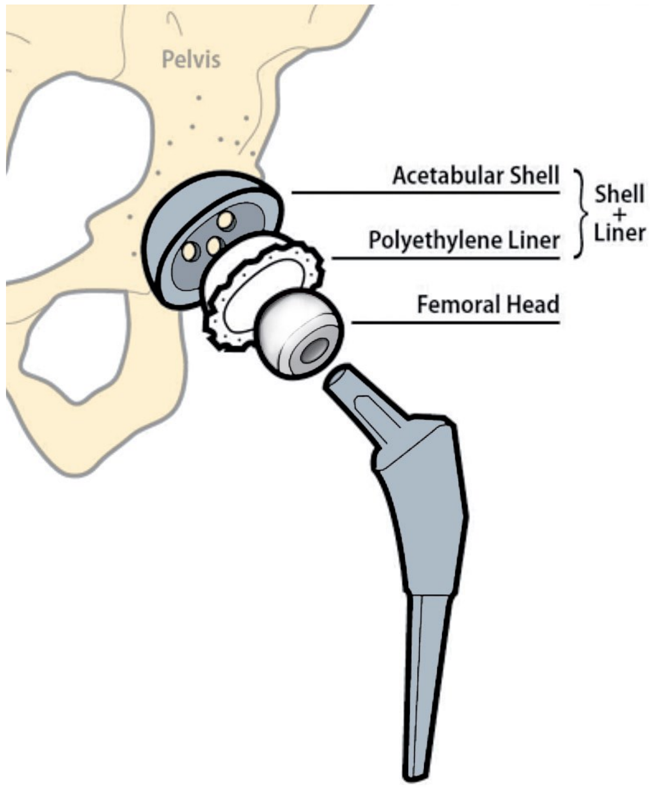

Figure 2-8: Schematic of a total hip replacement (Nebergall et al, 2015)

Figure 2-9: Alumina femoral head (left) and CFR PEEK acetabular cup (right) (Scholes et al, 2008)

Studies indicate that failure of a THA is greatly attributed to osteolysis (Scholes et al, 2008). Therefore, studies continue to be carried out to determine the best materials with the best resistance to wear. This may be done by either strengthening the polymer used by the acetabular cup or eliminating contact between the joints. The latter approach may be achieved by using metal-on-metal articulation instead. However, concerns have been made about the effect of the deposit of metal ions in the blood stream on the patient's health (Brodner et al, 2003). In addition to metal-on-metal, other combinations of bearing surfaces such as metal-on-ceramic and ceramic-on-ceramic are being tested for higher rates of long term survivorship. Techniques such as resurfacing arthroplasty are also being explored (Pivec et al, 2012).

2.6.2 Knee

Depending on the extent of osteoarthritis of the knee, one or more compartments of the knee may be affected. Initially, total knee arthroplasty (TKA) was developed for the treatment of advanced osteoarthritis of the knee (Figure 2-10). Advances in knee arthroplasties have allowed the development of prostheses for a unicondylar knee arthroplasty (UKA) in the event that the function of only one compartment of the knee is compromised (Figure 2-12). This condition is known as intra-articular unicompartmental osteoarthritis. UKA is preferable to TKA since it is less invasive and preserves the healthy compartment of the knee. UKA also provides a better range of motion and requires a shorter recovery time (Scholes and Unsworth, 2008). Solutions for UKA include unicondylar knee implants typically which consists of a tibial component and a meniscus (Figure 2-11) or an interpositional knee spacer (Figure 2-13). Unlike unicondylar knee implants, knee spacers aim at replacing the meniscus of the knee joint, thereby eliminating the need for bone resection. They are either prefabricated or specifically designed for each patient (Goetz et al, 2017).

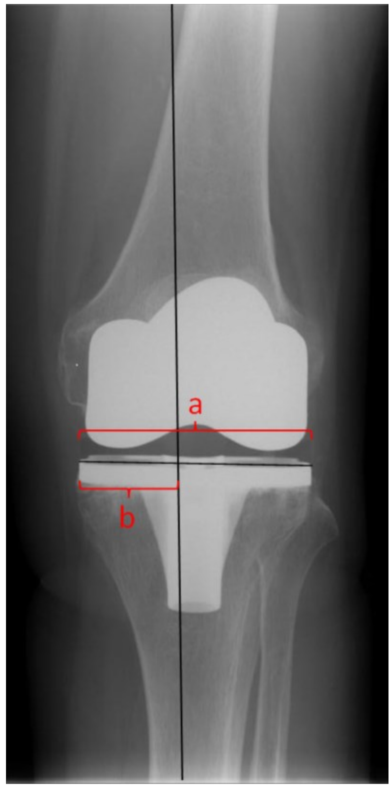

Figure 2-10: NexGen Legacy Posterior Stabilized Fixed Bearing Knee System for a TKA (Nishikawa et al, 2014)

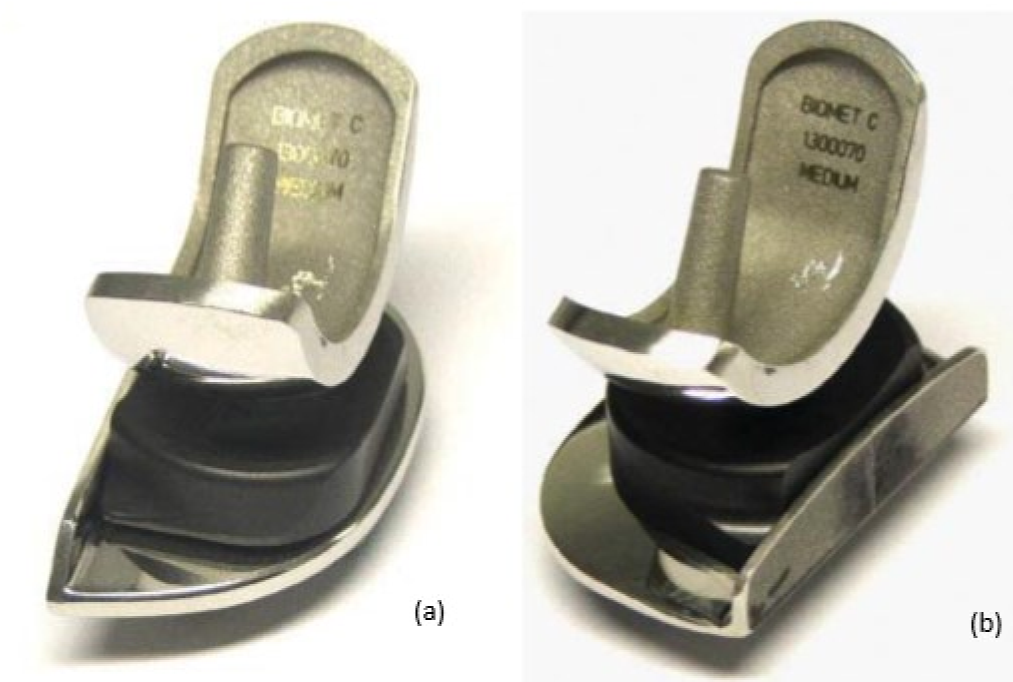

Figure 2-11: Unicondylar mobile knee bearings: medial component (Left) and lateral component (Right) (Scholes and Unsworth, 2008)

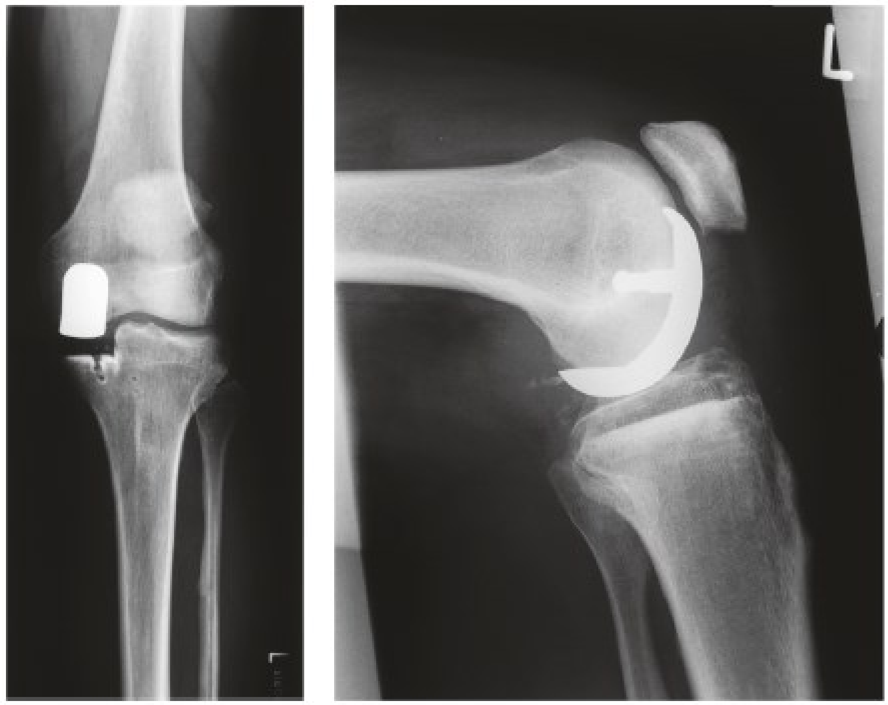

Figure 2-12: Anteroposterior and lateral radiographs of post-operative unicompartmental knee (Goetz et al, 2017)

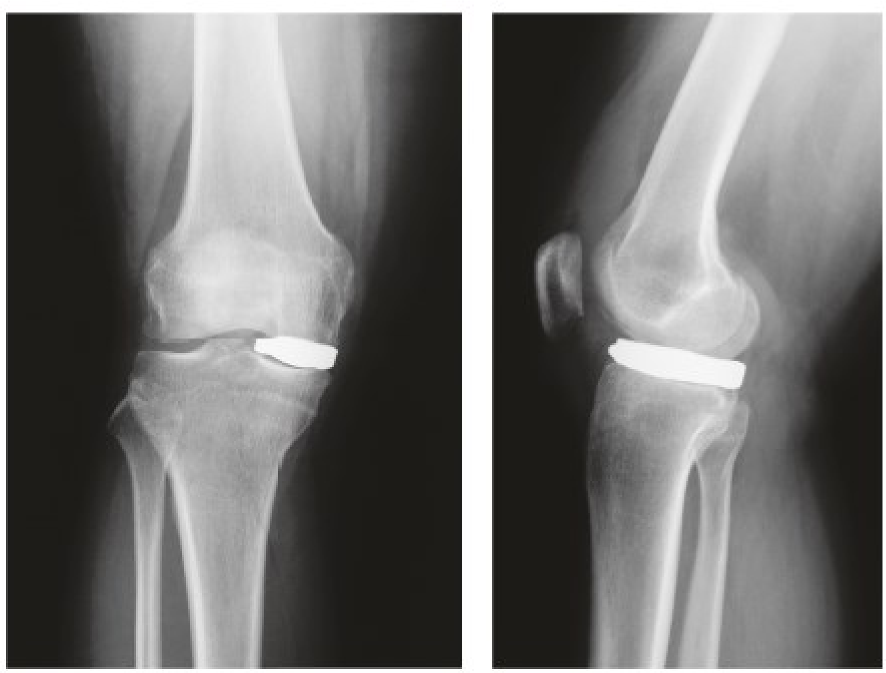

Figure 2-13: Anteroposterior and lateral radiographs of post-operative interpositional knee device (Goetz et al, 2017)

Clinical results show that 95% of patients who use unicondylar knee implants report a success outcome after 10 years (Price et al, nd). Lyons et al (n.d.) compared the survival rate of patients who had a TKA with a UKA. While the survival rate of TKA was higher, patients preferred UKA. Implants of various materials and shapes are readily available on the market for a TKA or UKA. TKA implants such as the total knee system manufactured by Sigma (DePuy, Warsaw, IN, USA) are typically made from a metal alloy such as Co-Cr and a polyethylene meniscus. The tibial or femoral component of a unicondylar knee implant can be made from either a metal alloy such as Co-Cr-Mo or plastic. On the other hand, the meniscus is mobile and made from a plastic such as UHMWPE and PEEK (Scholes and Unsworth, 2008). Knee spacers such as the ones manufactured by iForma (ConforMIS, Burlington, MA, USA) can also be made from a metal alloy such as Co-Cr-Mo.

2.6.3 Ankle

According to literature, Eloesser was the first to perform an alternative surgery to an ankle arthrodesis in 1913 (Eloesser, 1913). His method involved the transplantation of an ankle cartilage allograft. However, Lord and Marrotte made the first attempt at a total ankle replacement in 1970. By completely removing the talus, a long stem metallic component was implanted in the tibia and made to articulate with an acetabular cup fixed to the calcaneus bone. For this reason, the prosthesis was termed a "reverse hip" implant. Unfortunately, this procedure was discontinued due to its high failure rate (Lord et al, 1980).

From the 1970's until now, total ankle replacements (TARs) have evolved from two-component implants with cement fixation to three-component implants with either mobile or fixed bearings (Gougoulias et al, 2013). Two-component implants typically consisted of a polyethylene tibia and a metal talus. The implants were fixed to the bones using polymethyl methacrylate cement. Three-component implants came about as researchers discovered the need for a UHMWPE meniscus between the tibial and calcaneal components in the early 80's (Figure 2-14). The meniscus was either fixed to one of the implants or mobile. Designs that incorporated the fixation of the meniscus to one of the implants acted as two components. Results that are more favourable were obtained when the implants were less constrained. Consequently, surgeons discontinued the use of polymethyl methacrylate cement (Gougoulias et al, 2013).

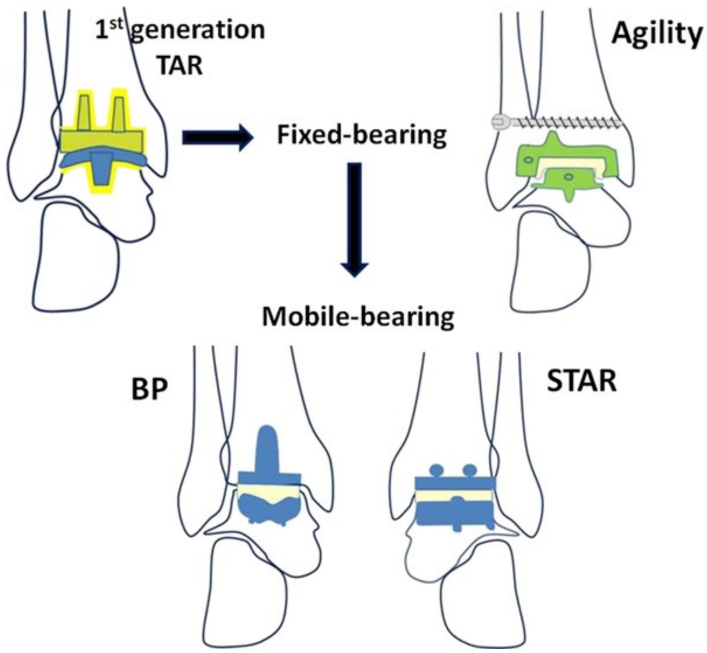

Figure 2-14: Evolution of TAR implants (Gougoulias and Maffoulli, 2013).

To date, the metallic components of most ankle implants are made of a cobalt-chromium alloy. However, surgeons in Japan use ceramic prostheses (Takakura et al, 2004). As research continues, the goal is to find the best product and method of implantation that minimizes bone resection, minimizes friction of the meniscus, induces bone ongrowth and reduces aseptic loosening to name a few (Gougoulias et al, 2013). While the design of ankle joint prostheses has improved over the last 40 years, the failure rates are still twice as much as hip and knee joint prostheses (Labek et al, 2011) (Deland et al, 2000). Two-component implants are still in use today. However, three-component implants with mobile bearings are proving to have a more favorable outcome (Gougoulias et al, 2013).

2.7 Wear Testing

2.7.1 Standards

Standards such as ISO 14242 and 14243 exist for the wear testing of total hip and knee joint prostheses respectively. As such, studies confirm the success of knee and hip simulators at predicting the wear performance of their respective prostheses (Reinders et al, 2015a). However, some researchers have chosen to use loading patterns based on the forces and kinematic loading of the hip joint, for example (Wang et al, n.d.). Since standards for wear testing of total ankle replacements still do not exist, some researchers such as Reinders et al (2015a) have developed suitable loading patterns for the ankle during gait. For a healthy ankle joint, the maximum reaction force is reported to range from four to seven times body weight (Pal & Routal, 1998). On the other hand, the implanted joint will withstand less load than the healthy joint.

2.7.2 Test Procedures

Wear testing simulators for hip and knee prostheses are readily available on the market. Reinders et al, (2015a) and Affatato et al, (2007) modified knee wear simulators to accommodate loading conditions for ankle joint prostheses. As per ISO 14242-1 and 14243-1, fatigue testing is typically carried out at 1 ± 0.1 Hz. Expedited wear testing at 25.3 Hz has been performed using a pin-on-disc device which simulated the wear mechanisms of total hip-joint prostheses. The wear rate was lower per million cycles in comparison to running the tests at 1 Hz. However, the wear mechanisms at both speeds were similar. The success of this expedited testing is attributed to keeping the sliding velocity as close as possible to the values obtained from biomechanical studies (Saikko, 2017).

Accelerated testing distorts the test conditions since the generation of heat from friction forces increases the growth of precipitate of the bovine serum which may form a layer between the articulating surfaces and result in a lower wear rate (Saikko, 2017). There have been published cases where testing was carried out at 2 Hz using a pin-on disk simulator (Bragdon et al, 2001) and a hip simulator (Bragdon et al, 1996). In these cases, UHMWPE samples were tested and in both cases, the wear rate was similar to that obtained at 1 Hz (Saikko, 2017). Pappas et al (1995) ran wear tests at 5 Hz in a hip simulator, but the maximum sliding velocity turned out to be too excessive.

Typical lubricants for testing include bovine serum, deionized water, distilled water and saline. ISO 14242-1 specifies the use of calf serum with 30 g/l protein concentration for hip-joint prostheses, while ISO 14243-1 requires 20 g/l for knee-joint prostheses. However, Scholes & Unsworth (2009) used bovine serum with a 17 g/l protein concentration for wear testing of knee-joint prostheses. Both standards also suggest the use of non-biological lubricants in the initial stages of testing. Based on ISO 14242-1, the loading pattern for wear testing of hip-joint prostheses follows a specific fourth order polynomial equation which produces a double peak between 0 to 62% of the cycle and a constant load of 300 N to the completion of one cycle (Figure 2-15). In addition, the various ranges of motion are specified by sinusoidal equations.

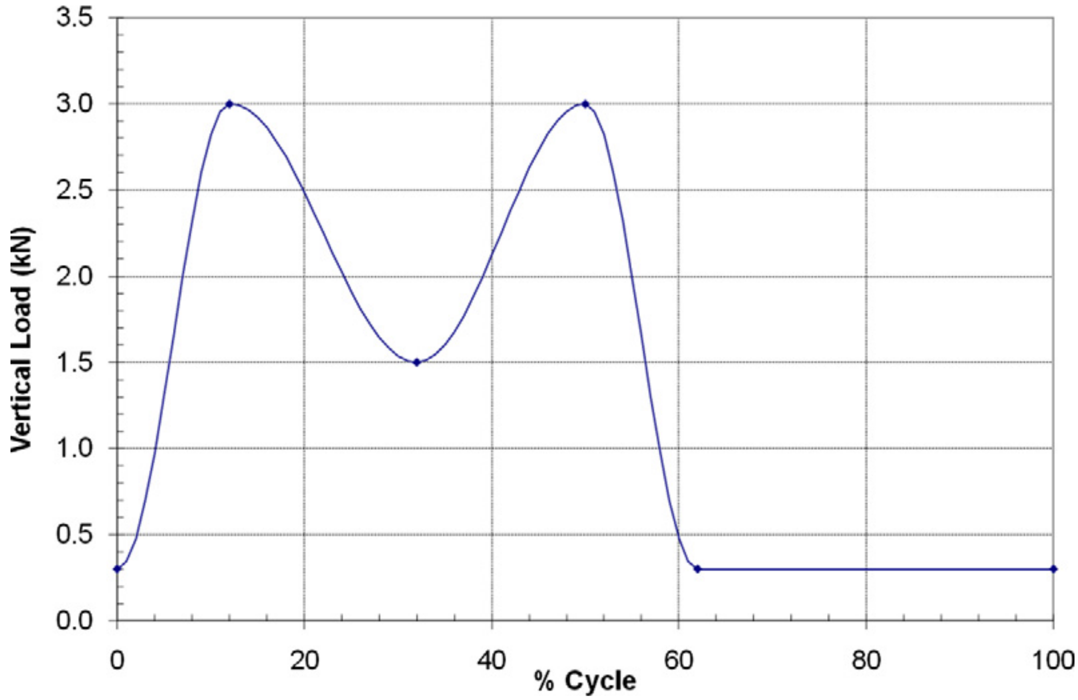

Figure 2-15: Hip joint loading as per ISO 14242-1 (Bandhyopadhya & Bose, 2013)

2.7.3 Subtalar Joint Range of Motion and Loading

Jastifer and Gustafson (2014) compared reports on subtalar joint biomechanics between several researchers. Overall, different methods were used to collect the data, resulting in different values for the ranges of inversion/eversion reported by researchers. In conclusion, the normal range of motion for inversion/eversion was 40 to 60 degrees. It should be noted that the angle of inversion was reported greater than that of eversion.

From a review by Michael et al (2008), researchers developed a numerical model to evaluate the loading at the calcaneus during gait and running. Based on this model, the peak load predicted during gait was 5.4 times body weight while that of running was 4.2 times body weight. Burdett (1982) reported that the ankle joint bears a force of approximately five times body weight during normal gait and a maximum of thirteen times body weight during running, for example. It has been experimentally proven that about 83% of the load from the ankle joint is transferred to the tibiotalar joint. Approximately 77% to 90% of this load is then transferred to the talar dome (Brockett & Chapman, 2016). Therefore, the subtalar joint is subject to the majority of load from the ankle joint.

2.7.4 Wear Measurement

According to ISO 14242-2, either the gravimetric method or the dimensional change method can be used to measure wear. From literature, the more popular method for quantifying wear rate of implants after specified intervals of fatigue testing is the gravimetric method. This method quantifies the rate of wear loss by the difference in mass of the implants. Both the test and control specimens should be soaked for 2 days, cleaned in a very specific manner, dried and weighed. This procedure is done prior to fatigue testing and should be repeated until it exhibits a steady sorption rate. A steady sorption rate is established when the incremental mass change of the specimen is less than 10% of the cumulative mass change. After obtaining a steady sorption rate, the test specimen can then be subject to the specified load and rotary displacement while the control specimen is subject to load only. Although the control specimen is not subject to articulation, it is usually immersed in the same fluid concentration and subject to the same loading as the test specimen. The control specimen is usually test in a separate station. It should be noted that the mass of the control specimen is expected to increase since the implants are manufactured to absorb the water from the test fluid. Since the control specimen is not subject to articulation, it is expected to absorb water easier than an object in motion. The cleaning, drying and weighing procedure is then repeated.

The gravimetric wear of the test specimen is calculated using Equation 2-1.

$$[Eq\ 2-1] \quad W_n = W_{an} + S_n$$

where:

$W_n = net\ mass\ loss\ after\ n\ cycles\ of\ loading$

$W_{an} = average\ uncorrected\ mass\ loss$

$S_n = average\ increase\ in\ mass\ of\ the\ control\ specimen\ over\ the\ same\ period$

Then, the average wear rate, a_G, is calculated using Equation 2-2. This equation employs the least squares linear fit relationship between the net mass loss, W_n and the number of cycles, n.

$$[Eq\ 2-2] \quad W_n = a_G \cdot n + b$$

where:

$W_n = net\ mass\ loss\ after\ n\ cycles\ of\ loading$

$a_G = average\ wear\ rate$

$n = number\ of\ cycles$

$b = constant$

Scholes et al (2008) developed their own procedure for cleaning the samples instead of using the procedure specified in the ISO or ASTM standards. The specific density of the material tested is then used to convert this to a volumetric wear rate.

Studies show that PEEK tends to have a low wear rate than other materials. Wear testing of PEEK on PEEK total cervical disc replacements produced a wear rate of 1.0 ± 0.9 mg/million cycles (Xin et al, 2013). Researchers report wear rates ranging from 2 to 20 $mm^3/10^6$ cycles for knee simulator tests and 10 to 80 $mm^3/10^6$ cycles for total hip replacements (Reinders et al, 2015b). For displacement controlled wear testing of total ankle replacements, the volumetric wear rate obtained was 18.2 ± 1.4 $mm^3/10^6$ cycles. This value was comparable to displacement controlled wear testing of TARs. Bell & Fisher (2007) reported a volumetric wear rate of 10.4 ± 14.7 $mm^3/10^6$ cycles and Affatato et al (2007) reported a volumetric wear rate of 17.1 ± 11.2 $mm^3/10^6$. Therefore, this large variance is typical of wear testing of orthopaedic implants.

2.7.5 Surface Analysis

Surface analysis is necessary to classify the type of wear mechanisms occurring in the implants *in vitro*. Of the studies for wear testing of hip, knee and ankle arthroplasties, researchers typically examine the surfaces of implants before and after wear testing. Surfaces of implants are inspected visually or with devices such as a scanning electron microscope (SEM), atomic force microscope (AFM), profilometer and the optical camera of a coordinate measuring machine (CMM).

2.7.6 Wear Mechanisms

Several types of wear mechanisms have been observed on different joint implants. Kretzer et al (2011) observed burnishing, creep and minimal wear tracks on the surfaces of tibial and fixed bearing inserts of knee prostheses. In another study by Scholes et al (2008), polishing and scuffmarks were seen on the medial tibial components of unicondylar knee implants. Xin et al (2013) reported burnishing and wear tracks on cervical disc implants. After wear testing, Reinders et al (2015a) observed polishing, scratching and adhesive wear on the polyethylene inserts of three-component total ankle replacements. Scholes et al (2007) conducted wear testing of alumina-on-CFR-PEEK hip joints. This study reported pits and wear tracks on the alumina femoral heads and reductions in surface roughness of the acetabular cups.

Chapter 3 Design of Experimental Setup

3.1 Design Requirements

CFR PEEK was selected as the initial material for the subtalar joint implants. The range of motion for inversion/eversion of the subtalar joint is reported as 40 to 60 degrees based on a comparison of studies conducted (Jastifer & Gustafson, 2014). Therefore, the implants will be subject to inversion/eversion of ± 10° at 3 Hz to meet a fraction of the range of motion provided by a fully functional subtalar joint. A relatively small sinusoidal load oscillating between 50–800 N at 6 Hz will be applied to the implants. The maximum load, 800 N, corresponds to the average weight of an adult. This load is much less than the typical reaction force at the ankle joint. However, an injured subtalar joint would be able to support a lesser force than a healthy one. Therefore, the minimum range was chosen for this preliminary study. To simulate physiological conditions, the implants will be submerged in 20 g/l bovine serum diluted with deionized water during wear testing. As such, the subtalar joint simulator should provide a user with the aforementioned requirements for one million cycles of ongoing testing, approximately 4 days.

Readily available in the biomechanics lab is a fatigue-testing machine (Figure 3-1). This machine can apply up to 7500 N of load at a maximum frequency of 100 Hz. The range of displacement of the crosshead is +/-25 mm. In addition, the fatigue testing machine allows a user to program the way load and displacement will be applied during testing and is able of applying several types of waveforms (e.g. half sine, square, and triangle). While this machine can provide the cyclic loading required for this experiment, there is no means of applying rotary displacement to the calcaneus jig.

Adding to this limitation, the load cell is unable to work properly if it is attached to moving objects, it is not water resistant and it was designed with the intention of remaining attached to the bottom platen. To overcome these challenges, the design is modified so that the cyclic load is applied through the talus jig attached to the end of an extension shaft in lieu of the top platen. Consequently, the load cell is also attached to the top platen since the talus jig is not subject to rotation. Having this arrangement in place (Figure 3-1), the amount of space available to attach the mechanism providing rotary displacement and conduct testing are determined.

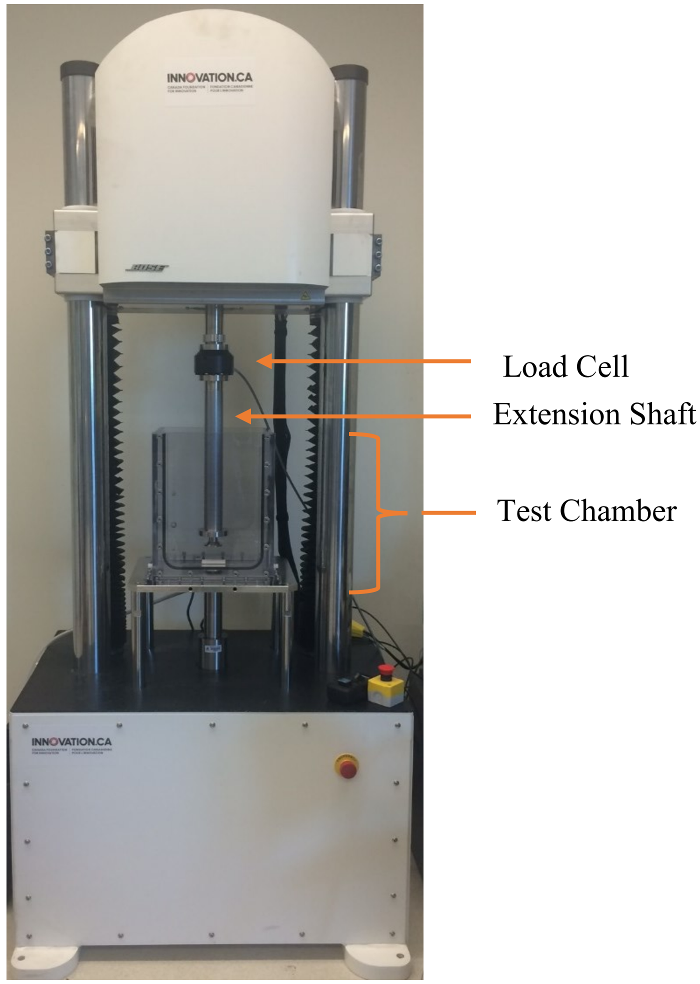

Figure 3-1: Fatigue-testing machine

For safety purposes, the mechanism providing rotary displacement should not extend beyond the emergency stop button of the fatigue-testing machine. Based on the requirements of the experimental design, the design criteria for the rotary actuator were decided as follows:

1. Adjustable angle of rotation
2. Adjustable rotational frequency
3. Easily assembled, disassembled and does not obstruct reach of implants
4. Precise angular rotation and frequency
5. Reasonable life expectancy

Initially, three designs were considered. The first design comprises of springs and bars that would allow rotation and limit the angles of eversion and inversion to the desired value (Figure 3-2). This system would work by finding the exact stiffness of a spring that would allow the talus jig to oscillate within the desired limits of angular displacement. Compressive load would be applied axially through the bars to the rotating talus jig. While this design contains no electrical components, it would be difficult to maintain the accurate angular displacement since the fatigue-testing machine applies load at the crosshead of the machine. Since this mechanism requires springs to operate, it would not have a reasonable life expectancy.

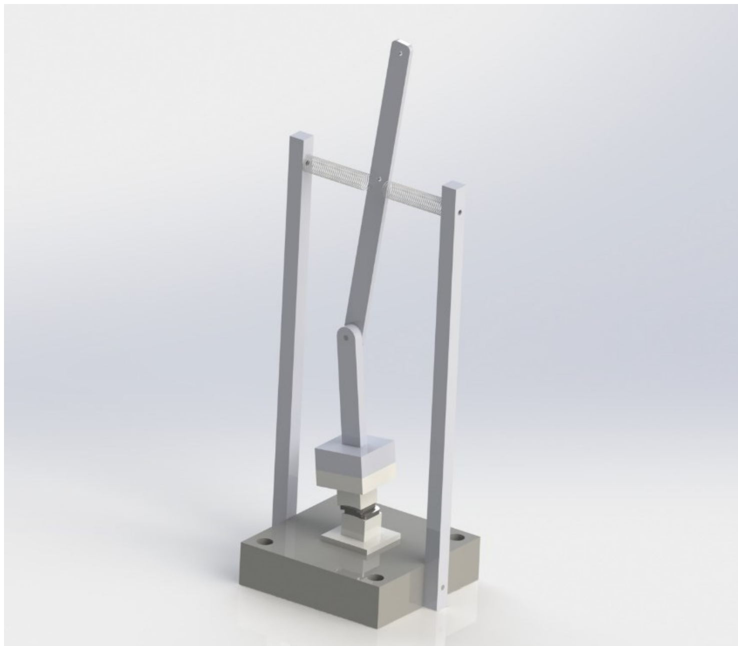

Figure 3-2: Design 1, bars and springs used to apply rotation

The second design consists of a stepped motor, which allows the user to program the specific angle of rotation and speed (Figure 3-3). While this motor provides the most accuracy, it is more expensive than a regular AC motor and requires a speed control and a transformer to operate. The layout of this design is also not ideal since the motor would have to be placed on a platform in front of the machine and get in the way of the user operating it comfortably.

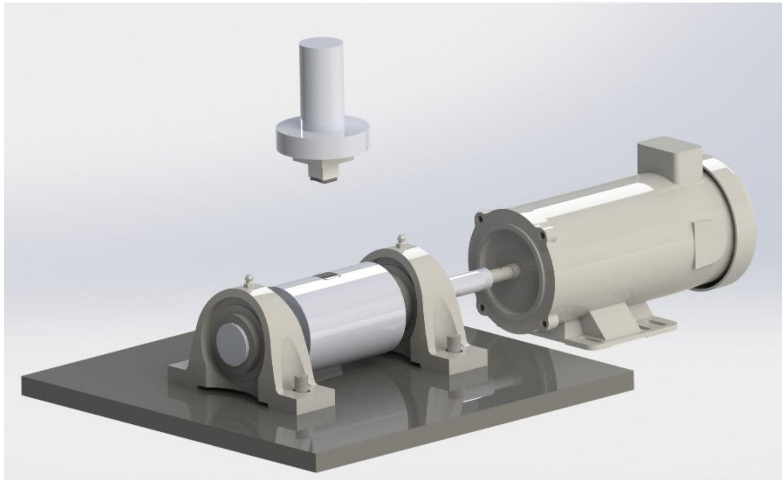

Figure 3-3: Design 2, stepped motor used to apply rotation

The third design utilizes a four-bar mechanism to output a specific angle and path of rotation as designed by the user. This design is simple, flexible and requires relatively inexpensive mechanical and electrical components to operate. A regular AC motor and speed controller can be used to drive the four-bar mechanism. Another benefit is that the moving parts are all within the working space of the machine, making it comfortable for a user to operate the machine safely and make adjustments at any point during testing if necessary.

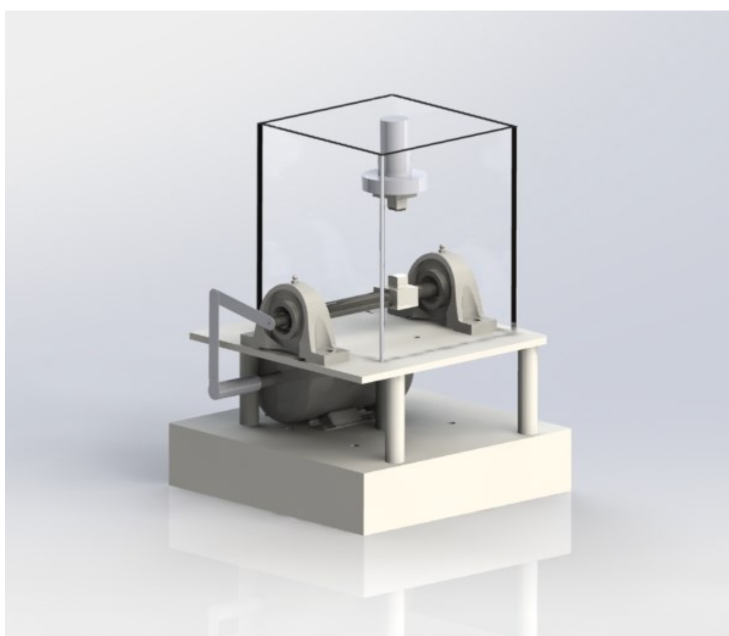

Figure 3-4: Design 3, four-bar mechanism used to apply rotation

Each design was evaluated using the five design criteria. Table 3-1 compares the three proposed mechanisms with the design criteria. Although the second and third designs both satisfied four out of the five design criteria, the ability to adjust the machine without interrupting testing is of more importance for the purpose of these experiments. Therefore, the four-bar mechanism proved to be the best choice (Figure 3-4).

Table 3-1: Comparison of proposed designs with design criteria

Proposed Design	Criteria #1	Criteria #2	Criteria #3	Criteria #4	Criteria #5
1	✓	✗	✓	✗	✗
2	✓	✓	✗	✓	✓
3	✓	✓	✓	✗	✓

3.2 Four-Bar Crank Rocker Mechanism

Of the many options available for attaching a device capable of providing rotary displacement to the fatigue-testing machine, the simplest and most cost-effective method is a four-bar mechanism depicted in Figure 3-5. A four-bar mechanism is one of the simplest means of controlling single degree of freedom (DOF) motion (Norton, 2008). For this particular configuration in Figure 3-5, the shortest linkage (s) represents the crank. This is the linkage responsible for driving the system. The linkage oscillating between two positions (p) is called the rocker, and the linkage connecting the crank to the rocker (q) is called the coupler. The ground length (l) is the distance between the two pinned ends and is not part of the physical linkages required for a four-bar mechanism. This mechanism is ideal for this experiment since rotation of the calcaneus jig is the only required DOF. For a four-bar mechanism to function, the Grashof condition denoted by Equation 3-1 should be satisfied.

$$[Eq\ 3-1] \qquad s + l \leq p + q$$

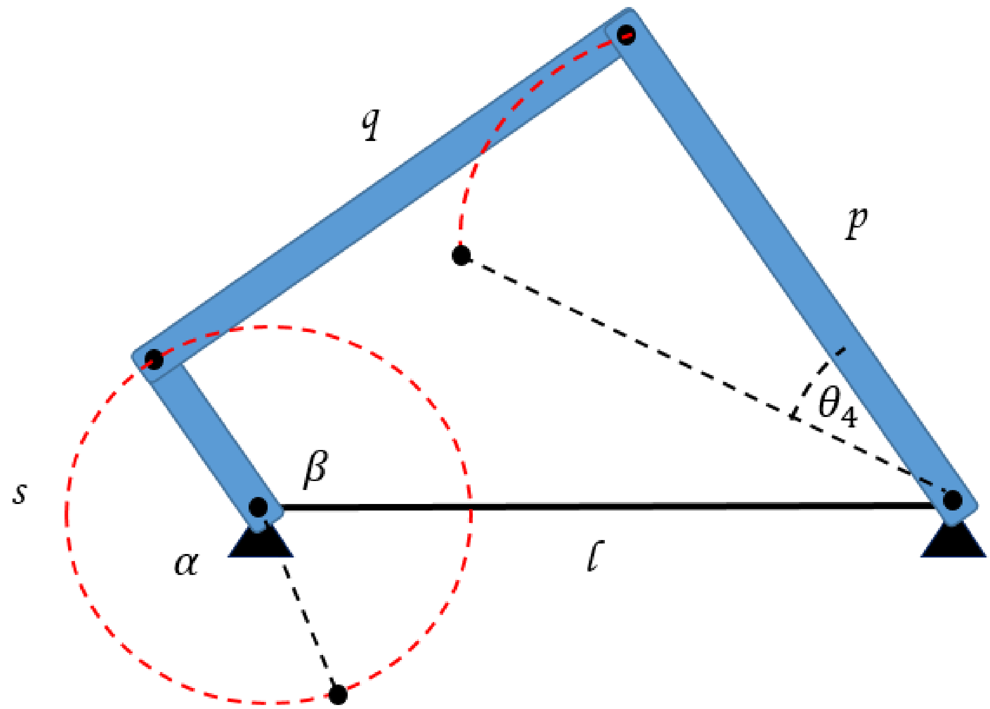

Figure 3-5: Typical four-bar crank rocker mechanism

where:

s = length of shortest linkage (mm)

l = length of longest linkage (mm)

p,q = length of other linkages (mm)

θ_4 = output angle (°)

α = angular displacement of crank to complete forward motion (°)

β = angular displacement of crank to complete return motion (°)

Based on the magnitude of the left-hand side of the inequality with respect to that of the right-hand side, various patterns of motion are exhibited by a four-bar mechanism.

In keeping with the goal of a simple, cost-effective design to provide rotary displacement, Class I crank rocker (GCRR) motion is selected. As the crank rotates 360° counterclockwise or counterclockwise, the rocker moves from its maximum to minimum toggle positions during its forward motion phase and back to its maximum toggle position during its return motion phase. A simple AC motor can maintain rotation in either direction at a constant velocity. In addition, the oscillation of the rocker translates to the calcaneus jig. This is done by attaching the calcaneus jig to the pinned end of the rocker via a shaft. To obtain this motion pattern, the sum of the lengths of the shortest and longest linkages should be less than that of the remaining linkages.

3.2.1 Construction of a four-bar crank rocker mechanism

Several factors are considered before constructing possible orientations for the four-bar mechanism used in this experimental setup. First, the locations of the shaft supporting the calcaneus jig and the motor shaft are identified. This limits the possible orientations that can be used for the mechanism. In addition, the AC motor used provides constant velocity to the system. Therefore, an even return four-bar crank rocker mechanism is designed rather than a quick return four-bar mechanism. As the name implies, an even return four-bar crank rocker mechanism takes the same amount of time to complete both forward and return motions. The transmission ratio, T_r, is defined as the time taken for the crank to complete forward motion divided by the time taken to return to its original position and is described by Equation 3-2. This is necessary for a more even distribution of the load on the mating surfaces of the talus and calcaneus jigs.

$$[Eq\ 3-2] \qquad T_r = \frac{\alpha}{\beta}$$

From Figure 3-6, the location of the motor shaft is denoted as O_2 while that of the shaft supporting the calcaneus jig as O_4. A horizontal line is drawn from O_4 in the direction of O_2 and a vertical line is drawn from O_2 beyond O_4. The point of intersection is labelled B. Considering the angles of eversion and inversion, ±10° lines are drawn from point O_4 to the vertical line originating from O_2. The points of intersection of these angular lines with the vertical line are labelled B_1 and B_2 respectively. Thus, the output angle (20°) is the sum of the absolute value of the angles of eversion and inversion |10° + -10°|. From geometry, B_2B is equal to BB_1 and O_4B_1 is equal to O_4B_2. A circle of radius BB_1 is drawn at O_2 and represents the path of the crank under rotation. Then, the vertical line from O_2 is extended to the circumference of the circle. The two intersecting points labelled A_1 and A_2 represent the positions of the crank when the rocker is at points B_1 and B_2 respectively

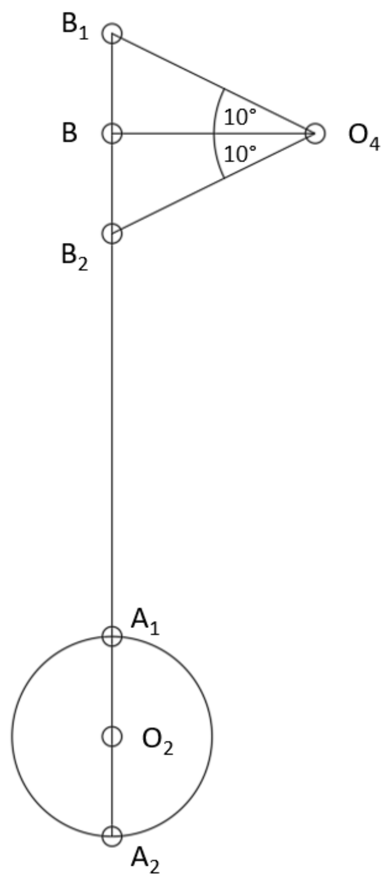

Figure 3-6: Construction of an even return four-bar crank rocker mechanism

Figure 3-7 depicts the geometrical properties of the four-bar mechanism used in this experiment. Based on the lengths of each linkage, the Grashof condition is tested for the experimental setup and is satisfied. In this configuration, equal angles are covered between the stationary points of the rocker and unit time ratio is achieved. The next step is to size the cross section of each linkage, which is covered in Chapter 4.

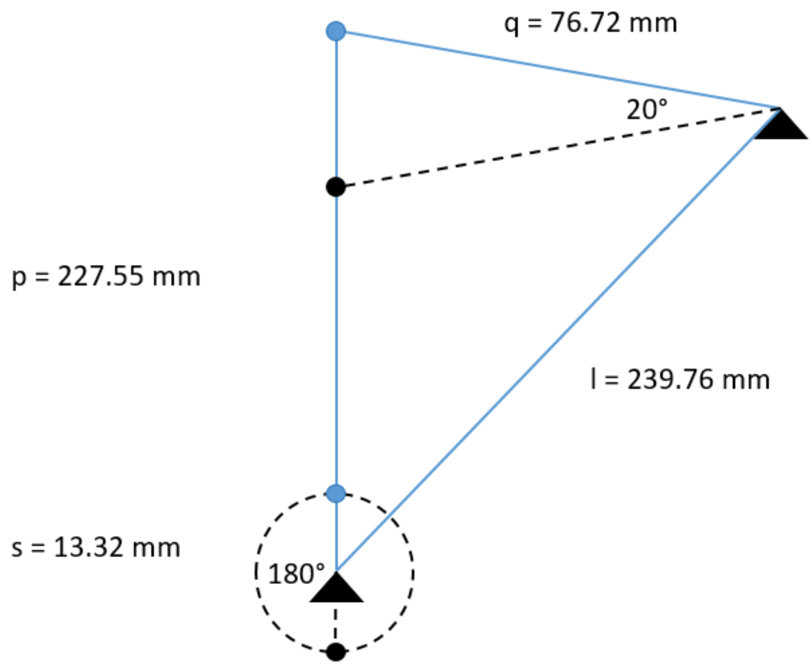

Figure 3-7: Geometrical configuration of four-bar mechanism used in experiment

$$T_r = \frac{\alpha}{\beta} = \frac{180}{180} = 1$$

$$s + l \leq p + q$$
$$13.32 + 239.76 \ \leq 76.72 + 227.55$$
$$253.08\ mm < 304.27\ mm$$

3.3 Mechanical Components

After finalizing the design of the four-bar mechanism, the other mechanical components needed to complete the experimental setup are designed. Pre-existing talus and calcaneus jigs are provided (Figure 3-8). These jigs are later modified to be attached to the experimental setup.

Figure 3-8: Original talus and calcaneus jigs

The existing fatigue-testing machine, four-bar mechanism, calcaneus jig, talus jig and other parts needed to mount are modelled and assembled using Autodesk Inventor Professional. This is necessary to minimize error post purchasing and manufacturing. Factors taken into consideration include the space available for persons to mount the parts and common practices. Figure 3-9 depicts the 3D model of the proposed experimental setup generated from Inventor. Refer to Table 3-2 for the corresponding parts list.

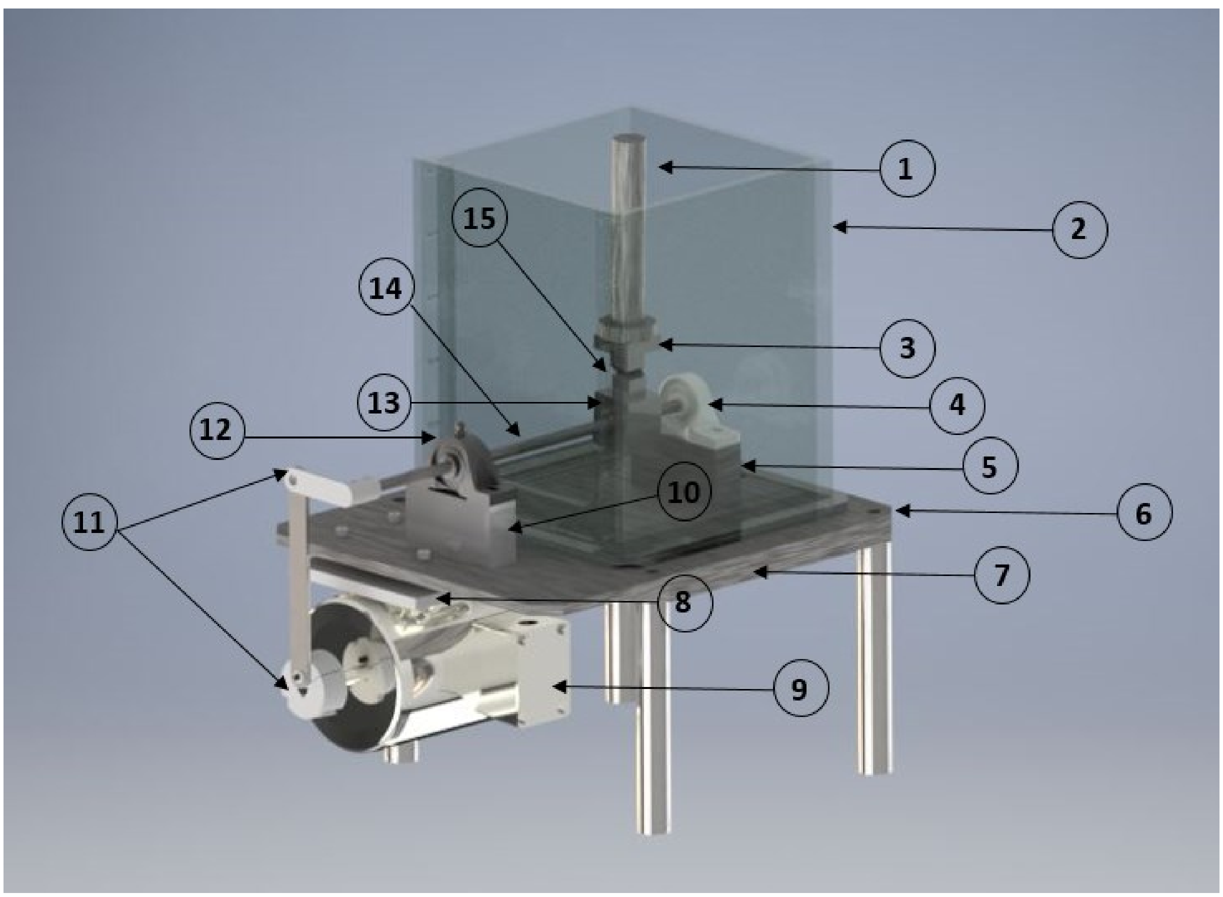

Figure 3-9: Isometric view of the experimental setup

Table 3-2: Parts list

Number	Part Name
1	Extension Shaft
2	Water Bath
3	Talus Jig
4	Corrosive Ball Bearing
5	Spacer
6	Modified Plate
7	Original Steel Plate
8	Motor Mounting Plate
9	Motor
10	Spacer
11	Four-Bar Mechanism
12	Ball Bearing
13	Calcaneus Jig
14	Shaft
15	Implants

Two additional steel plates are placed above and below the original plate installed with the fatigue-testing machine (Figure 3-10). Both plates are necessary to support the motor since it is mounted at its base. The upper plate also supports the external bearing block and expands the testing area for future attachments.

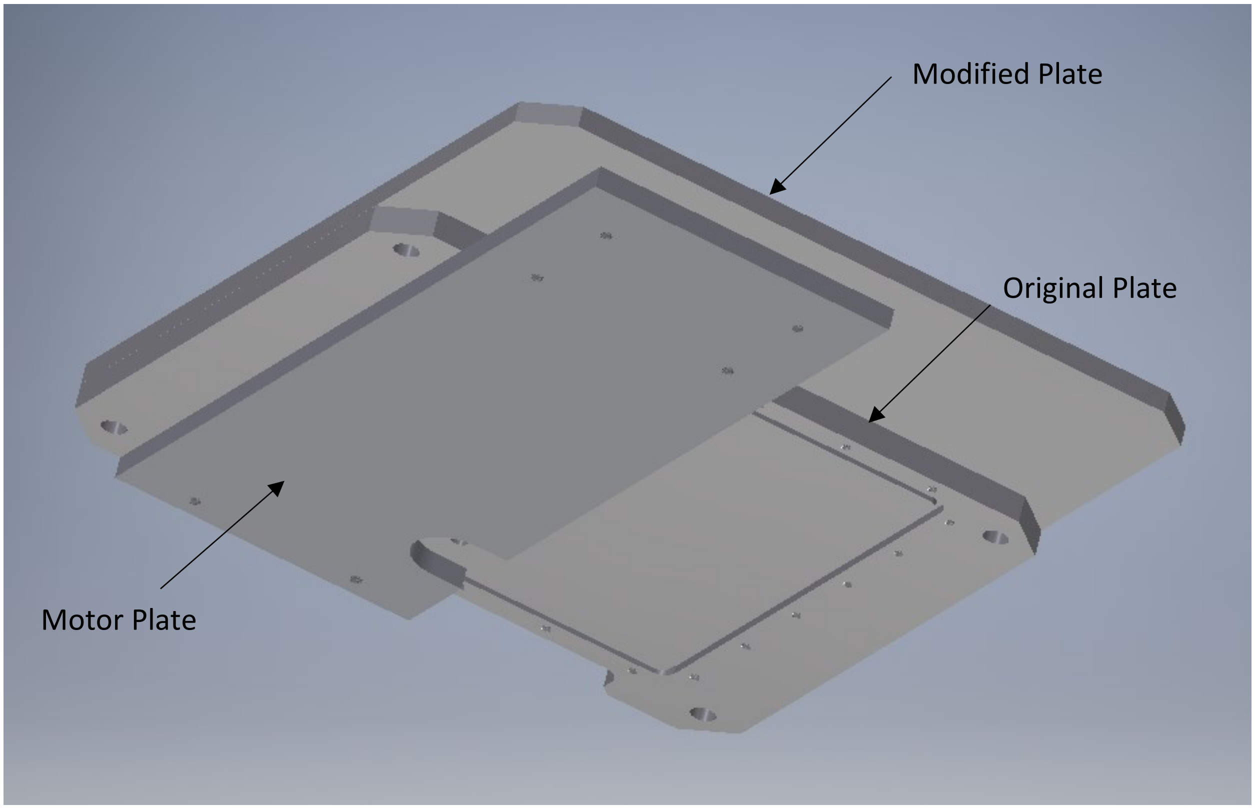

Figure 3-10: Original steel plate sandwiched between modified plate and motor plate

Since the manufacturers did not provide details of the existing plate, manual measurements using the metric scale are taken with a measuring tape, Vernier calipers and a ruler. It was not until after the plates were manufactured that the researcher realized that the manufacturer used imperial units. In addition to parallax errors, this introduced errors during assembly of the manufactured parts as the holes connecting the water bath to the plates were misaligned by 1/16" along one edge. This issue is remediated using smaller bolts and clamps.

A motor drives the four-bar mechanism while the implants are immersed in fluid and subject to compressive load. For this reason, the four-bar mechanism is placed outside the water bath and connected to the calcaneus and talus jigs within the test chamber. A shaft connects the calcaneus jig to the rocker via two shaft couplings. A shaft coupling consists of a shaft, keyway and hub. This mechanism connects the rocker and the calcaneus jig to the shaft. Since the shaft is inserted into the calcaneus jig, it acts as the hub and has a keyway cut through it (Figure 3-11). A coupling translates the motion of the rocker to the calcaneus jig. The keyway connecting the calcaneus jig to the shaft coupling is positioned so that the calcaneus jig is directly aligned with the talus jig above it. Details for the design of the hub and keyway are found in the Section 3.5.2.

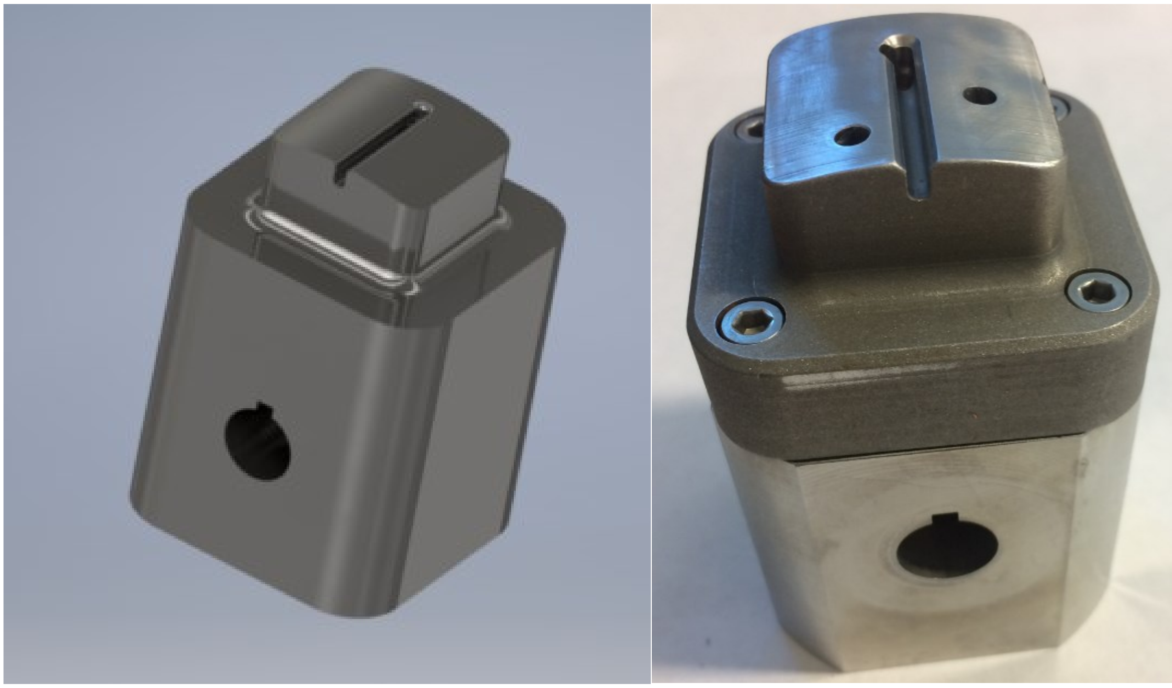

Figure 3-11: Modified calcaneus jig

A means of preventing the calcaneus jig from moving along the shaft was not considered during its design. To address this issue, a shaft collar (Figure 3-12) is placed in front and behind the calcaneus jig on the shaft. Placing the shaft collar and calcaneus jig in direct contact with each other causes additional friction forces on the system. Therefore, strips of Velcro were placed between the two to absorb the shock from the friction forces generated.

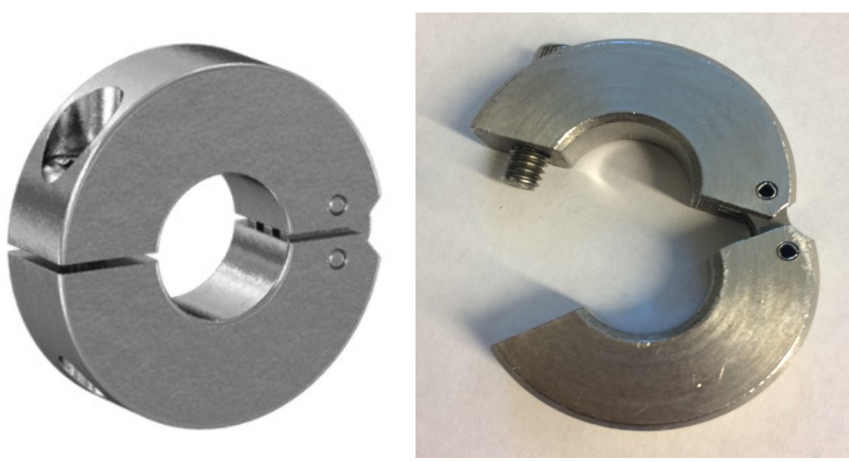

Figure 3-12: Hinged shaft collar. Retrieved from Mcmaster.com

Since the talus jig remains stationary while connected to an extension shaft on the crosshead of the fatigue-testing machine, a threaded blind hole is borne through the top of it (Figure 3-13).

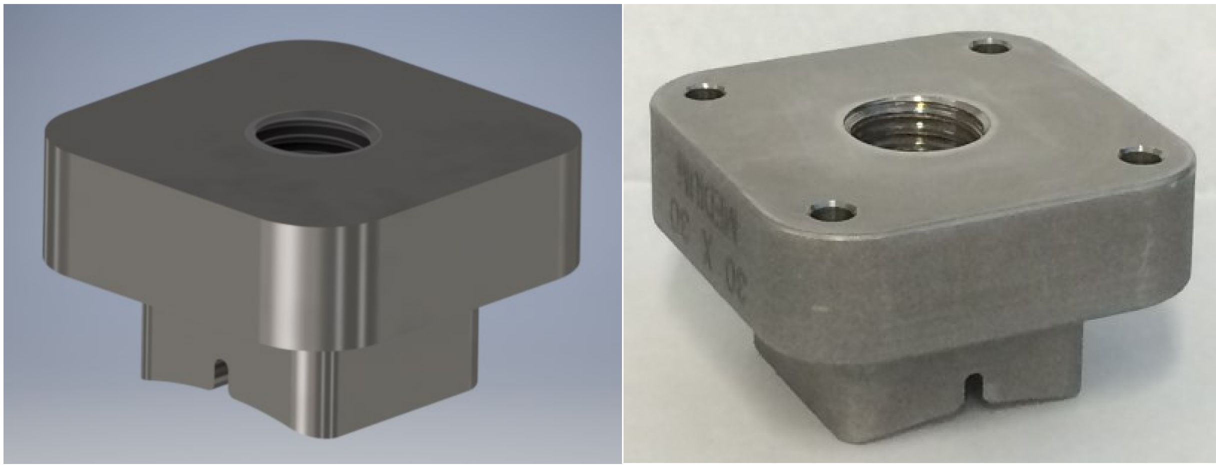

Figure 3-13: Modified talus jig

Fabrication of a 13.32 mm long steel bar to function as a crank is impractical. Therefore, a taper lock bushing will be attached to the shaft of the motor in lieu of a miniature steel bar. Since the bushing is manufactured as a hub for a keyed shaft, an additional hole 13.32 mm away from the centre of the bushing is drilled on its surface. In case a different output angle is required, a user may drill additional holes at the necessary distance away from the centre of the bushing (Figure 3-14). Using a taper lock bushing enables flexibility of the experimental setup.

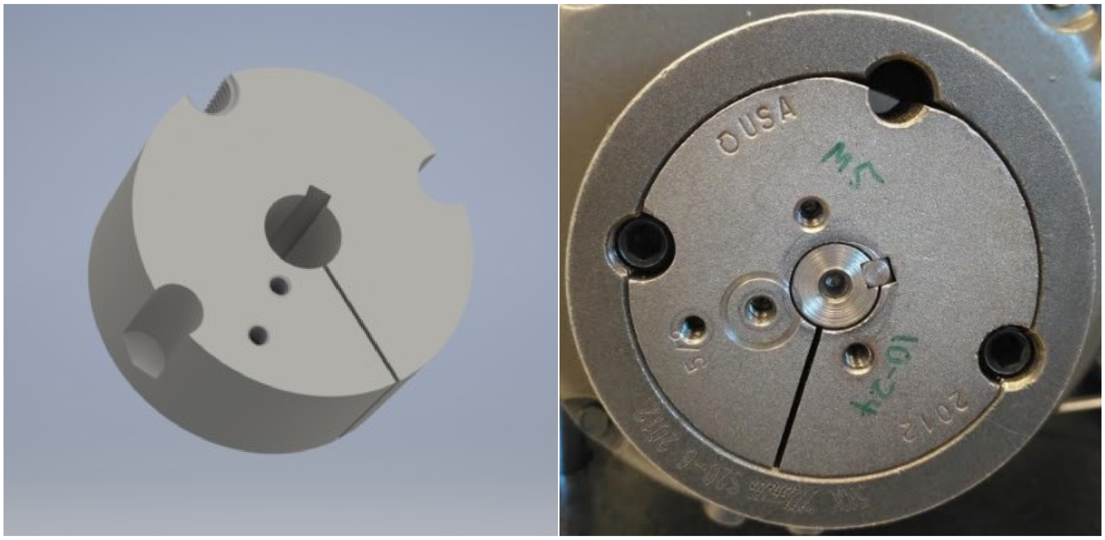

Figure 3-14: Modified taper lock bushing

The coupler (Figure 3-15) and rocker (Figure 3-16) are similar to the schematic shown in Figure 3-2. Since the rocker is used to translate its oscillation to the calcaneus jig via a shaft, a rigid shaft coupling is welded to it.

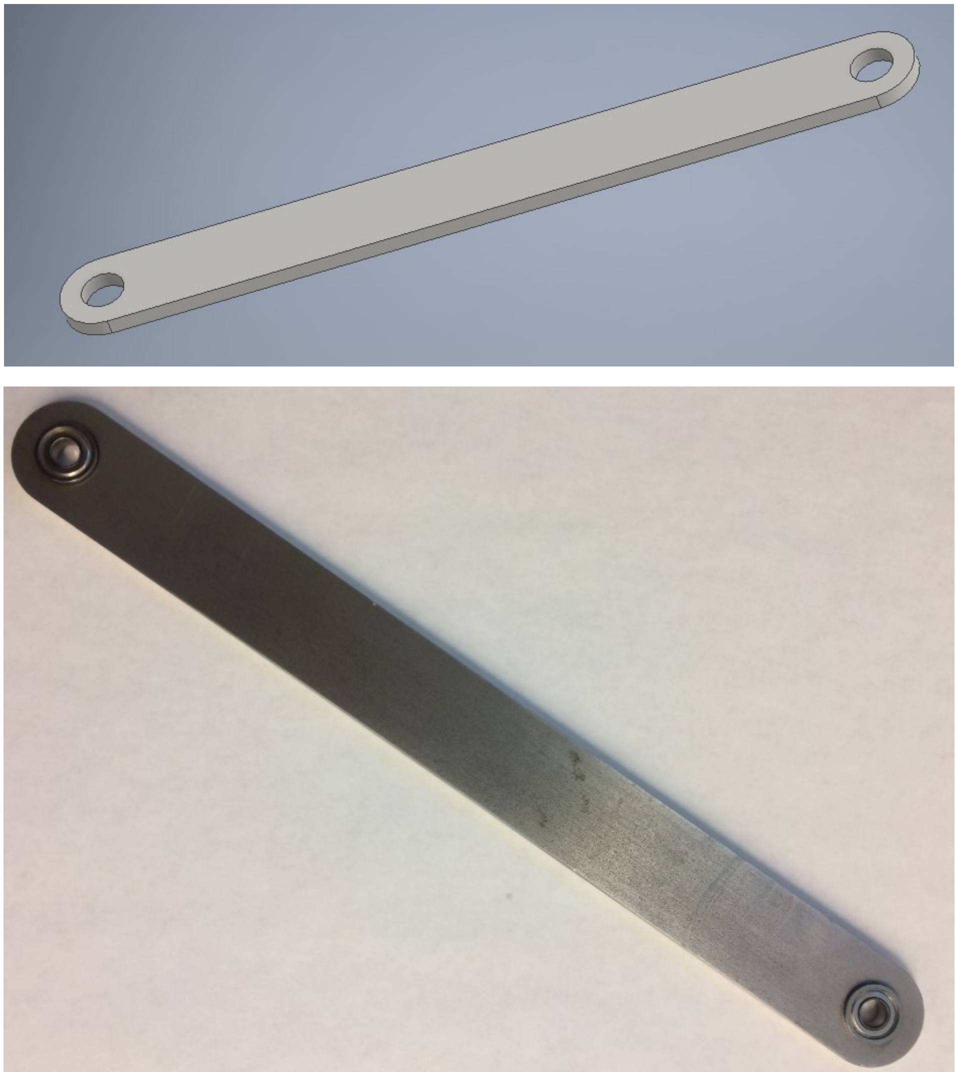

Figure 3-15: Coupler

Figure 3-16: Rocker welded to rigid shaft coupling

A smaller test chamber was designed to significantly reduce the amount of bovine serum required to fully submerge the implants during wear testing (Figure 3-17). With this chamber, 1 L of the immersion fluid will be sufficient to conduct testing. This should be changed at least every 500,000 cycles according to ISO 14242-2.

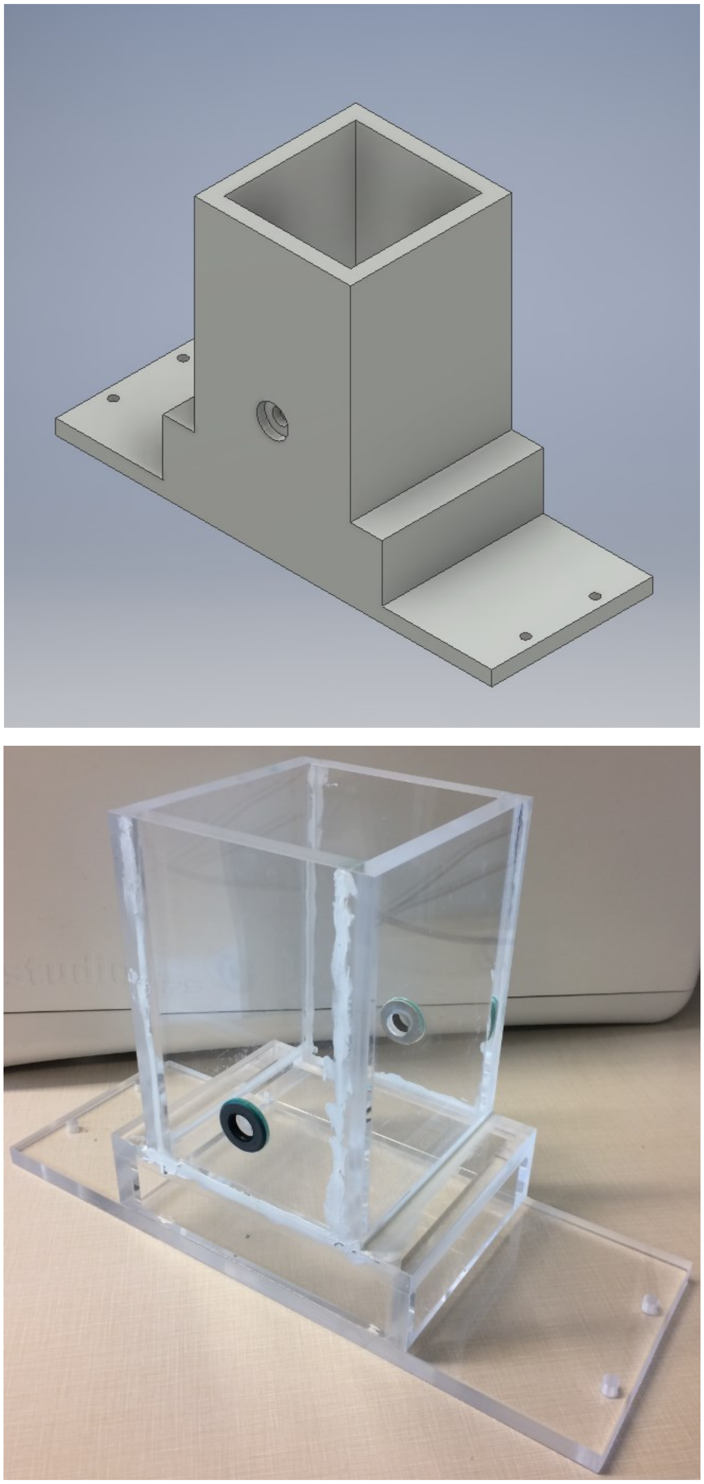

Figure 3-17: Smaller test chamber

3.4 Waterproofing

3.4.1 O-ring Seals

Replicating the original steel plate means that an identical groove and O-ring is necessary for the new plate. Unfortunately, the manufacturer of the fatigue-testing machine did not provide detailed drawings of the steel plate. Therefore, the researcher presents a brief discussion on the design of O-ring seals. An O-ring seal (Figure 3-18) is an alternative to a flat gasket, and prevents the leakage of gases or fluids from a chamber. It consists of a gland and an O-ring, which is made of PTFE, elastomers, thermoplastic materials or metals and can have either a solid or hollow cross section. The gland houses and supports the O-ring. Usually, it is cut into a more rigid material such as metal. Several benefits of using an O-ring include:

1. Its ability to withstand a vast range of temperature, pressure and tolerance
2. Its life span is equivalent to that of the material it is made of
3. It can be easily replaced when damaged
4. It is relatively inexpensive
5. It is not affected by compression or torque from tightening
6. It has a gradual failure pattern rather than sudden destruction

Figure 3-18: O-ring seal

An O-ring seal works by eliminating the clearance that the liquid or gas that it is sealing off tends to flow through. Figure 3-19(a) shows the cross section of an O-ring, the softer material, restrained by a rigid gland and plate. At this point, there is no application of pressure to the O-ring seal. However, its original circular cross section is “mechanically squeezed out of round” between the top plate and the gland so that the flow of fluids or gases from either side is prevented. Applying mechanical pressure to the system causes the seal to protrude the micro fine grooves of the gland and move up to the gap between the surfaces of the harder materials as shown in Figure 3-19(b). As a result, the sealing ability of the O-ring heightens during this phase. Every material has specific properties with limits. At its pressure limit, the O-ring slowly begins to extrude into the narrow gap between the gland and the top plate (Figure 3-19(c)). Increasing pressure results in more of the O-ring extruding further into the narrow gap until failure (Figure 3-19(d)).

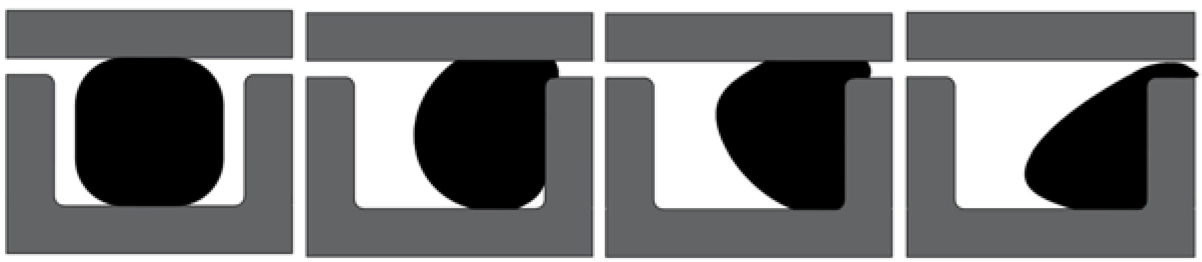

Figure 3-19: Life cycle of an O-ring seal

3.4.1.1 Static Seals

Since the water bath used in the experimental setup is attached to the steel plate with bolts, this type of O-ring seal is classified as a static face seal (Figure 3-20). As the name implies, the mating gland and top plate are stationary. Design Chart 4-3 of the Parker O-Ring Handbook is used to size the groove cut into the new plate (Seals, 1992). Based on this chart, the optimal design width of the groove depends on whether the fluid being sealed off is a liquid or a gas.

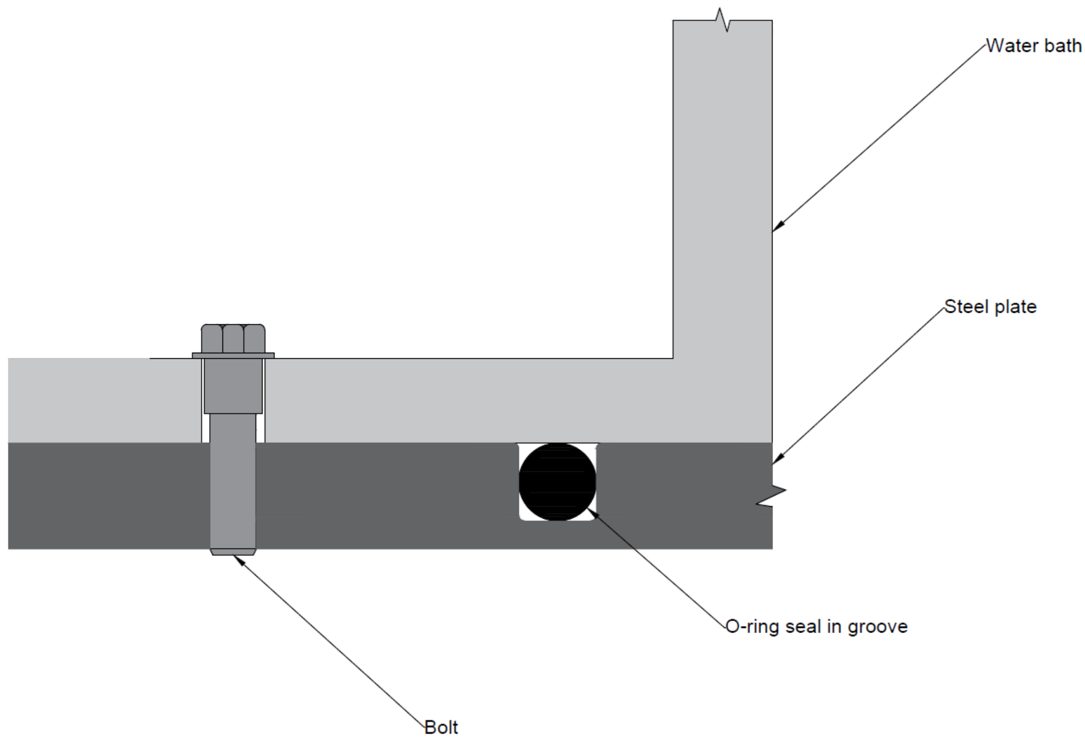

Figure 3-20: Cross section of static face seal

The idea is to replicate the O-ring groove and bolt holes on the original steel plate. Therefore, the average value of several measurements of the existing O-ring determine its cross section, inner diameter (ID) and outer diameter (OD). These values and Design Chart 4-3 help to determine the groove details. Based on the measurements taken, the cross-section width of the O-ring is 0.139 ± 0.004 in. Since the existing O-ring used too stretched out to accurately measure its inner and outer diameters, the inner and outer perimeters of the groove on the original plate can estimate these values. The groove width on the original plate is also measured using Vernier calipers and averaged to be at most 4.8 mm (0.189 in). Based on Design Chart 4-3, the measured values and the design conditions, the following parameters are selected:

1. O-Ring Size = 201 through 284
2. Gland Depth (L) = 0.107 in
3. Groove Width (G) = 0.187 in
4. Groove Radius (R) = 0.025 in
5. Surface Finish X = 32
6. Squeeze = 30 %

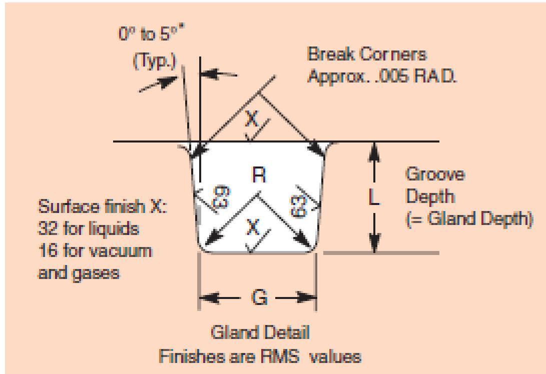

Figure 3-21: Gland details (Seals, 1992)

3.4.1.2 Rotary Seals

From the 3D model of the experimental setup, the shaft supporting the calcaneus jig passes through the cover of the test chamber. Therefore, leakage and cracking can occur from the constant rotation of the shaft and the contact with the cover of the water bath. It is necessary to select and install a suitable shaft seal that accommodates rotary displacement at the specified speed of inversion/eversion. Prior to selecting a seal, one should consider that this shaft is subject to deflection from the applied load and rotation from the four-bar mechanism. In addition, the door of the test chamber is made of plexiglass, which is brittle, by nature.

Considering the conditions that the shaft is subject to, a double lip seal is selected to prevent fluid leakage at the shaft opening on the cover of the test chamber (Figure 3-22). A double lip seal is categorized as a rotary or mechanical seal and is purchased based on the available standard sizes of shaft diameters. Therefore, it is not necessary to design this seal.

Figure 3-22: Mechanical lip seal. Retrieved from Mcmaster.com

After selecting the lip seal, the door of the test chamber is modified to accommodate it (Figure 3-23). Based on the thickness of the seal, it sits about halfway through the thickness of the plexiglass door. The counterbore to accommodate the outer diameter of the lip seal and the shaft is assigned a press fit tolerance so that it can easily be replaced when necessary.

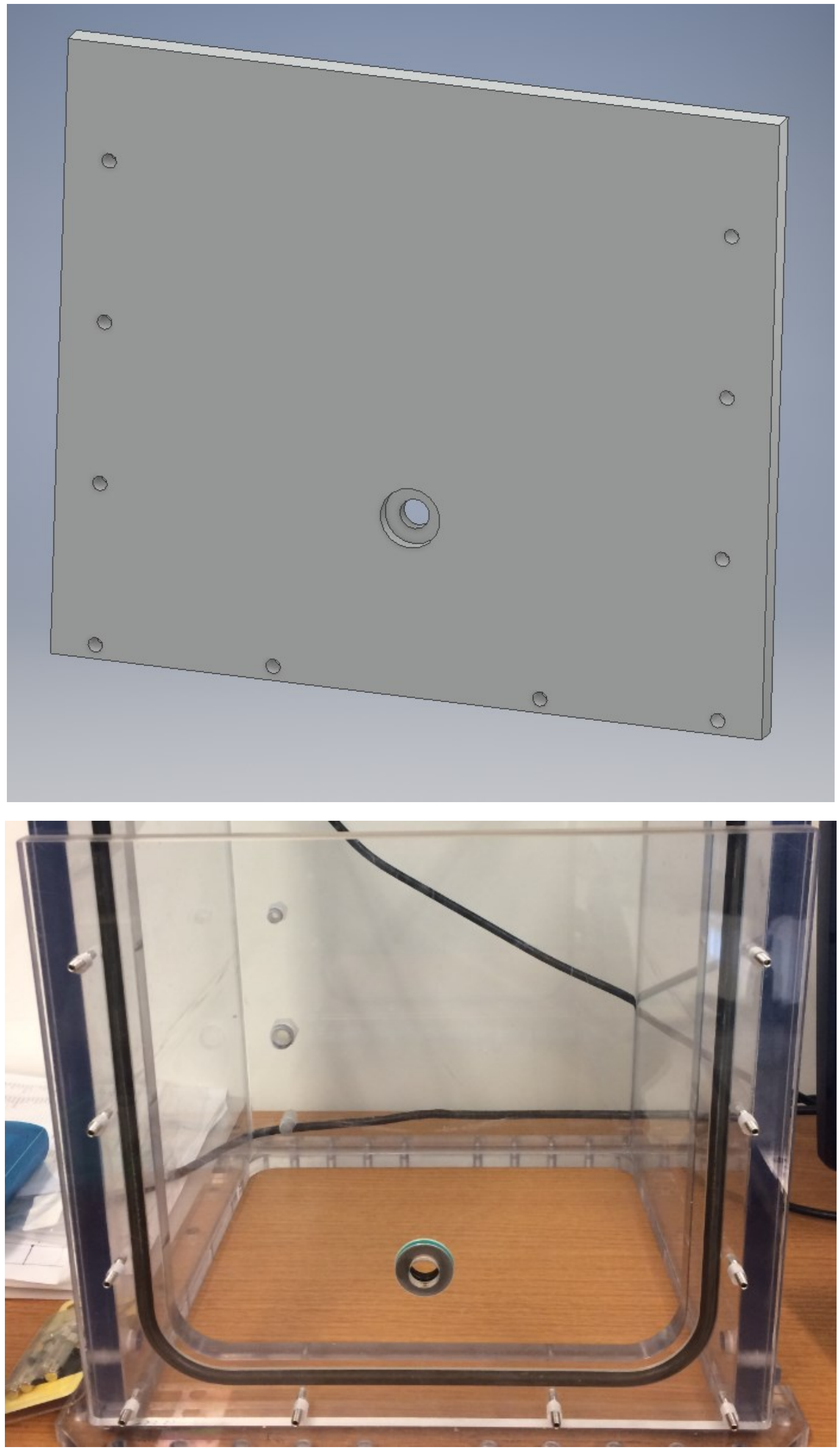

Figure 3-23: Modified test chamber cover

3.4.2 Drainage

To facilitate the collection of the immersion fluid at the end of testing, the new steel plate placed on top of the existing one had a drainage hole with the same diameter as that of the existing plate drilled through it. This is done so that the aligned holes will allow uninterrupted fluid to flow through the drain. However, fluid leaked out from a gap between the two stacked plates and through the bolt holes connecting the water bath to the plate. After several attempts to remediate this issue, a layer of silicon coating the gap between the drainage holes of the two upper plates proved effective.

A self-priming siphon pump (Figure 3-24) is used to drain immersion fluid from the smaller test chamber since it does not extend to the location of the drain. To avoid disassembly of the entire setup, soapy water is used to flush the bath and clean the siphon pump simultaneously.

Figure 3-24: Self priming siphon pump. Retrieved from Canadiantire.ca

3.5 Design of Shaft and Shaft Couplings

Shaft design requires the consideration of several factors and should be done in the following steps:

1. Define the shaft topology
2. Specify the driving elements such as gears, pulleys, sprockets, etc.
3. Free body diagram
4. Select bearings and position
5. Consider shaft deflection and stress

6. Check for critical speed
7. Specify connections and dimensions

3.5.1 Shaft Deflection

The shaft shown in Figure 3-25 is connected to quite a few of the mechanical components in the test setup. Its diameter determines myriad of things including the size of the keyway and shaft holes of the rocker and calcaneus jigs, the diameter of the hole drilled into the water bath cover, the inner diameter of the mechanical seal discussed previously, and the diameter of the mounted ball bearings used to support the shaft. As the calcaneus jig and the shaft used to apply cyclic load are considerably heavy stainless steel objects, it is necessary to determine if this added weight will cause deflection in this shaft.

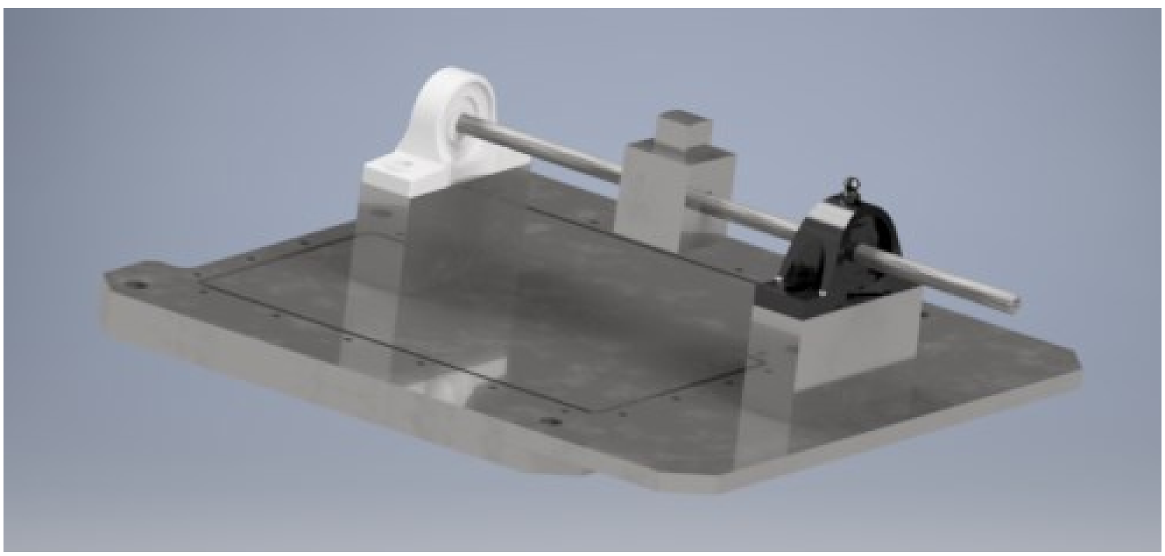

Figure 3-25: Shaft loads and boundary conditions

After obtaining the optimal diameter, the details of the shaft couplings are determined. Equation 3-3 is the general means of determining the minimum diameter of the shaft (Norton, 2014).

$$[Eq\ 3-3] \qquad d = \left\{ \frac{32N_f}{\pi} \left[\frac{\sqrt{\left(k_f M_a\right)^2 + \frac{3}{4}\left(k_{fs} T_a\right)^2}}{S_f} + \frac{\sqrt{\left(k_f M_m\right)^2 + \frac{3}{4}\left(k_{fs} T_m\right)^2}}{S_{ut}} \right] \right\}^{1/3}$$

where:

N_f = Safety factor

$M_{a/m}$ = Alternate and mean moment (N-mm)

$T_{a/m}$ = Alternate and mean torque (N-mm)

S_f = Stress endurance limit (MPa)

S_{ut} = Ultimate tensile strength (MPa)

K_f = Fatigue stress-concentration factor for bending

K_{fs} = Fatigue stress-concentration factor for torsion

Since a dynamic load is applied to this shaft, we will only consider the maximum load, 800 N, in this calculation. Assume that the mounted bearings and water bath cover are pinned and roller connections. Tightening the set screws on the ball bearings restricts axial movement of the shaft. Therefore, the ball bearings can either be modelled as a pin or roller connection if the set screws on them are tightened or not. Next, the calcaneus jig is modelled as a concentrated load at the centre of its location on the shaft. This is done by retrieving its volume from Autodesk Inventor and multiplying it by the density of stainless steel and gravity. The equivalent force from the calcaneus jig is approximately 11 N. Using the double integration method, the deflection along the shaft was then investigated (Figure 3-23). Three cases were considered:

1. Not considering the interaction of the shaft with the water bath cover as a reaction force.
2. Considering the reaction force of the water bath cover on the shaft
3. Considering the interaction of the shaft with the smaller test chamber

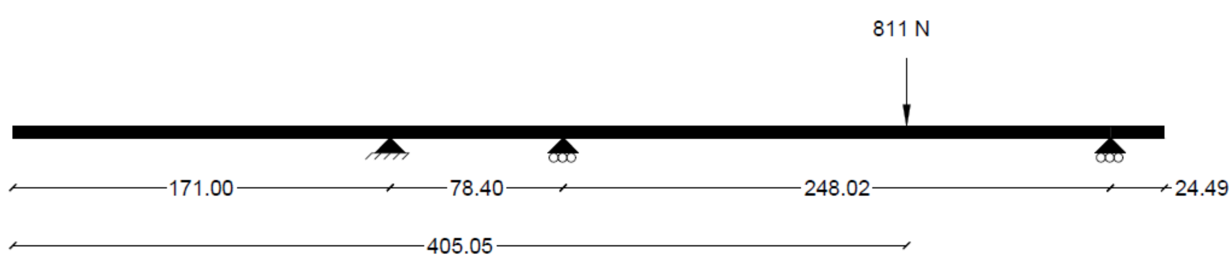

Figure 3-26: 2D model of shaft with all boundary conditions and loads

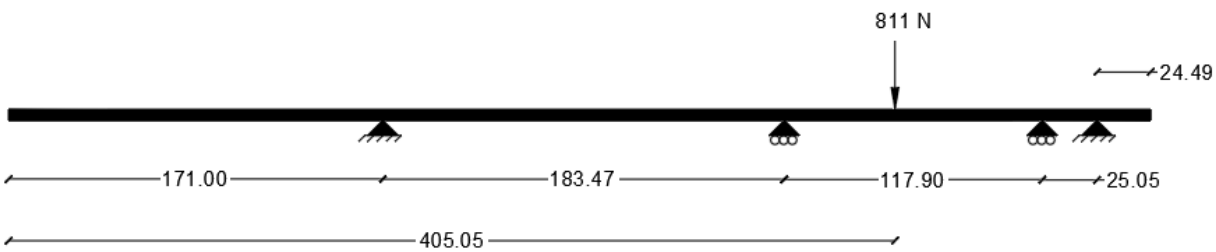

Figure 3-27: 2D model of shaft with boundary conditions from smaller test chamber and loads

The deflected shape of the shaft can first be estimated using the stiffness method in MATLAB. The shaft is split into five elements with six nodes so that the load and constraints can be applied. Material properties of the shaft, such as the area moment of inertia and Young's modulus, are calculated. Magnification factors of 5 and 20 are used for Case 1 and Case 2 respectively so that the plots of the deflected shape are more visible. Figures 3-24 and 3-25 show the deflected shapes of the shaft in both cases. To obtain the actual maximum deflection, divide the figure from the plot by the respective magnification. The maximum deflection is 2.51 mm and -0.57 mm for Case 1 and Case 2 respectively.

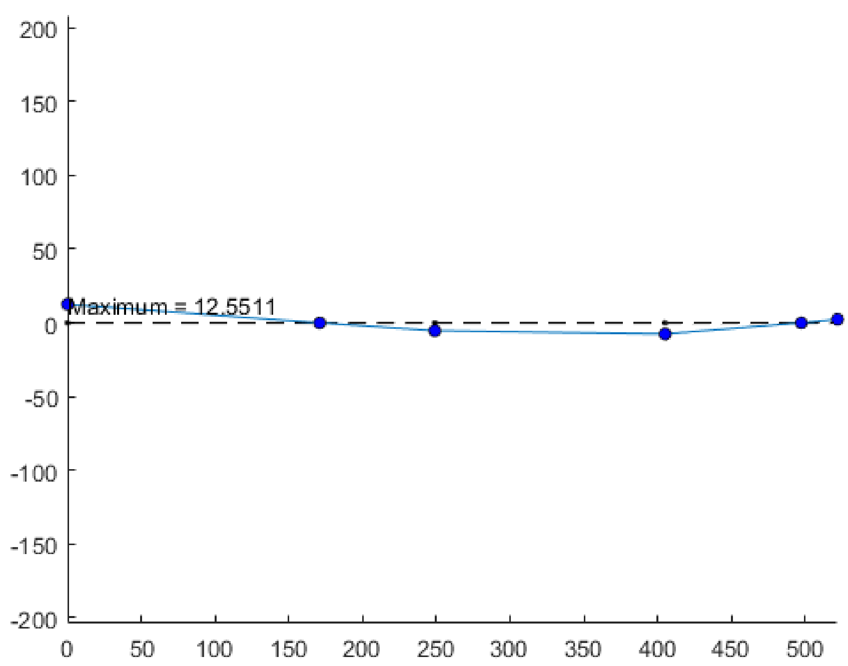

Figure 3-28: Deflected shape of Case 1 shaft using MATLAB

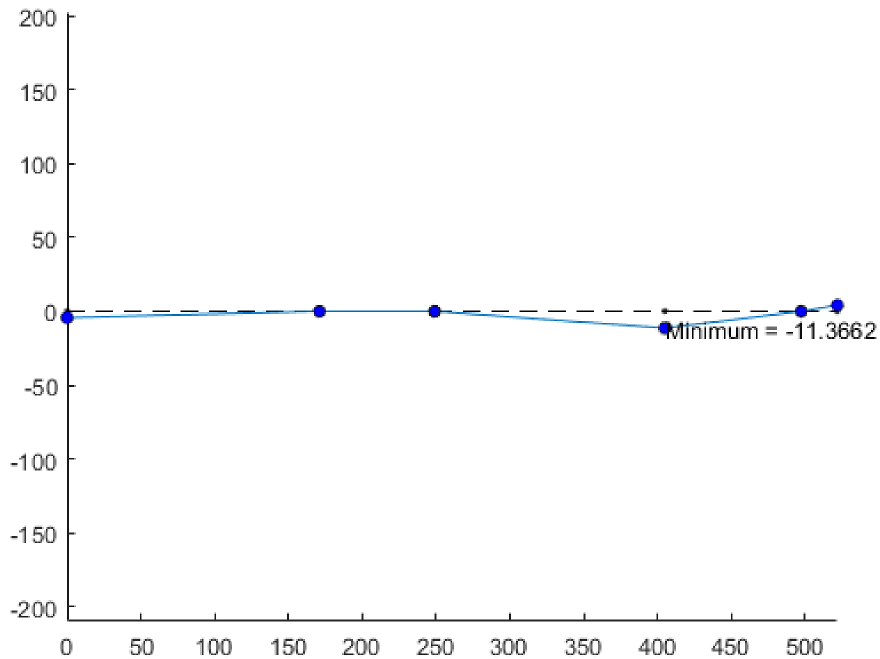

Figure 3-29: Deflected shape of Case 2 shaft using MATLAB

Abaqus is used to verify the deflected shape of the shaft obtained by hand calculation in Case 1 and Case 2. A static general analysis is used for this analysis. The shaft is modelled as a 2D deformable wire with solid, circular cross section that is 12.7 mm (1/2 in) in diameter. To apply the load and boundary conditions at nodes, the beam is modelled using a line with continuous points. The nodes are taken as the x-y coordinates of each constraint, the load and the beginning and end of the beam. In case 1, the maximum deflection, 2.51 mm, is at the left cantilevered end of the beam (Figure 3-30). In case 2, the maximum deflection, 0.58 mm, is also at the point of application of the load (Figure 3-31). This confirms that considering the restraint provided by the water bath cover significantly reduces the overall deflection of the shaft.

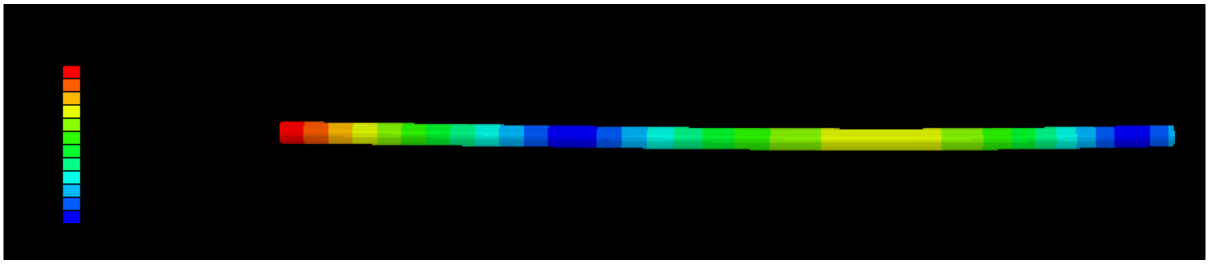

Figure 3-30: Case 1 deflection of ½-inch shaft

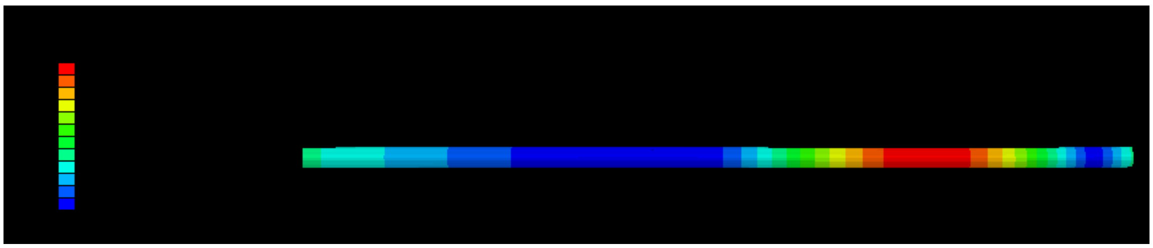

Figure 3-31: Case 2 deflection of ½-inch shaft

The deflection of the shaft under the boundary conditions for Case 3 was only modelled in Abaqus since the MATLAB results from Cases 1 and 2 were validated in Abaqus. Using the smaller water bath resulted in the lowest deflection of the three cases, 0.10 mm (Figure 3-32). This is expected since it is modelled with an additional roller connection closer to the point load.

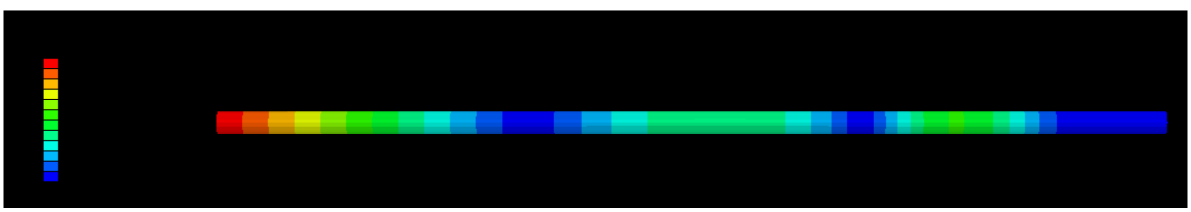

Figure 3-32: Case 3 deflection of 1/2-inch shaft with smaller test chamber

Further analyses show that using a 25.4 mm (1 in) diameter shaft significantly reduces maximum deflection of the shaft to approximately 0.04 mm at the point of application of the load (Figure 3-33). Another future improvement to the design of this shaft is to use a stepped shaft so that the exact location of the bearings is easier to find. The shaft diameter should decrease at the point where the bearing is located.

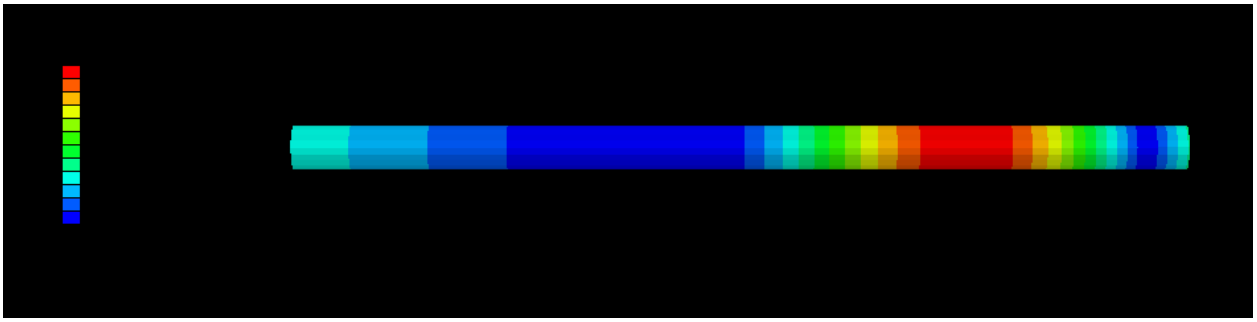

Figure 3-33: Deflection of 1-inch diameter shaft

Deflection of the shaft may cause leaking at the mechanical seals. Based on the tolerances of the seal provided by the manufacturer, the inner lip of the seal which maintains contact around the shaft has a tolerance of ± 0.0762 mm. The outer lip has a tolerance of 0.0254 mm. Therefore, the deflection of the shaft should not exceed the tolerances at the point of intersection with the mechanical seals. Since the points of intersection of the shaft with the seals were modelled as roller connections, it was assumed that no deflection would occur at these points. These results show that under a static analysis, the deflection of the shaft before and after the supports is minor. In addition, the shaft will not always be subject to the maximum load. Therefore, it is not necessary to simulate the dynamic conditions under which the shaft actually operates. The shear and moment diagrams for Case 2 are shown in Figures 3-34 and 3-35 respectively.

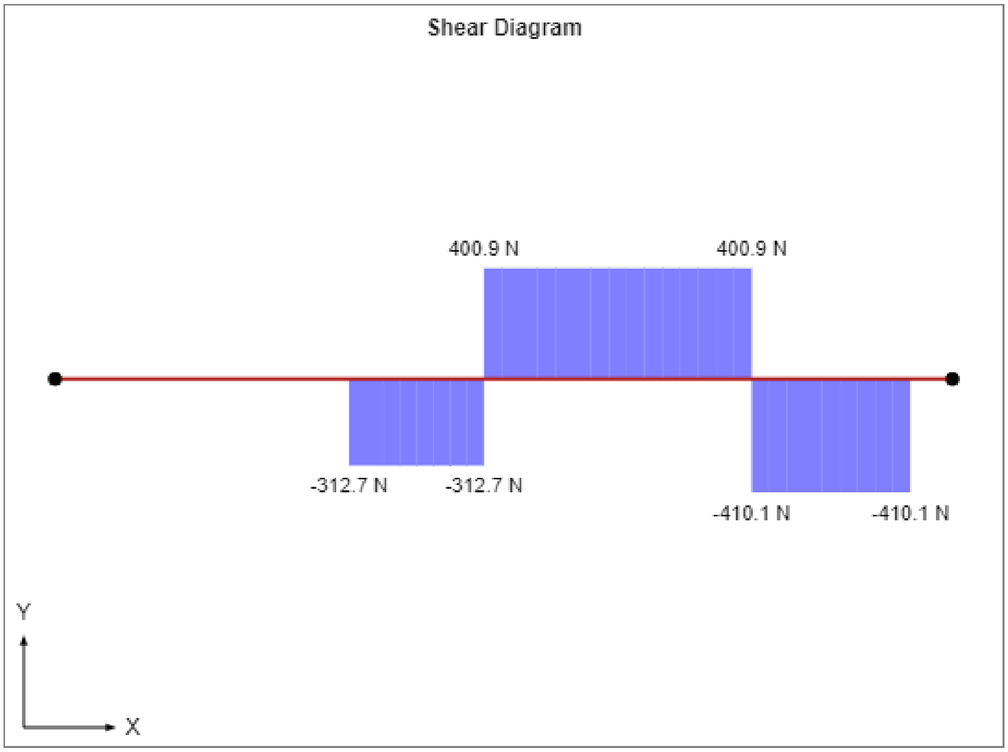

Figure 3-34: Shear diagram of the shaft in Case 2

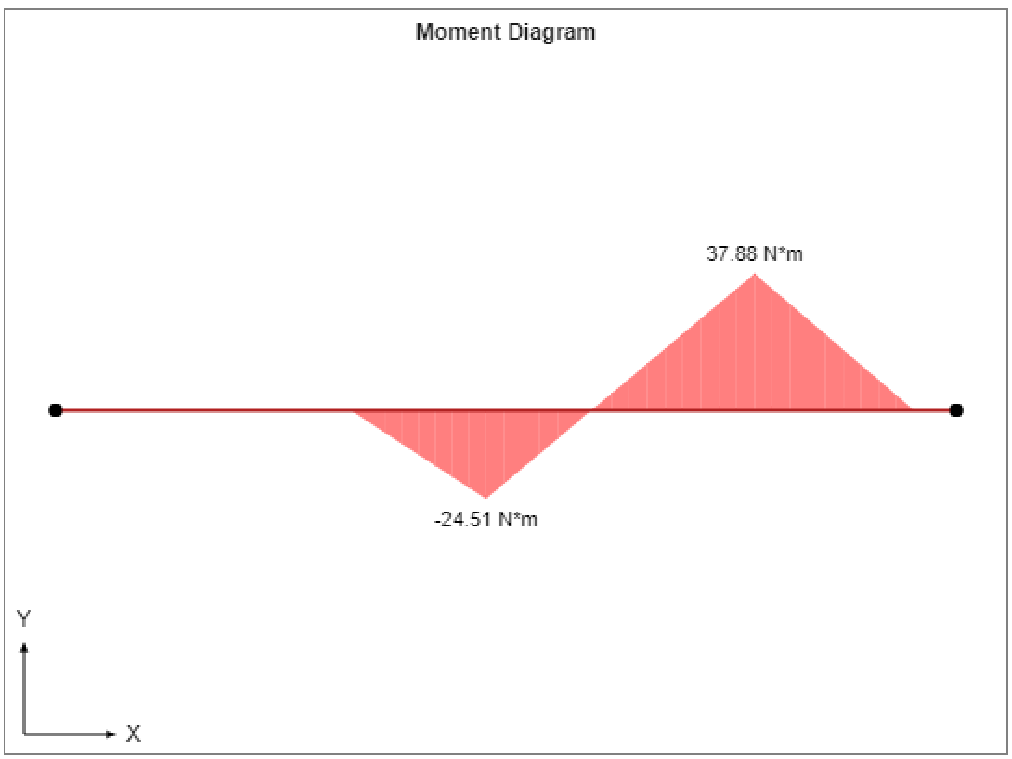

Figure 3-35: Moment diagram of the shaft in Case 2

3.5.2 Shaft Keys and Keyways

The four-bar mechanism translates rotary displacement from the pinned end of the rocker to the calcaneus jig. This is made possible by means of torque being transmitted from the shaft to the hub via shaft keys. There are three types of shaft keys:

1. Parallel keys
    a. Square
    b. Rectangular
2. Tapered keys
    a. Gib-head
    b. Plain tapered
3. Woodruff keys

Based on the design requirements and standards, this section focuses only on parallel keys. Parallel keys (Figure 3-36) may have either a square or rectangular cross section (W x L) that is constant throughout its length (L). When a parallel key is used, half of its height rests in the hub while the other half sits in the shaft.

Figure 3-36: Details of a parallel key

It was previously determined that using a 25.4 mm (1/2 in) diameter shaft is sufficient under the maximum loading conditions. ANSI B17.1-1967 is used to determine the dimensions of the hub, key and keyway based on the shaft diameter. ANSI standards suggest that a ½” diameter shaft uses a square parallel key rather than a rectangular one. Keys should have a tight fit in the shaft and a sliding fit in the hub. There should also be some clearance between the top of the key and the hub keyway. A Class 1 fit is appropriate for this application because one should be able to remove the calcaneus jig from the shaft with relative ease. This key cross section is too small to apply a fillet to its corners a radius to the keyway as per the design standards.

Table 3-3: Excerpt from ANSI B17.1-1967 Table 1 Key Size vs Shaft Diameter

Shaft Diameter (in)		**Width, W (in)**	**Height, H (in)**	**Nominal Key Seat Depth, H/2 (in)**
Over	**To**			
7/16	9/16	1/8	1/8	1/16

Table 3-4: Excerpt from ANSI B17.1-1967 Table 4 Standard Fits for Parallel & Taper Keys

Type of Key	**Key Width**		**Side Fit**			**Top and Bottom Fit**			
	Over	**To**	**Width Tolerance**		**Fit Range**	**Depth Tolerance**			**Fit Range**
			Key	**Key Seat**		**Key**	**Shaft Key Seat**	**Hub Key Seat**	
Class 1 Fit for Parallel Keys									
Square	0	½"	+0.000	+0.002	0.004 CL	+0.000	+0.000	+0.010	0.032 CL
			-0.002	-0.000	0.000	-0.002	-0.015	-0.000	0.035 CL

The length of shaft keys and hubs are typically 1.5 times the shaft diameter and should never extend beyond the hub by more than the rounded ends of the key. In addition, the hub diameter is typically twice that of the shaft diameter. However, the nature of this experiment requires the length of the calcaneus jig, which acts as a hub, to be 50 mm long. The distance from the top of the calcaneus jig to the radius of the shaft should also be 50 mm in order for it to remain in contact with the talus jig. A supplier provides the rigid shaft coupling welded to the rocker. While this rigid coupling meets the required hub diameter, it is twice as long as the recommended design value, 19 mm (¾"), since its purpose is to connect two shafts together.

Although the lengths chosen for both keys were longer than the prescribed length, they would not fail from shear failure (τ_{xy}) and bearing failure (σ_{xy}) due to the small magnitude of the cyclic load applied at the calcaneus jig. Bearing failure is the crushing of the key under a compressive load while shear failure happens when the key is sheared across its width. This is calculated using Equation 3-4. Shear failure occurs where the shaft and the hub meet and is calculated using Equation 3-5 (Norton, 2014). Although a dynamic load is applied to the shaft, the maximum load was used since bearing failure is only due to compression.

$$[Eq\ 3-4] \qquad \tau_{xy} = \frac{F}{A_{shear}} = \frac{F}{L \cdot W}$$

$$[Eq\ 3-5] \qquad \sigma_x = \frac{F}{A_{bearing}} = \frac{F}{L \cdot \left({}^{H}/_{2}\right)}$$

Figure 3-37 shows the key seats cut into the shaft to accommodate the calcaneus jig and the shaft coupling. Since the shaft coupling is at the end of the shaft, its key only requires one round end. The calcaneus jig is positioned between the ends of the shaft, therefore its key requires both ends to be rounded (Figure 3-38).

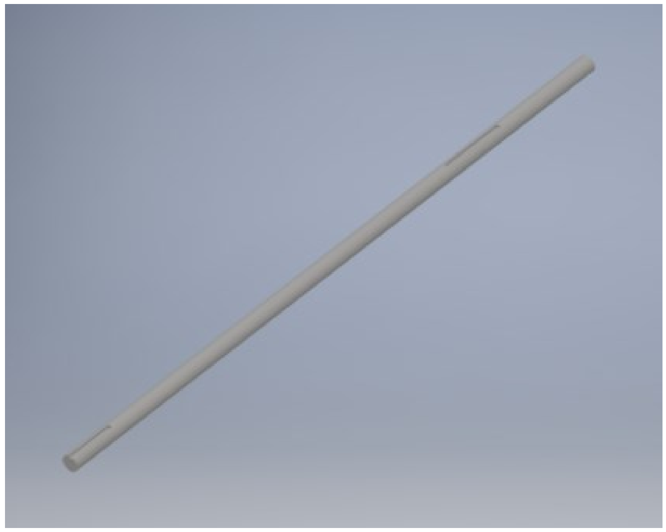

Figure 3-37: Shaft with key seats for calcaneus jig and rocker

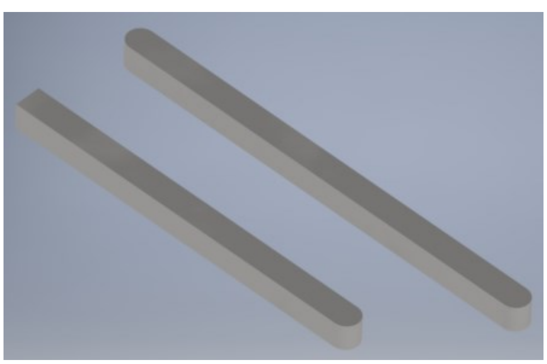

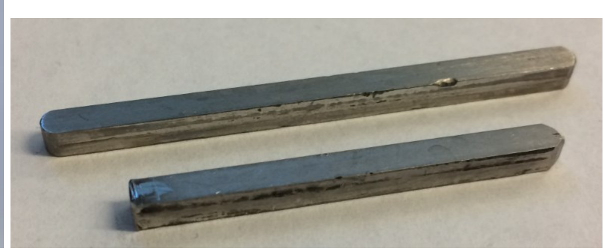

Figure 3-38: Shaft keys for coupling and calcaneus jig

3.6 Other Connections

When bolting two plates to each other, it is standard practice to make a clearance hole in the top plate and a threaded hole in the bottom plate as per Figure 3-39. This clearance is necessary to facilitate the alignment of the bolt in the holes. If the bolt holes in both plates were threaded, they would have to be clamped and tapped in unison so that no discontinuities exist in the thread pattern. Initially, this was overlooked and many of the tapped holes in the modified plate and the bearing spacers had to be drilled after receiving them from the manufacturer.

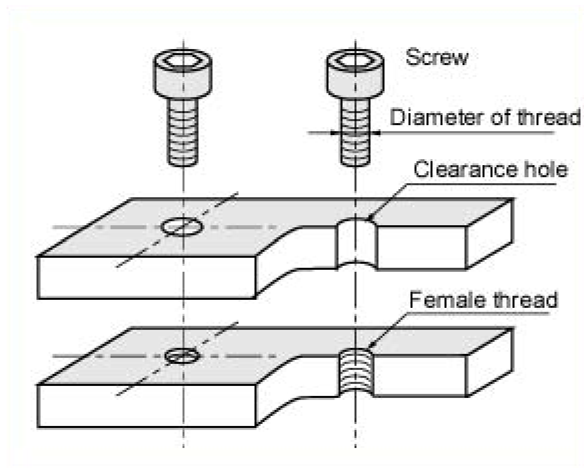

Figure 3-39: Clearance and tapped hole used to align two plates

Socket head screws connect all attachments to the motor, original and modified plates. Shoulder screws connect the crank and rocker to the coupler (Figure 3-40).

Figure 3-40: Socket head screws and shoulder screws. Retrieved from sandhuautoengineers.com

Lipped ball bearings (Figure 3-41) are used to facilitate the connection of the shoulder screws at the joints of the four-bar mechanism. Without ball bearings, motion of the four-bar mechanism would be restricted.

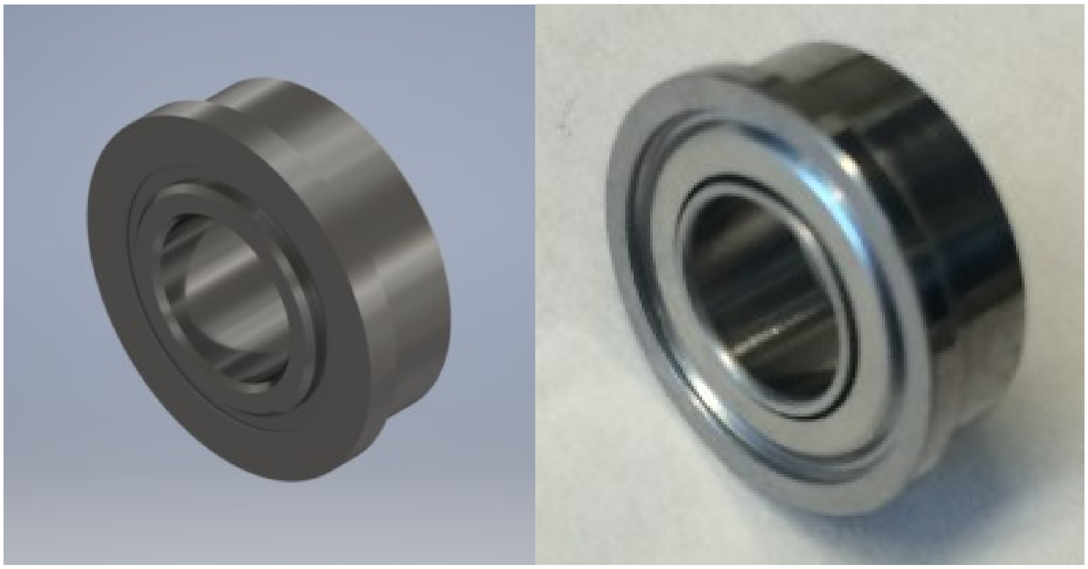

Figure 3-41: Lipped Ball Bearing

Shims, which are like washers with smaller outer diameters, are placed between the mating faces of the ball bearings and other objects. This is necessary to prevent the inner and outer races of the ball bearing from being compressed by the heads of the shoulder screws and the taper-lock bushing during rotation. If the inner and outer races of the ball bearings are compressed, the shield could fall off and the remaining parts of the ball bearing will fall apart. A strong adhesive is used to prevent the ball bearings from detaching from the linkages during rotation.

3.7 Electrical Components

Since flexibility is paramount to the design of this experimental setup, an AC motor is used to provide the input torque for this experiment. Connecting a variable frequency drive (VFD) to an AC motor allows the user to alter its speed to the desired frequency. Finite Element Analysis (FEA) is used to optimize the size of the motor required for this experiment and is discussed in detail in Chapter 4. Both the motor and VFD are purchased from a manufacturer with no means of direct connection to electrical outlets. This section describes how to connect the windings of a three-phase AC motor and how to connect the motor to a single-phase VFD.

3.7.1 Motor Connection

Every motor has a nameplate, which informs users of the proper connection for a specified voltage, the power rating and efficiency to name a few. Figure 3-42 depicts the nameplate of the three-phase motor used in this experiment.

Figure 3-42: Motor nameplate

From the nameplate, this motor runs on either 208-230/460 volts of alternating current. A delta connection (Figure 3-43b) is used for high voltage supply (460 V) while a star connection (Figure 3-43a) is used for low voltage supply (208-230 V).

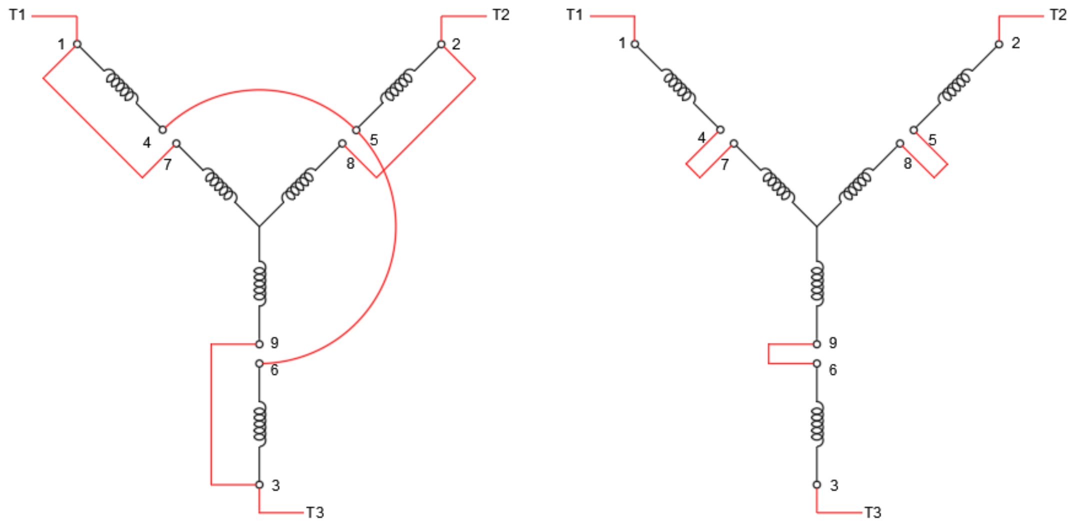

Figure 3-43: (a) Star connection and (b) delta circuit schematics

A single phase VFD transmits low voltage three phase current to the motor. Therefore, star connection is used to connect the stator winding of the motor. Within the power compartment of the motor are 9 terminal wires, labelled 1 – 9. As seen in the star connection schematic (Figure 3-43a), a neutral point is formed with wires 4, 5 and 6. The three windings (T1, T2 and T3) are connected to the VFD via a four-strand cable. First, an adequate length of the cable is stripped of its housing to expose the four strands of wire. Then, a cable gland is used to secure the exposed length of wire within the motor terminal box. Wire nuts secure the connection of the four-strand cable wires and terminal wires.

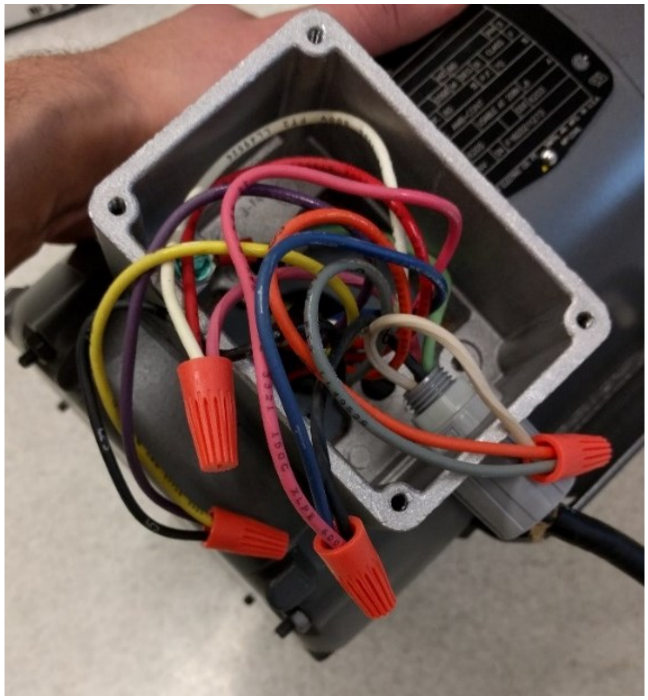

Figure 3-44: Motor wire connection

Table 3-5 details the wire colour code for Canada, based on the Canadian Electric Code (CEC). Based on Figure 3-43(a), the red wire (T1) from the four-strand cable is connected to terminals 1 and 7, the black wire (T2) to terminals 2 and 8 and the white wire (T3) to terminals 3 and 9. The exposed end of the green wire is attached to a wire connector with a spade terminal using an electrical crimper. Then, the green wire is screwed to the ground terminal in the motor. The next step involves connecting the exposed end of the four-strand cable from the motor to the VFD.

Table 3-5: Wire colour code for AC power circuits in Canada

Function	Label	Colour
Protective Ground	PG	Green or yellow-green
Neutral	N	White
Line, Single-Phase	L	Black
		Red (2nd hot)
Line, Three-Phase	L1	Red
Line, Three-Phase	L2	Black
Line, Three-Phase	L3	Blue

3.7.2 Variable Frequency Drive (VFD) to Motor Connection

In Canada, the power supplied to educational institutions is typically single-phase current. Traditional VFDs use three-phase current and output three-phase current. However, newer VFDs on the market use single-phase current and output three-phase current. Using a phase converting VFD for this experiment is convenient since it does not require an additional connection to three-phase power supply. Eaton manufactures the VFD used in this experiment. Its model number is MMX11AA3D7N0-0. This model converts single-phase input current to three-phase output. The user is given the ability to alter the frequency of rotation of the motor shaft from 0 to 320 Hz.

Using this particular phase converting VFD results in the frequency programmed by the VFD becoming half of the corresponding motor shaft frequency. For example, programming the VFD to 10 Hz gives a response of 5 Hz from the motor shaft. This is attributed to the phase conversion of the current.

Figure 3-45 shows a schematic for the connection of the motor and power supply wire leads to the VFD. A four-strand cable connects the motor to the VFD while a three-strand power chord connects the VFD to the AC power supply. Perform this connection while the power supply is off. Switching T1 with T2 would result in the shaft rotating anti-clockwise. However, the direction of rotation can be altered using a command on the VFD. Figure 3-46 gives a better visual of the actual motor and VFD in connection.

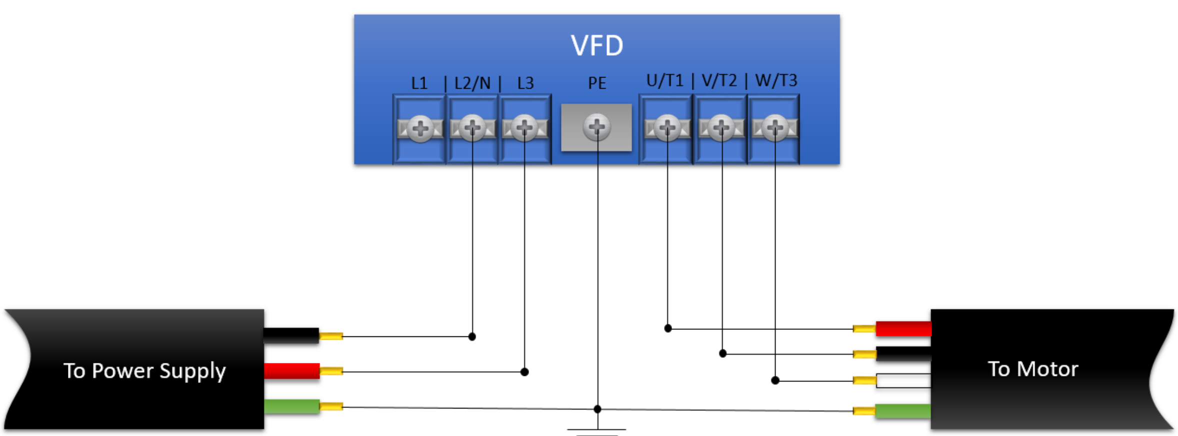

Figure 3-45: Schematic of motor and AC supply to VFD connection

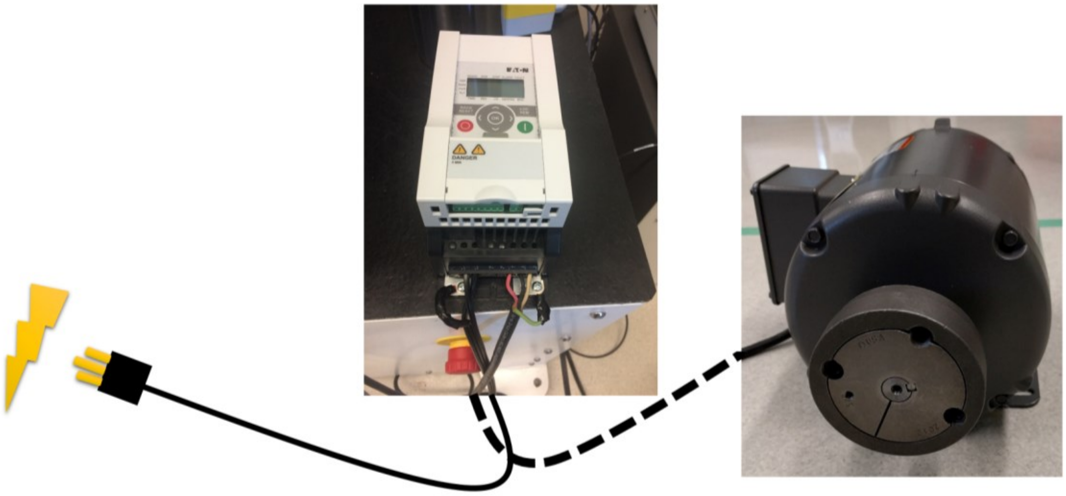

Figure 3-46: Connection of motor to VFD

3.7.3 Controlling the motor using the VFD

The VFD is programmable so that several parameters match the specifications of the motor it powers. This is necessary for accurate communication between the VFD and the motor. After powering the VFD, the default monitor screen is shown in Figure 3-47. Pressing the "OK" button will display the output frequency of the motor shaft connected to the VFD. To switch from the monitor menu (MON) to parameters (PAR), press the "BACK RESET" button and use the arrow down key to move the left pointing arrow from MON to PAR and hit "OK".

Figure 3-47: VFD output monitor after the power comes on

First, the quick start parameter P1.1 is set to "0" to allow the user to modify the factory settings of the VFD. Table 3-6 shows the specifications which were changed, and the new values used. Parameter 7 covers the information provided on the motor nameplate changed to match that of the motor nameplate. The values correspond to the low voltage (230 V) setting for the motor.

Table 3-6: Parameters changed on the VFD

Parameter	Description	Input
Parameter selection		
P 1.1	Quick start configuration	0 = All parameters
P 1.2	Application macro	0 = Basic
Drives Control		
P 6.1	Primary remote control source	2 = Control unit (Keypad)
P 6.2	Primary speed reference	1 = Keypad (REF)
P 6.3	Minimum frequency	0 Hz
P 6.4	Maximum frequency	60 Hz
Motor		
P 7.1	Motor rated current	0.8 A
P 7.3	Motor speed	1750 RPM
P 7.4	Power factor	0.70
P 7.5	Motor voltage	230 V
P 7.6	Motor rated frequency	60 Hz
V/Hz Characteristic Curve		
P 11.8	Motor control mode	1 = Speed control (vector)

Since the incorporation of an analog source is absent from the electrical component of this experimental setup, the VFD keypad is used to power the motor and adjust the speed of its shaft. Therefore, the Drives Control parameters are adjusted accordingly so that the keypad is the source of control. However, it is desirous to connect the VFD to the fatigue-testing machine and control it with a computer program in the future. To allow for analog control, P 6.1 should be changed to "1" and P 6.2 to "3". Then, the Motor parameters should be adjusted to reflect the relevant information from the motor nameplate.

Timely response of the motor to the speed commanded by the VFD and consistency of the desired speed is vital for the success of this experiment. For this reason, one should switch the V/Hz Characteristic Curve parameter from frequency control to vector control. Vector control, also known as field-oriented control (FOC), is better suited for a dynamic environment. Kohlrusz and Fodor (2011) concluded that FOC has a faster response compared to scalar control and is better at handling transients. This justifies why the speed of the motor shaft is not accurate enough when the motor control mode was set to frequency control.

After setting the VFD to the desired frequency, the user can verify the speed of the motor shaft in revolutions per minute by switching to the monitor panel on the VFD. A tachometer (Figure 3-48), which measures the speed of rotating shafts, confirmed that the speed monitored by the VFD corresponds to the speed of the motor shaft. By placing reflective tape on the shaft and pointing the tachometer at it, one can easily read off the speed of the rotating shaft on the monitor of the tachometer.

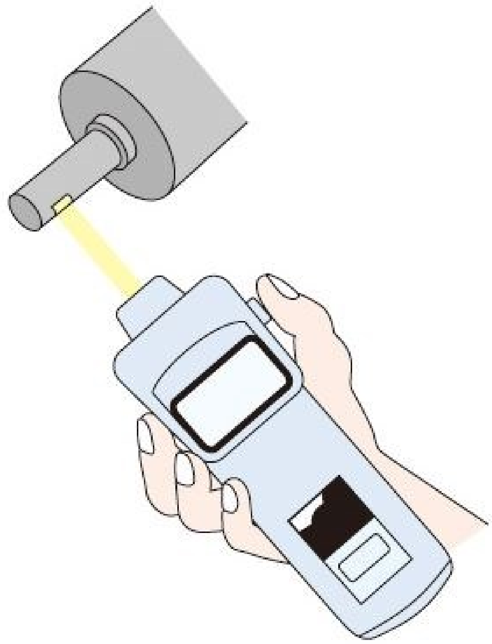

Figure 3-48: Tachometer measuring speed of shaft (RPM) using reflective tape. Retrieved from nidec-shimpokeisoku.jp

3.8 Assembly of Experimental Setup

The next step involves assembling all the mechanical and electrical components of the test set up. To minimize the possibility of running into obstacles and tight fits, the user should mount the parts in the following order:

1. Connect the motor to the VFD as instructed in section 3.4.
2. Dismount the load cell, shaft extension and water bath from the fatigue-testing machine as per Figure 3-49(a).
3. Remove the four bolts at each corner of the original plate, but do not remove the plate from the stands.
4. Align the modified plate by the four holes at its corners with the original plate. Use M8 x 1.25 bolts and their corresponding oversized washers to secure the two plates at each corner to the four cylindrical stands as per Figure 3-49(b).
5. Mount the motor plate using M8 x 1.25 mm bolts, washers and spacers as per Figure 3-50.
6. Apply a layer of silicon around to seal the drainage hole of the original and modified plates.

7. Fit the O-ring in the groove of the modified plate.
8. In this case, the vertical holes for the water bath are misaligned by 1/16" in comparison to those drilled into the original plate. Therefore, replace the original M6 x 1 mm bolts with smaller M4 x 0.7 mm bolts to half align the water bath, making them off by 1/32" along both edges of the vertical holes. Using smaller bolts in much larger holes requires nuts and washers placed beneath the original plate to secure the M4 x 0.7 mm bolts in place. Refer to Figure 3-51.
9. The motor plate interferes with the placement of these bolts along the left half of the water bath. Use C-clamps to apply compression to the left half of the water bath. The C-clamp should encompass all three plates and the water bath as shown in Figure 3-52.
10. Insert the taper-lock bushing through the motor shaft until its face is flush with the exposed end of the motor shaft (Figure 3-53). The manufacturer will provide instructions on how to mount the bushing and hub to a shaft. Mount the motor from its base to the motor plate using washers and nuts (Figure 3-54).
11. Mount the stainless steel spacer and corrosive bearing block inside the water bath using the M10 x 1.5 mm black oxide bolts and corresponding stainless steel washers. We used extra washers this time because the desired bolt length is not available from manufacturers.
12. Remove the key at the end of the ½" shaft and keep the key towards the middle of it attached. Place the end of the shaft with no keyway cut through it through the shaft hole of the corrosive ball bearing. Ensure that the keyways cut in the shaft are face up.
13. Place the double-lip seal in its designated hole in the water bath cover. Then, slide the water bath cover through the hole along the exposed end of the shaft until it gets to the opening on the face of the water bath. Ensure that the side with the exposed lip seal is towards the inside of the water bath and the seal is oriented to the bottom of the bath cover. Secure the water bath cover by attaching the binding barrels to the threaded rods.
14. Align the holes in the carbon steel spacer with its designated threaded holes in the modified plate. Insert the mounted ball bearing through the exposed end of the shaft and secure it to the spacer and modified plate using the M10 x 1.5 mm bolts and spacers.
15. Reattach the key in the keyway on the cantilevered end of the shaft. Pull out the shaft from the corrosive block inside the water bath and insert the calcaneus jig through the

end of the shaft within the water bath. Ensure that the calcaneus jig aligns with the key on the shaft. Figure 3-55 shows the progress from steps 11 to 15.

16. Attach the rocker to the cantilevered end of the shaft via the rigid shaft coupling. Use the appropriate Allan key to secure the rigid coupling to the shaft via its setscrews. Place the lipped end of the bearing facing the front of the ½” hole in the rocker.
17. Place one lipped ball bearing in each of the ½” holes of the coupler. Both of the lipped ends should be on the same face of the coupler. Mount the coupler behind the rocker, with the lipped end facing the water bath cover.
18. Place the bearing that looks like a thick washer between the mating faces of the rocker and coupler. Then, insert the longer shoulder screw through these three components. Place two nuts on the threaded end of the shoulder screw to secure it. Refer to Figure 3-56 for clarity.
19. Ensure that the lipped end of the bearing on the other end of the coupler is in contact with the face of the taper lock bushing. Use the shorter, stainless steel shoulder screw to fasten the rocker to the taper-lock bushing by hand. Tighten the shoulder screw with the appropriate Allan key (Figure 3-57).
20. Screw on the load cell to the actuator preferable at eye level. Attach the load cell to the cable that connects it to the fatigue-testing machine. Orient the cable such that the letters on the wires correspond to the letters on the load cell.
21. Loosen the three bolts on each side of the cross head using the drive torque wrench. Press the blue button to activate the lever and raise the cross head high enough so that the shaft can be attached without interfering with the calcaneus jig.
22. If using the longer shaft, place two nuts and two washers at the centre of an M16 threaded bolt (Figure 3-58). Fasten one end of the bolt to the load cell. Attach the shaft to the exposed end of the bolt. Use a level to ensure that the shaft is plumb.
23. If using the two shorter shafts, bolt the two shafts together and attach the end with the shorter shaft to the load cell.
24. Fasten a threaded bolt all the way into the talus jig. Then, place a nut on the exposed end and fasten the bolt to the load cell. Position the talus jig so that the mating surface will be aligned with the calcaneus jig and use a wrench to tighten the nut in this position. You can use a thread adhesive to keep the talus jig fastened securely to the shaft.

25. Attach the implants to the talus and calcaneus jigs.
26. Lower the cross head of the motor until there is about a 1 mm gap between the two surfaces of the implants (Figure 3-59). Use the torque wrench to tighten the bolts of the crosshead. Deactivate the lever.
27. Ensure that the knob of the drain is perpendicular to the drain and fill the test chamber with the immersion fluid to the desired level.
28. Plug in the VFD to a circuit breaker.
29. You are now ready to begin running experiments. The complete test set up should mimic either Figure 3-60 or Figure 3-61 depending on which extension shaft is used.
30. Place the yellow guard over the four-bar mechanism and attach it to the modified plate by bolting on the ¼” shoulder screws through its arms (Figure 3-62).
31. For the final setup using the smaller test chamber, refer to Figure 3-63.

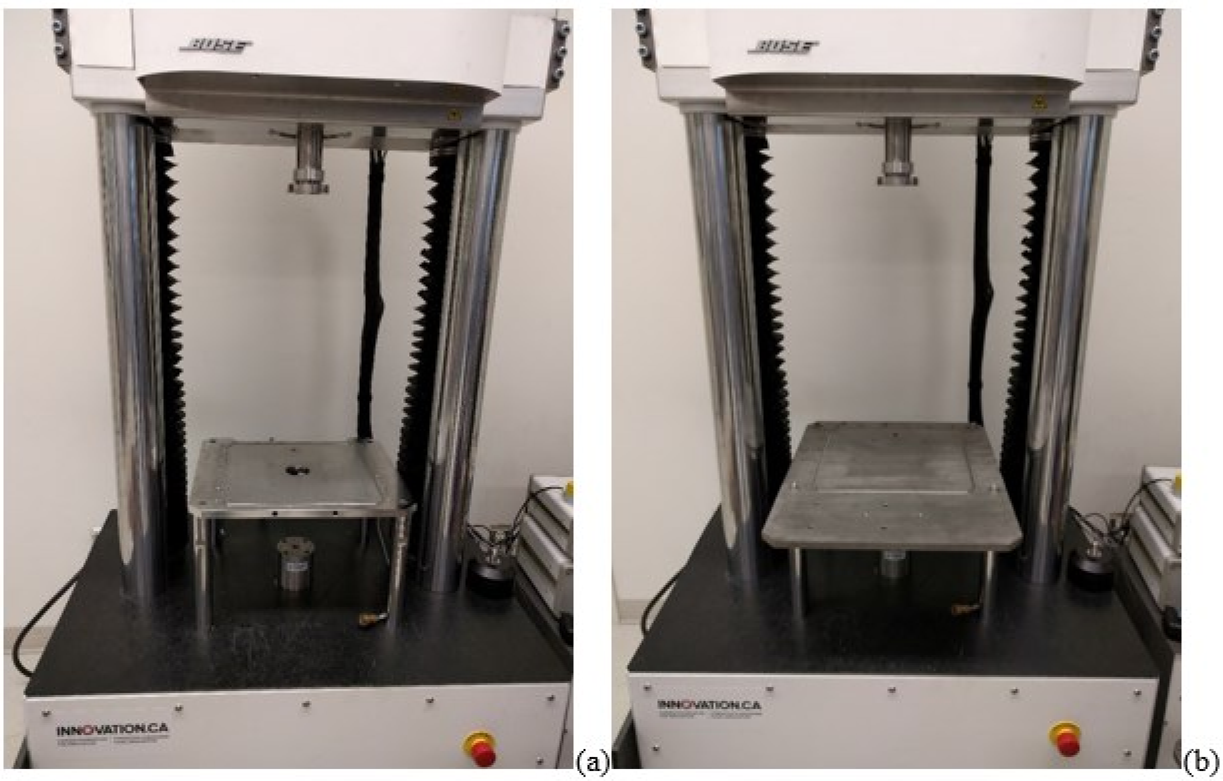

Figure 3-49: (a) Fatigue testing machine with original steel plate (b) Modified plate mounted on top of original steel plate

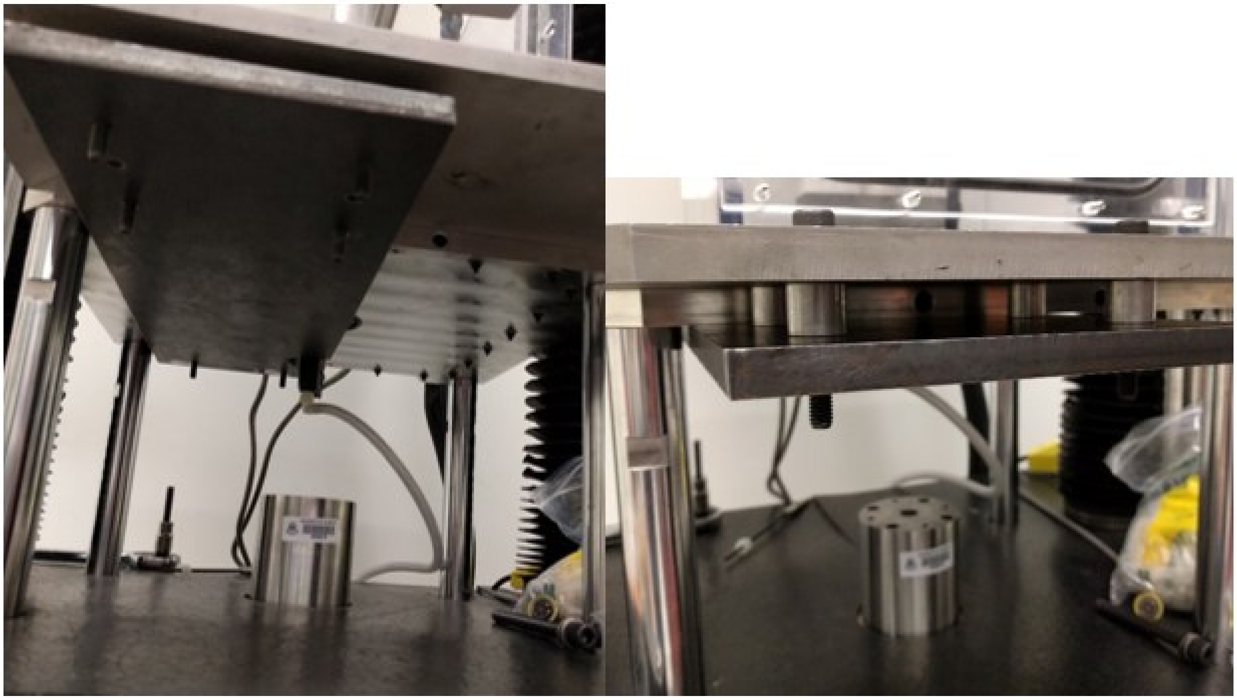

Figure 3-50: Motor plate mounted below the original and modified plates

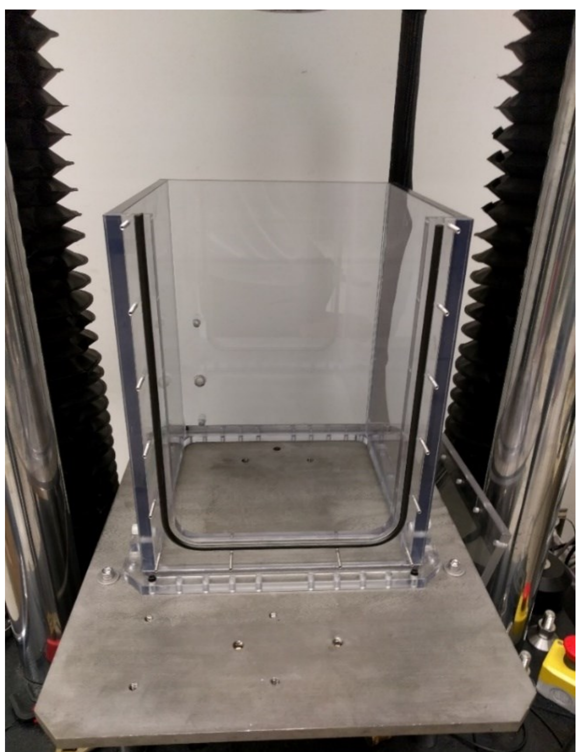

Figure 3-51: Water bath with threaded rods half-aligned on top of modified steel plate

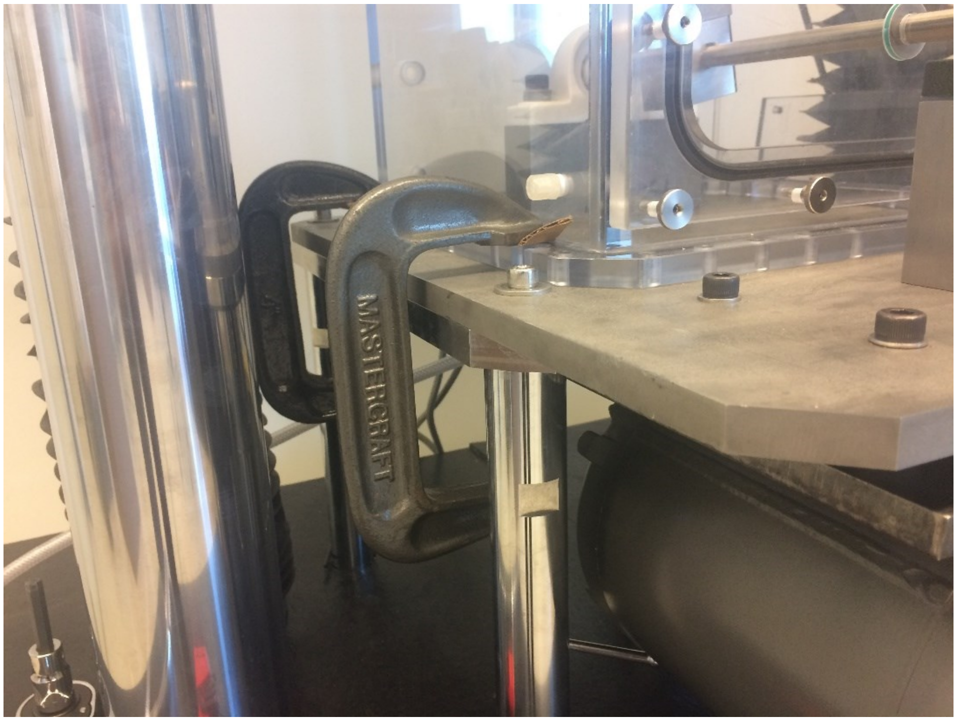

Figure 3-52: C-clamps applying compression to the left side of the water bath

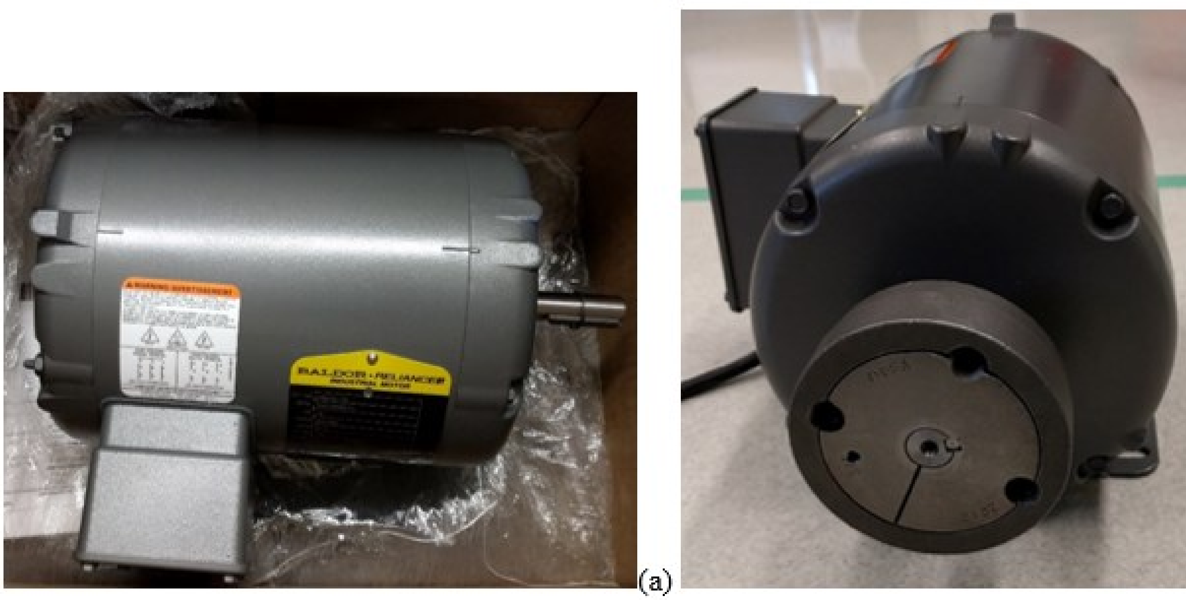

(a) (b)

Figure 3-53: (a) Original motor (b) Taper-lock bushing installed on shaft of motor

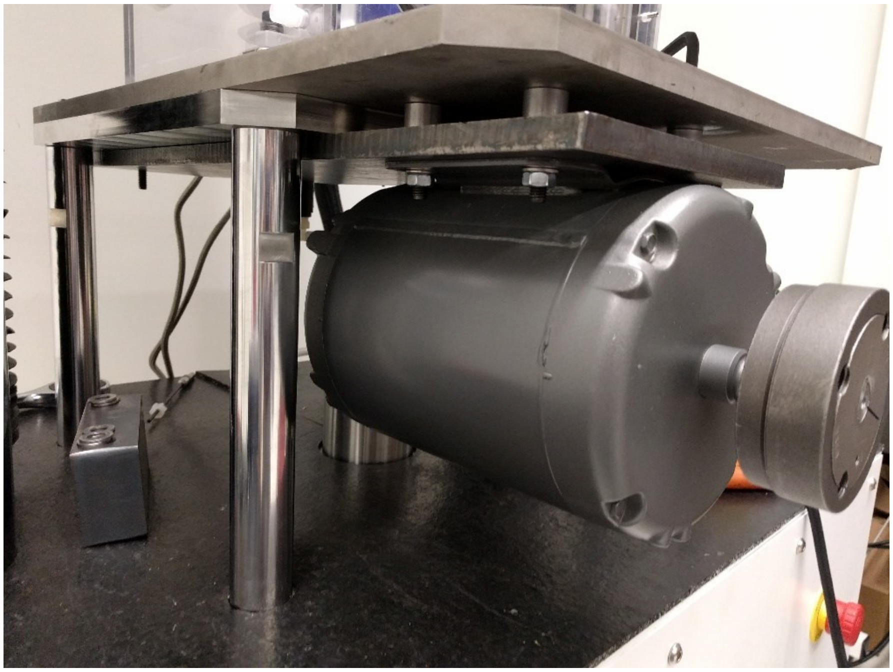

Figure 3-54: Motor base mounted to the bottom of the motor plate

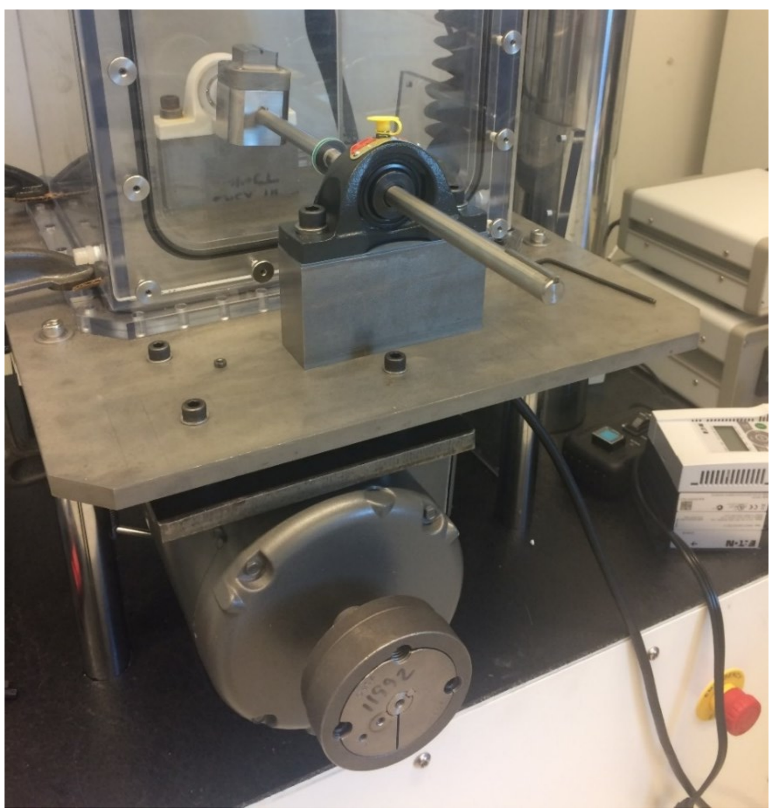

Figure 3-55: Shaft, mounted bearings, calcaneus jig and water bath cover installed

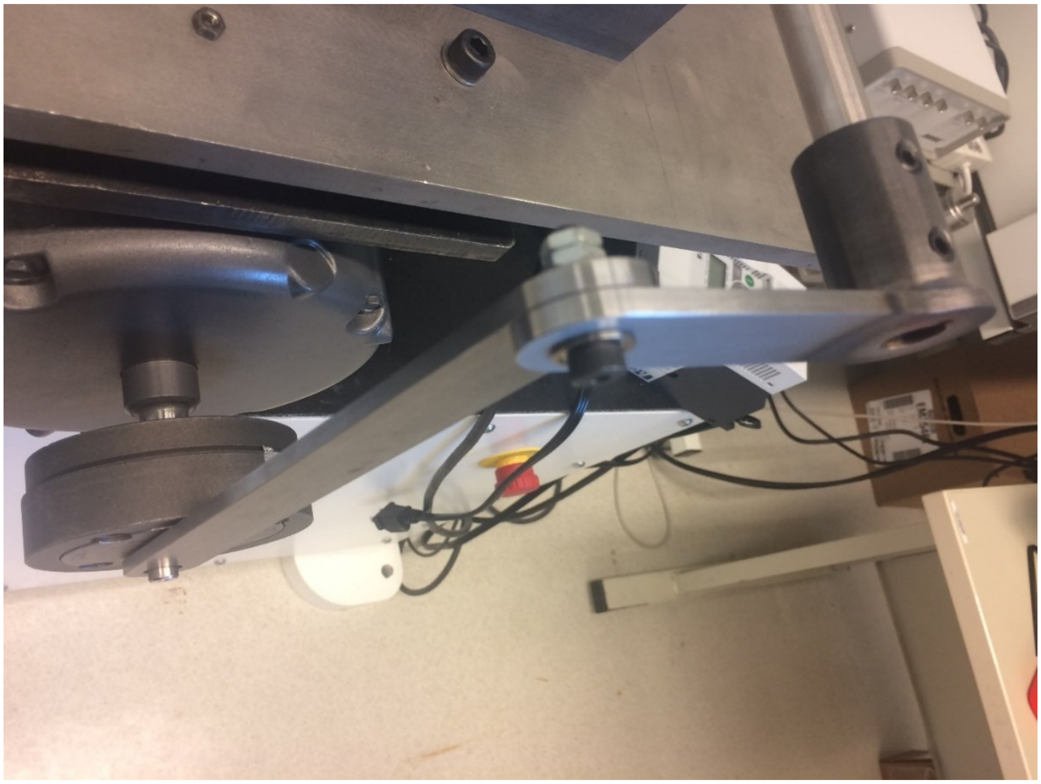

Figure 3-56: Attachment of the rocker to the shaft and the coupler

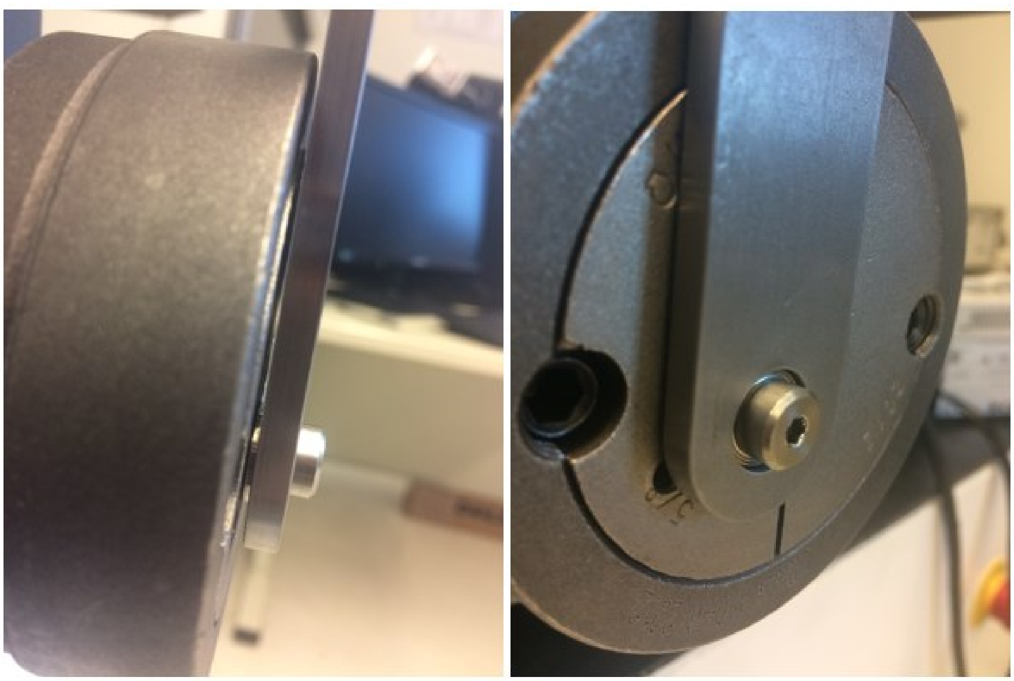

Figure 3-57: Attachment of coupler to taper-lock bushing via shoulder screw and ball bearing

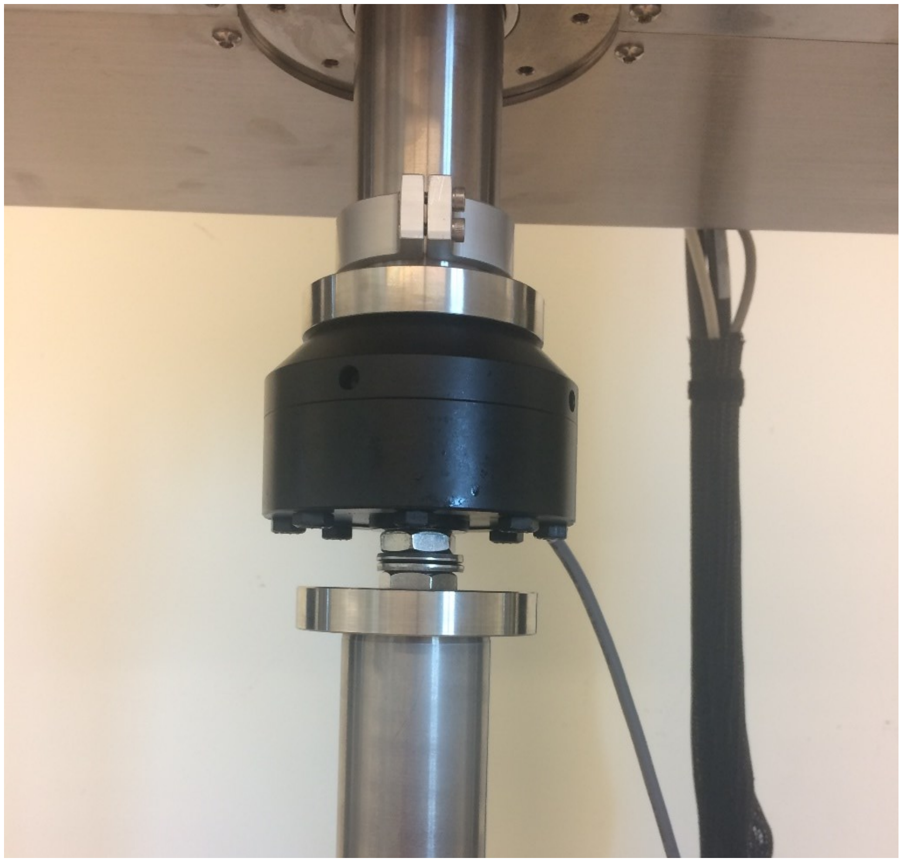

Figure 3-58: Nuts and washers used to connect longer shaft to the load cell.

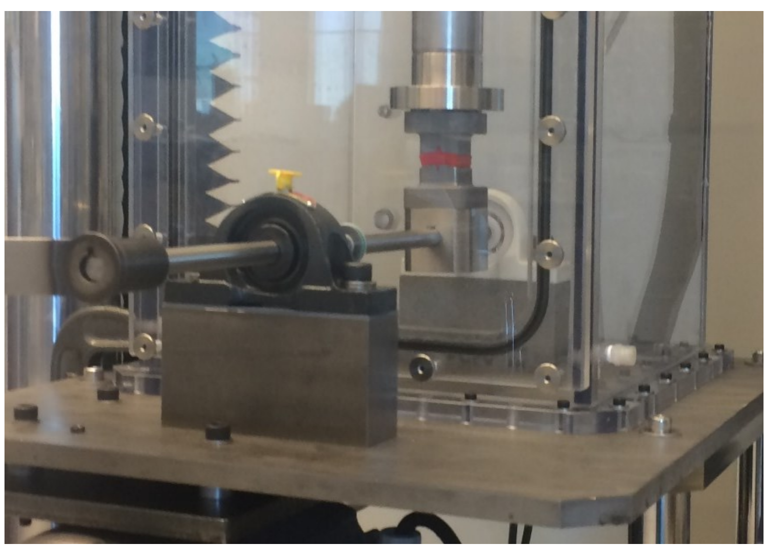

Figure 3-59: Talus and calcaneus jigs aligned and in contact with each other

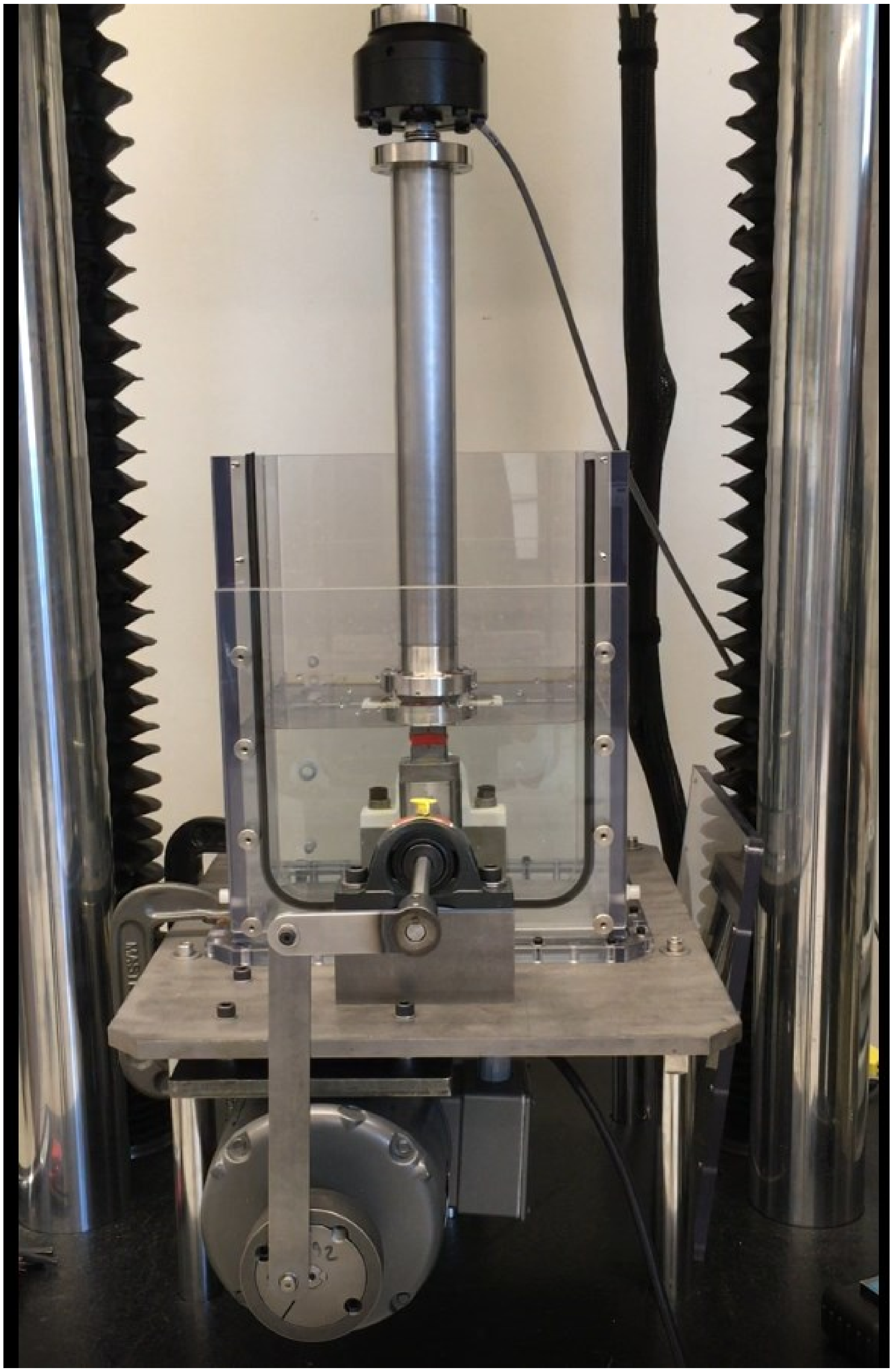

Figure 3-60: Complete assembly of test setup using longer shaft

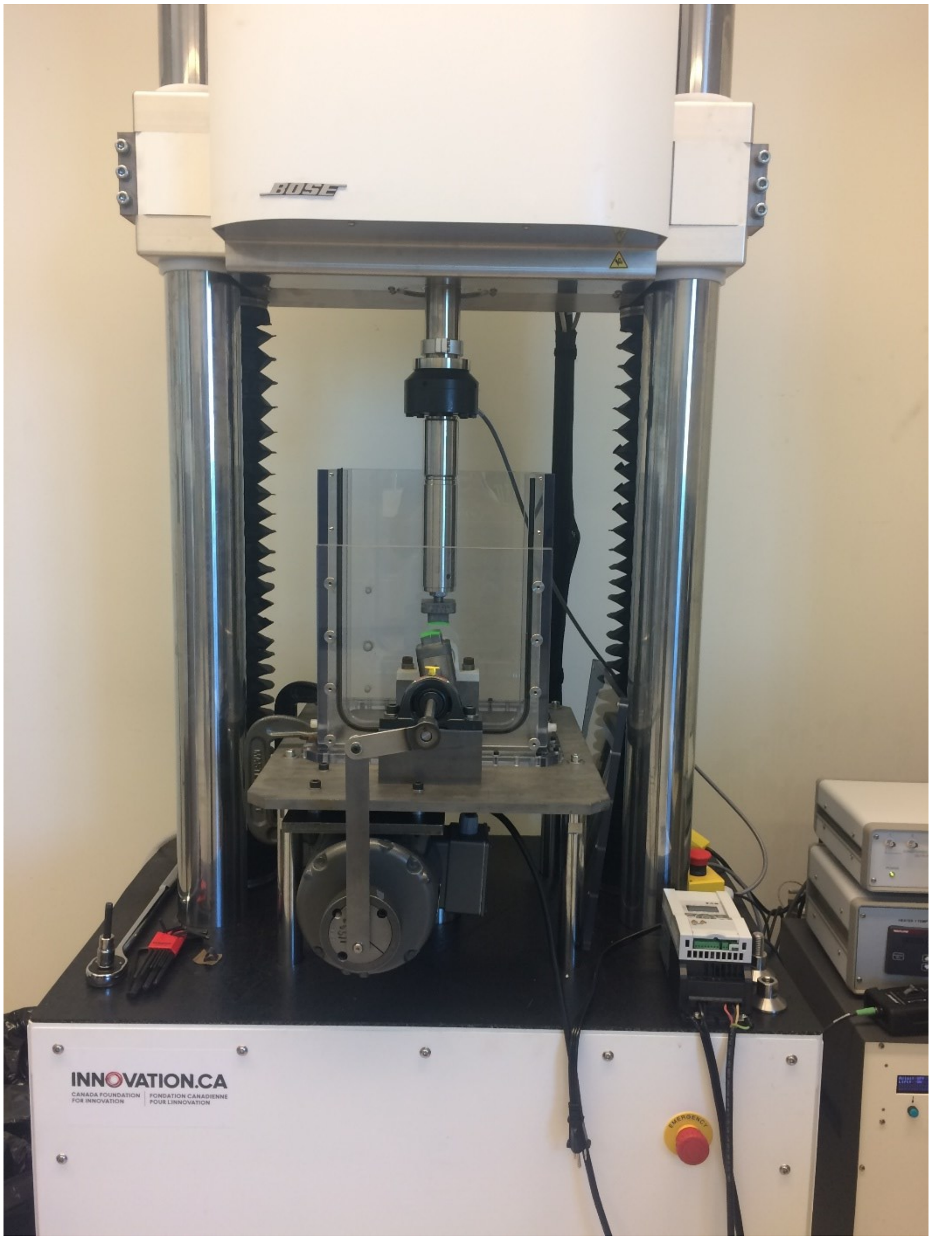

Figure 3-61: Complete assembly of test setup using shorter shafts

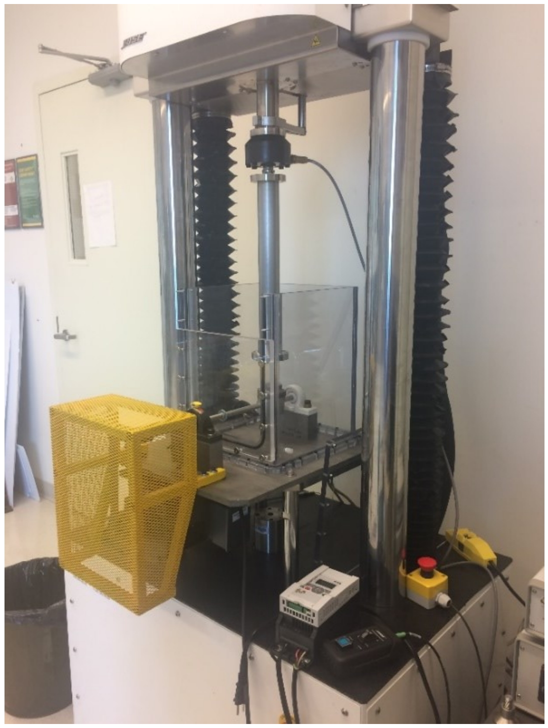

Figure 3-62: Protective guard placed over four-bar mechanism

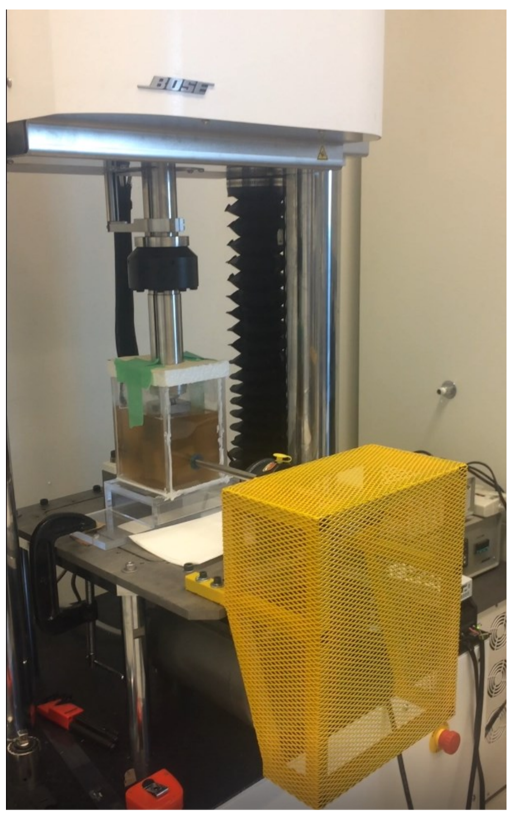

Figure 3-63: Complete assembly of test setup using smaller test chamber

Chapter 4 Finite Element Analysis of Four-Bar Mechanism

4.1 Introduction

Designing the four-bar crank rocker mechanism only determines the length of each linkage required to output a specified angle. The experimental setup specifies that the implants should be tested for wear every 1 million cycles for a total of 5 million cycles. Therefore, the possibility of failure from fatigue should be determined. In addition to failure from fatigue, the cyclic loading applied to the shaft results in an applied moment that the mechanism is required to overcome. This moment results from inertia effects and from the resistance provided by the friction between the mating surfaces of the implants. These factors should be considered prior to determining a suitable cross section for each of the linkages and the magnitude of the input torque that drives the system under steady state conditions.

Traditionally, a dynamic force analysis is used to determine the input torque of a four-bar mechanism. While this method of analysis considers the mass of each linkage, which is the result of the size of the cross section, it does not indicate failure from fatigue. For this reason, Finite Element Analysis (FEA) is performed using Abaqus/CAE 6.14-2 to test different cross sections for the four-bar mechanism under the specified loading conditions. A dynamic explicit analysis is run in Abaqus since it allows displacement and load to be entered as amplitudes. This emulates the rotation of the crank provided by the motor and the cyclic load from the fatigue-testing machine. To determine whether the linkages will be subject to failure from fatigue, the difference between the minimum and maximum principal stresses of each linkage is calculated.

4.2 Methods

4.2.1 FEA Model of the Four-Bar Mechanism

To reduce computation time, a 2D model is created. Each linkage is modelled as a separate 2D deformable wire in the +10° displacement orientation of the four-bar mechanism. Pinned connections are applied at the ends of the crank and rocker as shown in Figure 5(b). This is done by setting U1=U2=0 under the Boundary Conditions module and is essential for the rotation of the crank. Tie constraints with untied rotational DOFs are then added at the two points connecting the linkages to each other. These constraints enable the crank to make complete revolutions while the rocker goes from its maximum to minimum positions. Adjusting the settings to record output every

0.01 seconds allows the user to see the mechanism rotating at the end of the analysis. Figure 4-1 shows a schematic of the 2D model of the mechanism in its initial +10° orientation generated by Abaqus. The blue triangles represent the pinned joints while the blue dots represent the tie constraints applied at the ends of the linkages to enable rotation of the free end of the crank. M represents the moment amplitude applied at the pinned end of the rocker, and the rotary amplitude, 10π rad/s, represents the speed of the motor attached to the crank.

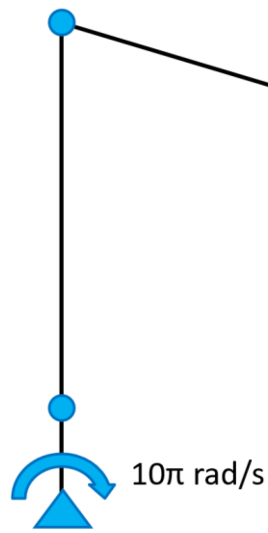

Figure 4-1: Schematic of 2D model created in Abaqus

Then, each part is defined as a beam element with a solid rectangular cross section (5 mm x 25.4 mm) and structural steel material properties defined in Table 4-1. The nature of this simulation requires a dynamic explicit analysis. Therefore, the density of the material is defined and amplitudes are used to define loads and displacement.

Table 4-1: Material Properties

Property	**Value**
Young's Modulus, E	200 GPa
Density	7850 kg/m^3
Poisson's Ratio	0.3

It is assumed that the contact between the two oscillating implants will provide some friction that is required to be overcome by the motor. Therefore, using just a half sine wave of vertical load oscillating from 50 – 800 N at 10 Hz inaccurately describes the load on the shaft for this analysis. To represent the effect of the applied load at the pinned joint in a 2D analysis, the load is converted into a resultant moment. Considering the 50 mm radius between the shaft centre and the convex surface of the calcaneus jig and setting the coefficient of friction (μ) as 0.3, the changing moment in time is calculated as shown in Figure 4-2.

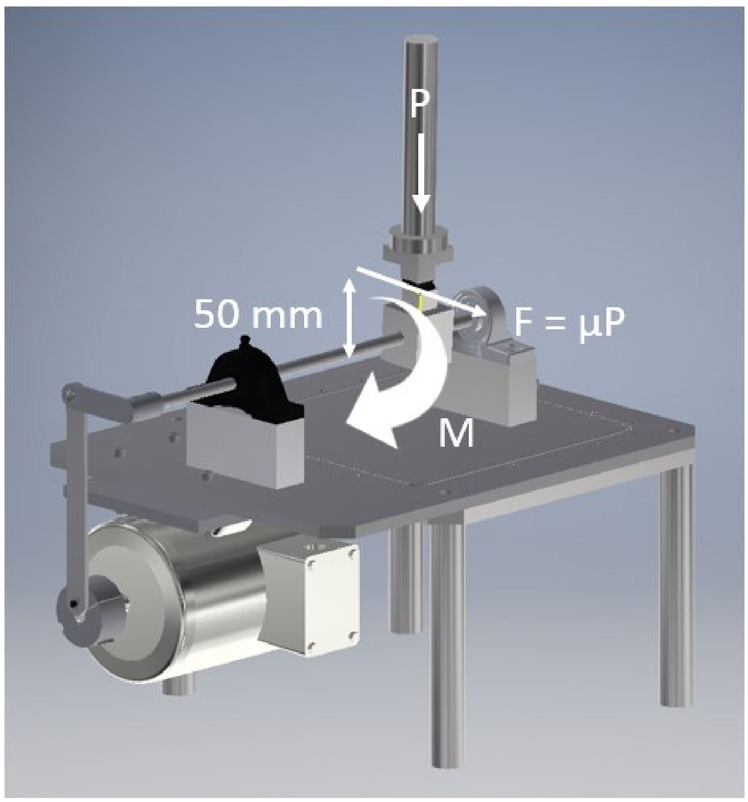

Figure 4-2: Conversion of applied load to moment

A sample calculation for the applied moment is demonstrated in Table 4-2. Figure 4-3 depicts the amplitude of the applied moment with time, which takes into consideration the relative motion of the two rotating parts with respect to each other. It should be noted that the initial moment applied corresponds to the maximum position (+10° rotary displacement) of the four-bar mechanism.

Table 4-2: Reaction Moment due to applied cyclic load

Time (s)	Force, F (N)	Friction Force, 0.3F (N)	Moment, M (N-m)	Step function			Moment, M (N-m)
0.00	800.00	240.00	12.00	0.00	1.00	1.00	12.00
0.01	728.38	218.51	10.93	-0.31	0.00	-1.00	-10.93
0.02	540.88	162.26	8.11	-0.59	0.00	-1.00	-8.11
0.03	309.12	92.74	4.64	-0.81	0.00	-1.00	-4.64
0.04	121.62	36.49	1.82	-0.95	0.00	-1.00	-1.82
0.05	50.00	15.00	0.75	-1.00	0.00	-1.00	-0.75

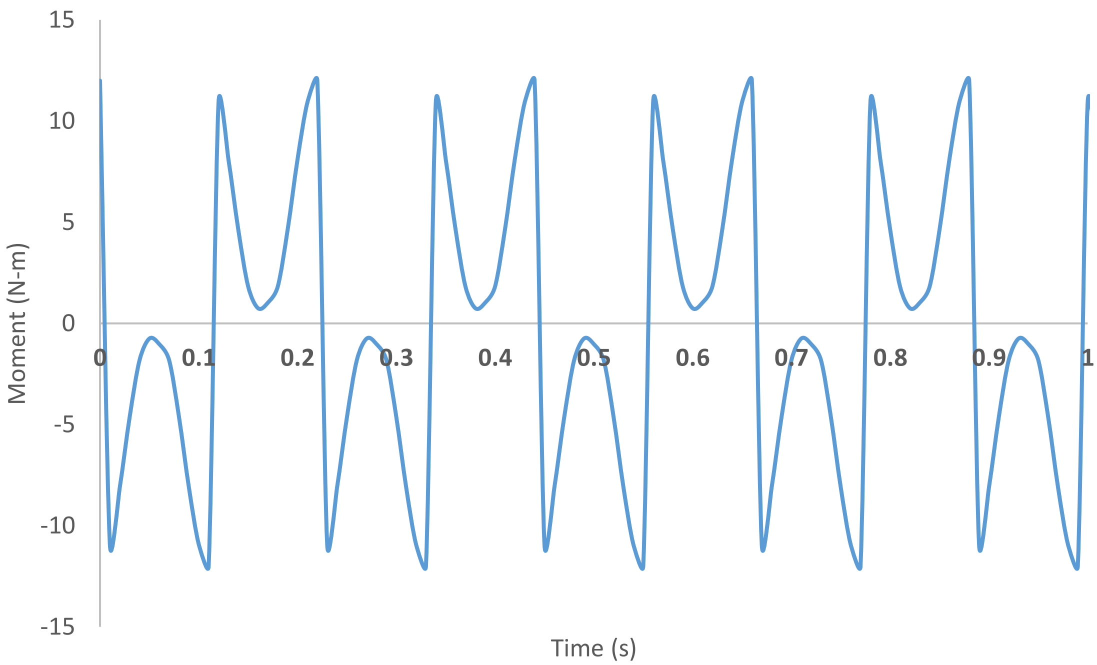

Figure 4-3: Applied moment with time

Based on the test parameters, the required frequency of inversion/eversion is 5 Hz. To simulate rotation of the crank in Abaqus, one should apply an angular displacement at the crank in the form of an amplitude. Therefore, Equation 4-1 is used to convert the frequency into angular frequency, which measures the rate of change of angular displacement with time. From the calculation, the angular frequency was found to be 10π rad/s. The cumulative angular displacement after 10 seconds is shown in Figure 4-4.

$$[Eq\ 4-1]\ \omega = 2\pi f$$
$$= 2\pi(5)$$
$$= 10\pi\ rad/s$$

where:

ω = Angular frequency (rad/sec)

f = Frequency (Hz)

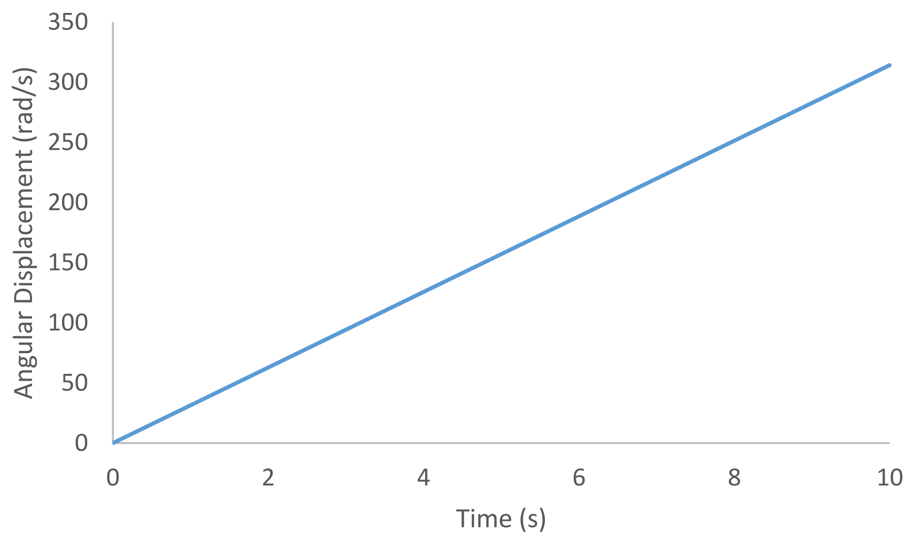

Figure 4-4: Rotary displacement with time

To account for the fatigue limit, the minimum and maximum principal stresses are recorded along the length each linkage. The input torque required to drive the system is determined by the reaction moment extracted at the pinned end of the crank. It was later decided to perform the experimental wear tests at 3 Hz instead of 5 Hz. Therefore, another model is analyzed with moment and rotation amplitudes corresponding to 3 Hz.

4.3 Results

4.3.1 Deformed Shape

Although the analysis was set to run for 10 seconds, it aborted after 4 seconds initially. This is due to the large deformation of the crank shown in Figure 4-5. The rocker and coupler are unaffected after this analysis. Considering the lengths of the coupler and rocker in comparison to the crank and the fact that the crank is responsible for rotating both linkages in addition to overcoming the applied torque, such a large deformation in Abaqus is reasonable. However, this will not be the case in the actual experiment. In reality, the crank linkage, is replaced with a much thicker taper-lock bushing, which is better suited for the rotary motion and is made to be attached to the shaft of a motor.

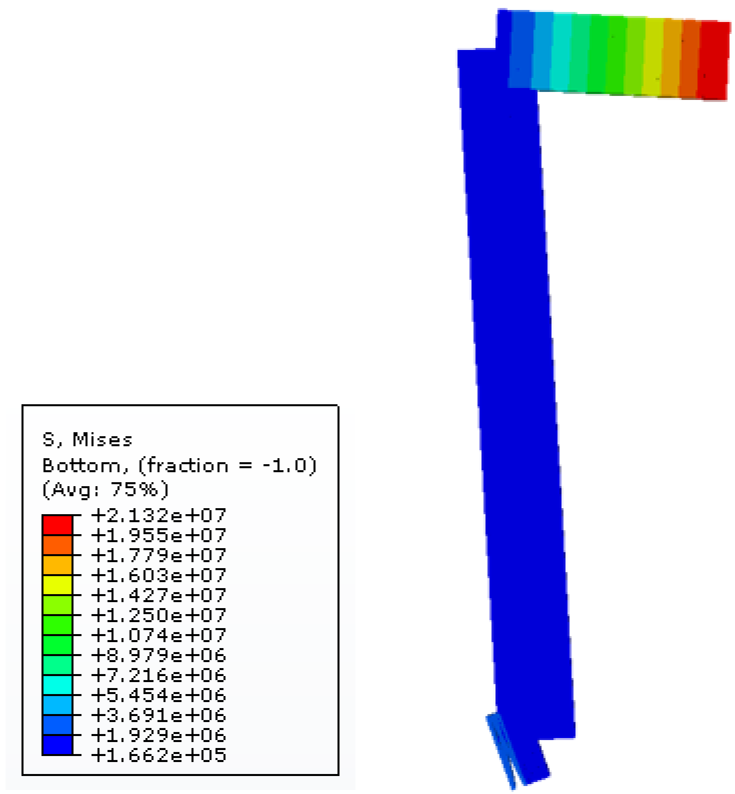

Figure 4-5: Deformation of four-bar mechanism after analysis

Changing the job precision from “single” to “double – analysis only” in Abaqus allows this analysis of a four-bar mechanism to run for the entire 10 seconds. Double precision is necessary to account for the accumulating errors after each iteration of a dynamic explicit analysis. While all the linkages are subject to stresses, there is no deformation in the crank although its cross-sectional thickness was not increased (Figure 4-6).

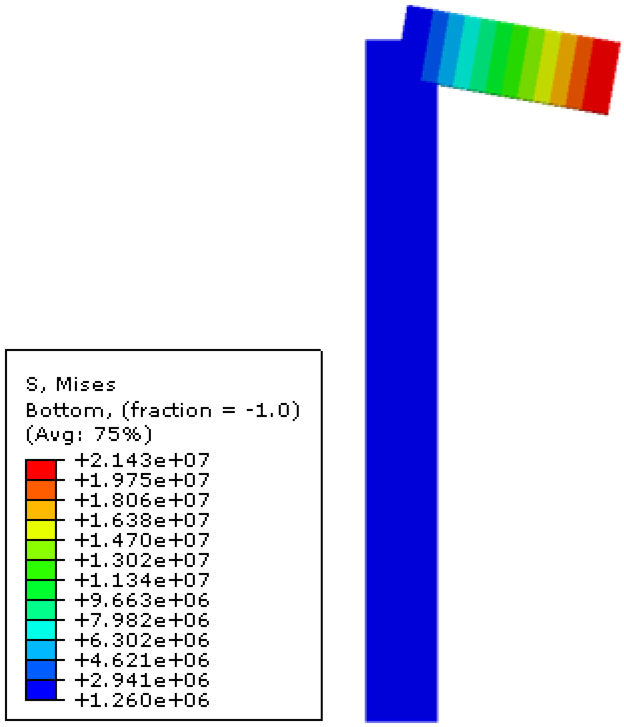

Figure 4-6: Undeformed four-bar mechanism after analysis with double precision

Figure 4-7 shows the undeformed shape of the four-bar mechanism under the 3 Hz loading analysis. The maximum von Mises stress in this case is only slightly less than the initial 5 Hz loading analysis. Therefore, a similar trend is expected for the minimum and maximum principal stresses along the linkages. The built equipment designed for 5 Hz rotation will function normally under 3 Hz rotation.

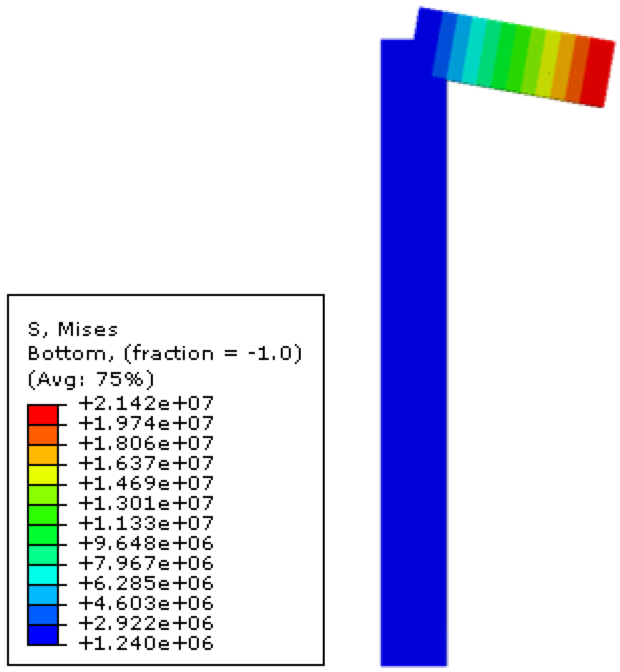

Figure 4-7: Undeformed four-bar mechanism using 3 Hz loading condition

4.3.2 Minimum &Maximum Principal Stresses

By taking the difference between the minimum and maximum principal stresses for each linkage and comparing it to the fatigue limit of structural steel, it was determined whether the linkages would approach the fatigue limit of structural steel or not. These principal stresses are recorded at each node generated by the mesh in Abaqus along the length of each linkage. Based on the steady state principal stress values recorded, the linkages are subject to very low minimum and maximum principal stresses ranging from 0 – 22 MPa while rotating and overcoming the applied torque. As expected, the rocker (Figure 4-10) outputs the largest difference between the minimum and maximum principal stresses, approximately 22 MPa, since the moment was applied at its pinned end in the model.

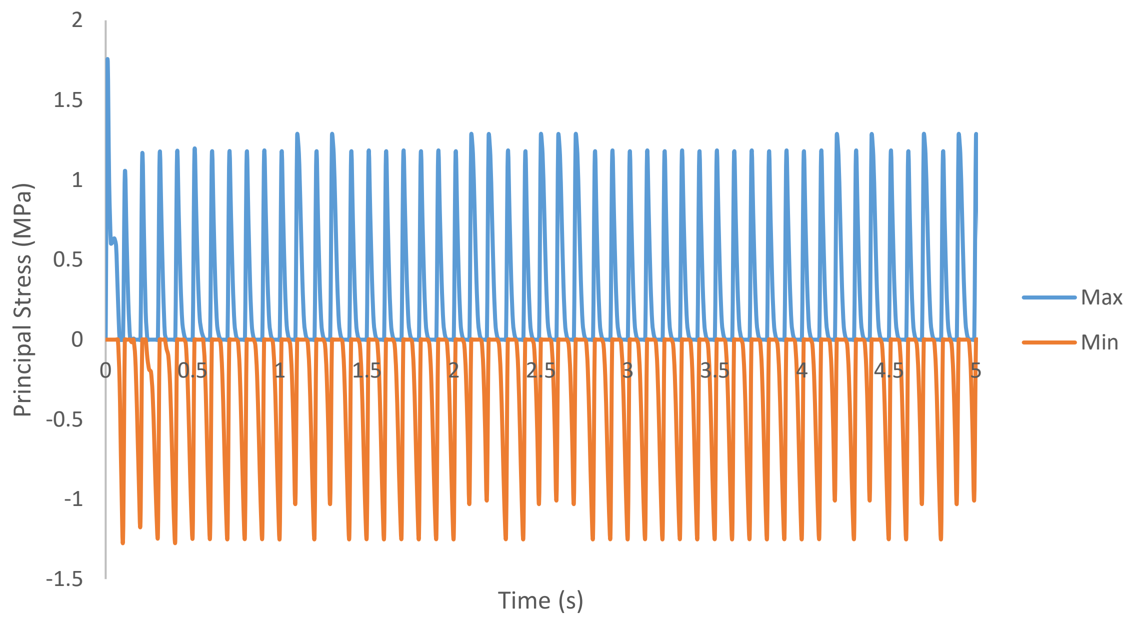

Figure 4-8: Minimum and maximum principal stresses on the crank

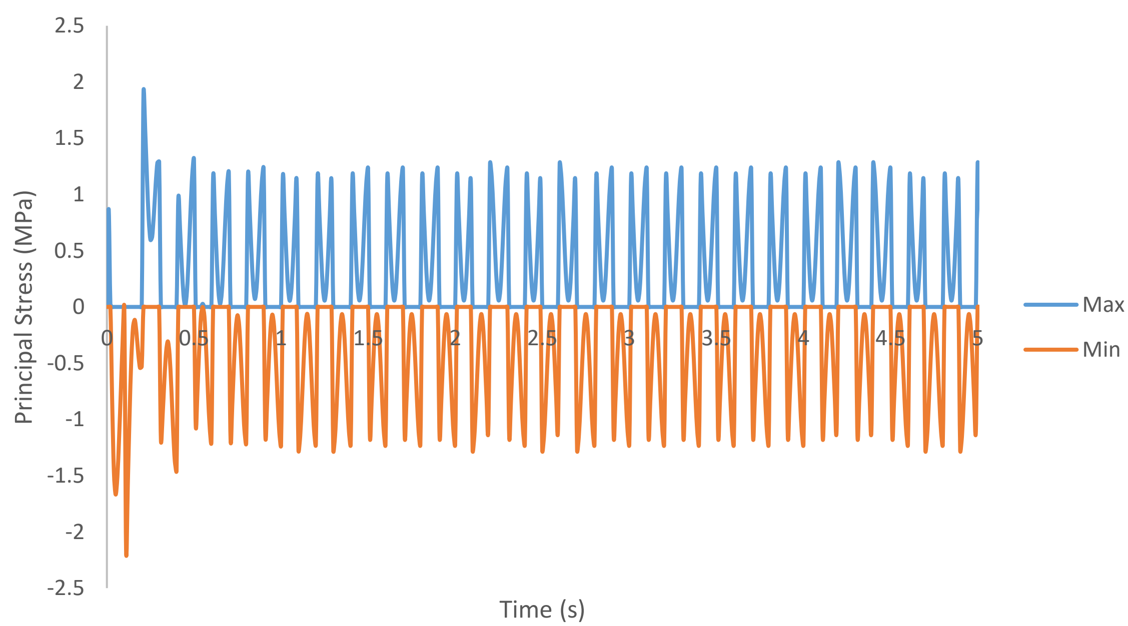

Figure 4-9: Minimum and maximum principal stresses on the coupler

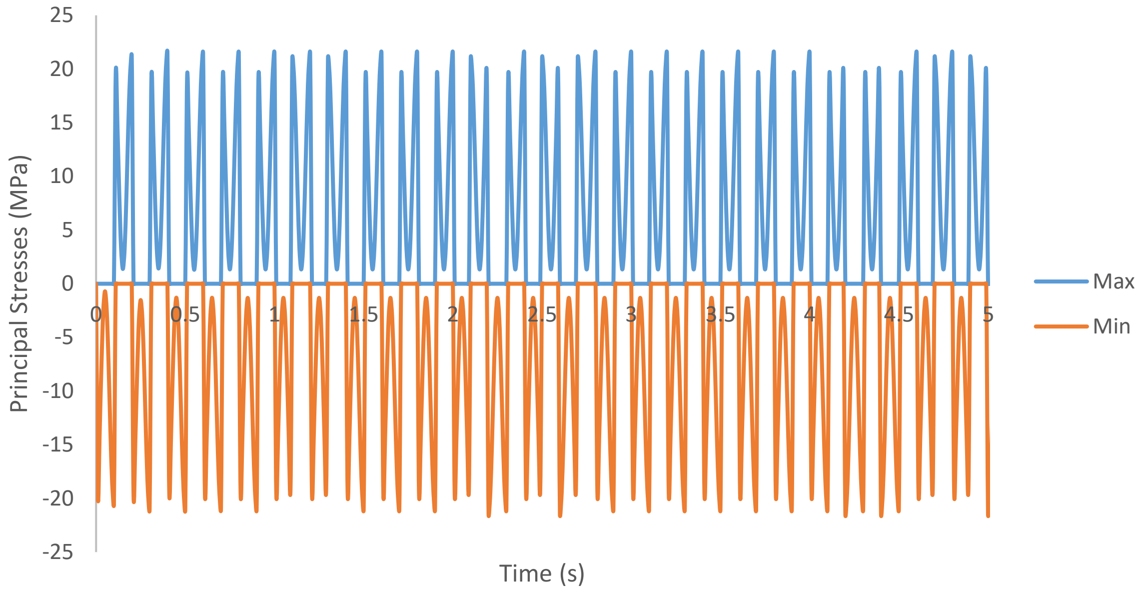

Figure 4-10: Minimum and maximum principal stresses on the rocker

4.3.3 Input Torque

The reaction moment depicted in Figure 4-11 is extracted at the pinned end of the crank since this is the location of the driving force of the system. This is done for both loading conditions at 5 Hz and 3 Hz rotation. Based on the graph, the driving torques are similar for both cases except the 5 Hz conditions has a larger initial torque. For the 5 Hz condition, the initial torque is approximately 1.79 N-m and decreases to a steady state value of approximately 0.9 N-m after 0.6 seconds. Like the previous graphs, we are mainly interested in the steady state reaction moment since this experiment runs for approximately 2.5 days on end. Considering the steady state portion of the graph, a maximum torque of 0.89 N-m, is required to drive the four-bar mechanism under these loading conditions.

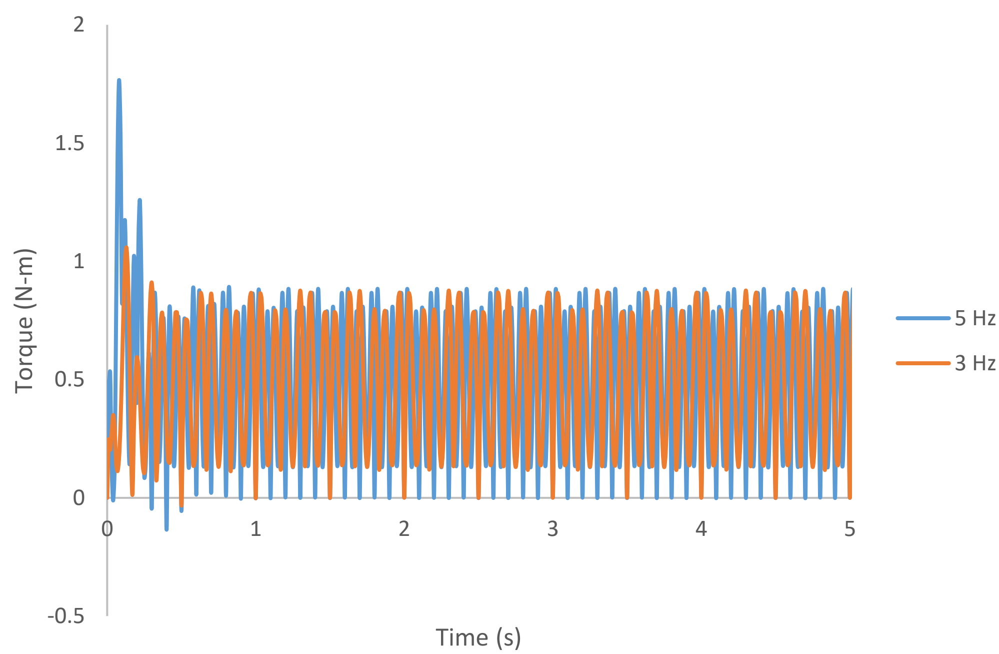

Figure 4-11: Reaction torque applied to the pinned end of the crank for both conditions

It should be noted that the additional pressure from the immersion fluid that the motor may have to overcome is not considered in this FE analysis. Equation 4-2 is used to calculate the size of the motor required.

$$[Eq\ 4-2] \quad \begin{aligned} P &= T\omega \\ &= 2 \cdot 0.89 \cdot 300 \cdot 0.105 \\ &= 0.056 \text{ kW} \end{aligned}$$

where:

P = Power (kW)

T = Torque (N-m)

ω = Angular velocity (rad/sec)

1 RPM = 0.105 rad/sec

Based on the above calculation, a 0.06 kW (0.08 hp) motor is sufficient to drive the system under the applied moment and additional forces from its environmental conditions.

4.4 Discussion

From the Dynamic Explicit Analysis, each linkage is subject to minimal principal stresses. Structural steel has a fatigue limit that is half of its ultimate tensile strength, approximately 225 MPa. The largest difference between the maximum and minimum principal stresses is exerted on the rocker (22 MPa). This value is approximately 10% of the fatigue limit of structural steel. Therefore, none of the linkages is expected to succumb to fatigue for at least 1 million cycles when a 5 mm x 25.4 mm cross section is used. Figures 4-9 and 4-10 show similar patterns to the applied moment (Figure 4-1). Such a trend is logical since the rocker is directly subject to the load and the coupler functions as an aid to translate motion between the coupler and the rocker. Consequently, the coupler is subject to the least amount of stress as confirmed in Figure 4-9.

Using double precision is essential to obtain an accurate model when running a dynamic explicit analysis because it assumes large deformations and rotations. In addition to the large deformations, the errors increase with each iteration under single precision, which explains why the analyses aborted initially from the deformed crank no matter what its thickness was set to. Figure 4-11 shows that the steady state driving torque oscillates between -0.001 N-m and 0.9 N-m. This is expected as the moment also oscillates. The position of the crank rocker mechanism and the magnitude of the torque applied at the pinned end of the rocker determine the driving torque at that instant. Even applying the wrong values would alter the shape of this graph significantly. Modelling the four-bar mechanism using 5 Hz rotation results in higher stresses and driving torques. Therefore, the system will function normally when operated at frequencies less than or equal to 5 Hz. In conclusion, Abaqus gives a good representation of the conditions needed to drive the four-bar mechanism.

Chapter 5 Dynamic Force Analysis of Four-Bar Mechanism

5.1 Introduction

A dynamic force analysis determines the resultant forces and driving torque of a kinematic system. This method uses Newton's equations of motion (Eq 5-1 to 5-3) to derive the aforementioned unknown quantities. After defining the coordinate system, equations 5-1 to 5-3 are written for each member of the kinematic system (Norton, 2008).

$$[Eq\ 5-1]\ \sum F_x = ma_x$$

$$[Eq\ 5-2]\ \sum F_y = ma_y$$

$$[Eq\ 5-3]\ \sum T = I_G\alpha$$

where:

F = Force (N)

m = mass (kg)

a = linear acceleration (m/s^2)

I = mass moment of inertia (kgm^2)

α = angular acceleration (rad/s^2)

Initially, a kinematic analysis of the system is performed to determine both the linear and angular velocities and accelerations of each linkage at a given instant. Knowing the geometry and material properties of the linkages allows for the calculation of the mass and mass moment of inertia for each linkage. After performing the kinematic analysis, a dynamic force analysis allows the calculation of the driving torque and reaction forces for this instant. These analyses can be reiterated either graphically or analytically for a complete cycle of motion of the mechanism since acceleration and velocity are time varying quantities. A complete cycle is necessary to determine the maximum driving torque needed to drive the system. Thus, the size of the constant speed motor needed for the loading conditions of this four-bar mechanism can be determined.

5.2 Kinematic Analysis of Even Return Four-Bar Mechanism

Figure 5-1 shows a kinematic diagram for the four-bar mechanism used in this experiment. The linkages are modelled as structural steel bars with rectangular cross sections in the Abaqus model. Therefore, the physical properties for each linkage are calculated from rectangular bars that are the lengths of from centre to centre of the linkages.

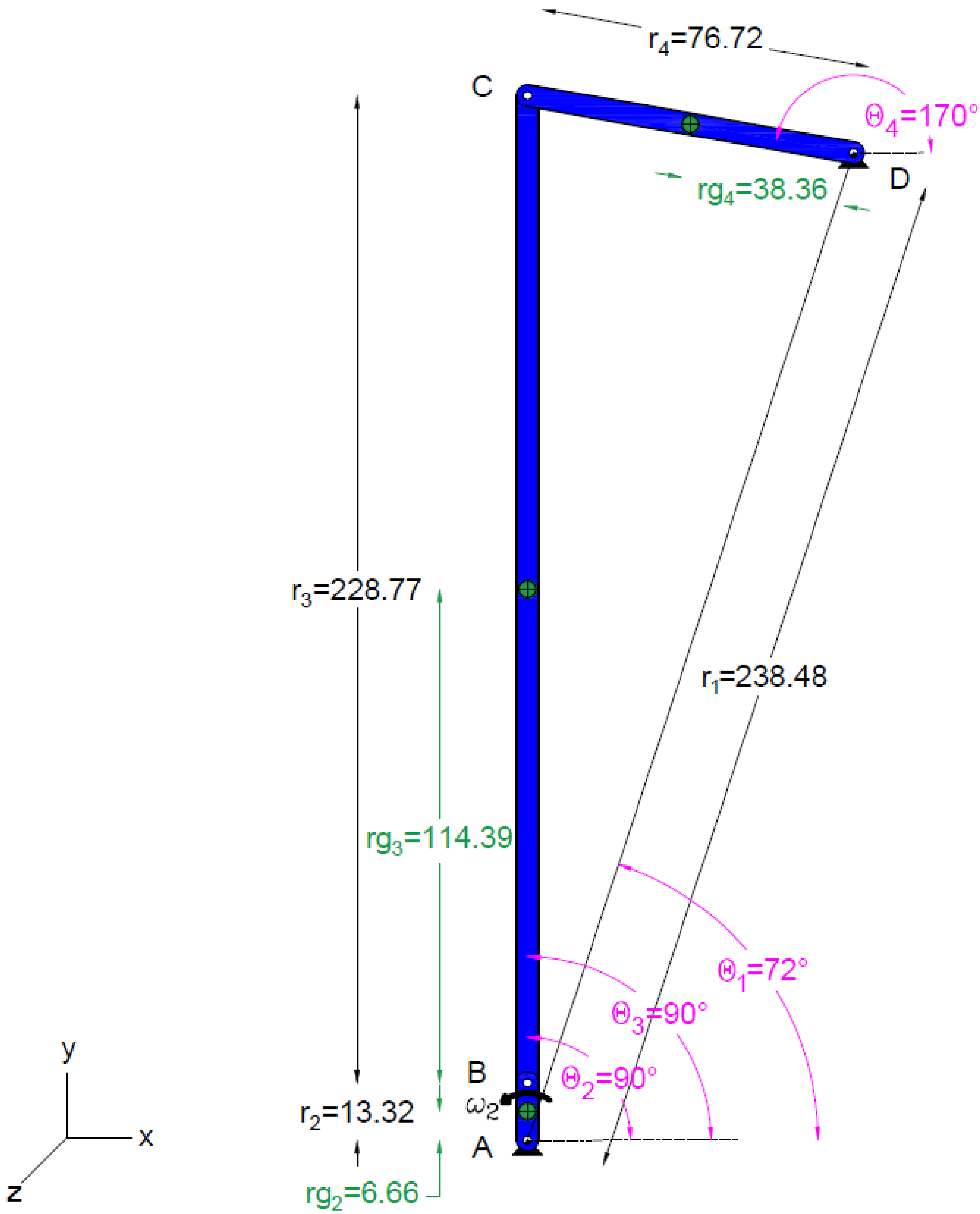

Figure 5-1: Kinematic diagram of four-bar mechanism in initial position

Rotation of each linkage occurs about the z-axis. Therefore, Equation 5-4 is used to calculate the mass moment of inertia.

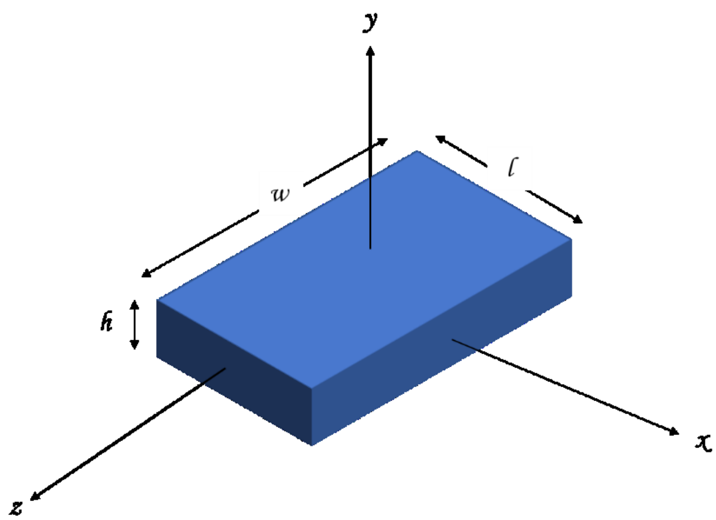

Figure 5-2: Mass moment of inertia of a rectangular bar

$$[Eq\ 5-4]\ I_z = \frac{1}{12}m(h^2 + l^2)$$

where:

I_z = mass moment of inertia about the z axis (kgm^2)

m = mass (kg)

h = height (m)

l = length (m)

Based on the experimental requirements, a constant speed motor rotating at 5 Hz is applied at the pinned end of the crank. Therefore, the angular velocity of link 2 is 10π rad/s and the acceleration is 0 rad/s^2. Using the analytical approach, the angular velocity and acceleration of the remaining linkages are calculated using the following equations to relate the linear velocity and acceleration of one point on a linkage to another. Pinned joints will have zero linear velocity and acceleration. The linear velocity of a point is the cross product of the angular velocity of the linkage and the position vector between the two points.

Relative velocity of Point B with respect to Point A on Link 2:

$$[Eq\ 5-5]\ \overrightarrow{v_B} = \overrightarrow{v_A} + \overrightarrow{v_{B/A}} = 0 + \overrightarrow{\omega_{AB}}\ X\ \overrightarrow{r_{B/A}}$$

Relative velocity of Point B with respect to Point C on Link 3:

$$[Eq\ 5-6]\ \overrightarrow{v_B} = \overrightarrow{v_C} + \overrightarrow{v_{B/C}} = \overrightarrow{v_C} + \overrightarrow{\omega_{BC}}\ X\ \overrightarrow{r_{B/C}}$$

Relative velocity of Point C with respect to Point D on Link 4:

$$[Eq\ 5-7]\ \overrightarrow{v_C} = \overrightarrow{v_D} + \overrightarrow{v_{C/D}} = 0 + \overrightarrow{\omega_{DC}}\ X\ \overrightarrow{r_{C/D}}$$

Equations 5-5 and 5-7 can be substituted into Equation 5-6. Then, this equation is split into two equations by separating the i and j components to solve for the two unknowns, ω_{BC} and ω_{CD}.

The angular acceleration of the remaining linkages can be found by relating the relative accelerations of points B and C in terms of the known accelerations at points A and D. Relative acceleration of one point with respect to another point can be split into its normal and tangential vector components. The normal component is perpendicular to the relative velocity vector and points towards the radius of curvature. On the contrary, the tangential component has the same direction as the relative velocity vector. Like relative velocity, the relative acceleration of a pinned joint is zero.

Relative acceleration of Point B with respect to Point A on Link 2:

$$[Eq\ 5-8]\ \overrightarrow{a_B} = \overrightarrow{a_A} + \overrightarrow{a_{B/A}} = \overrightarrow{a_B^n} + \overrightarrow{a_B^t}$$
$$= 0 + \left(\overrightarrow{a_{B/A}^n} + \overrightarrow{a_{B/A}^t}\right)$$

where:

$$\overrightarrow{a_{B/A}^n} = \overrightarrow{\omega_{AB}}\ X\ \overrightarrow{v_{A/B}} = \overrightarrow{\omega_{AB}}\ X\ \overrightarrow{\omega_{AB}}\ X\ \overrightarrow{r_{B/A}}$$

$$\overrightarrow{a_{B/A}^t} = \overrightarrow{\alpha_{AB}}\ X\ \overrightarrow{r_{B/A}}$$

Relative acceleration of Point B with respect to Point C on Link 3:

$$[Eq\ 5-9]\ \overrightarrow{a_B} = \overrightarrow{a_C} + \overrightarrow{a_{B/C}}$$
$$= \overrightarrow{a_C} + \left(\overrightarrow{a_{B/C}^n} + \overrightarrow{a_{B/C}^t}\right)$$

where:

$$\overrightarrow{a^n_{B/C}} = \overrightarrow{\omega_{BC}}\, X\, \overrightarrow{v_{B/C}} = \overrightarrow{\omega_{BC}}\, X\, \overrightarrow{\omega_{BC}}\, X\, \overrightarrow{r_{B/C}}$$

$$\overrightarrow{a^t_{B/C}} = \overrightarrow{\alpha_{BC}}\, X\, \overrightarrow{r_{B/C}}$$

Relative acceleration of Point C with respect to Point D on Link 4:

$$[Eq\ 5-10]\ \ \overrightarrow{a_C} = \overrightarrow{a_D} + \overrightarrow{a_{C/D}}$$

$$= 0 + \left(\overrightarrow{a^n_{C/D}} + \overrightarrow{a^t_{C/D}}\right)$$

where:

$$\overrightarrow{a^n_{C/D}} = \overrightarrow{\omega_{CD}}\, X\, \overrightarrow{v_{C/D}} = \overrightarrow{\omega_{CD}}\, X\, \overrightarrow{\omega_{CD}}\, X\, \overrightarrow{r_{C/D}}$$

$$\overrightarrow{a^t_{C/D}} = \overrightarrow{\alpha_{CD}}\, X\, \overrightarrow{r_{C/D}}$$

Similarly, these three equations are enough to solve for the two unknowns, α_{BC} and α_{CD}. This method is valid for the calculation of relative acceleration at any point along the linkage. Therefore, the acceleration at the centre of gravity of each linkage can also be calculated with this method. Table 5-1 summarizes the kinematic properties of each linkage for the instant in Figure 5-1 by hand calculation. To validate these results, this four-bar mechanism is modelled in this initial position and analyzed using System Advisor Model, more commonly termed SAM 7.0. As per the requirements of the experiment, a constant speed motor is assumed to act at the pinned joint of link 2.

Table 5-1: Kinematic analysis of four-bar mechanism in the initial position

Linkage	**Length**	**Mass**	**Mass Moment of Inertia, I_g**	**Angular velocity, ω**	**Angular acceleration, α**
i	**(m)**	**(kg)**	**(kgm^2)**	**(rad/s)**	**(rad/s^2)**
1	0.240	N/A	N/A	N/A	N/A
2	0.013	1.33×10^{-2}	9.05×10^{-7}	31.42	0
3	0.228	2.27×10^{-1}	9.98×10^{-4}	-1.83	10.78
4	0.077	7.65×10^{-2}	4.16×10^{-5}	0	184.16

The angular position, velocity and acceleration of links 3 and 4 vary as link 2 makes a complete revolution. Thus, these calculations need to be repeated for varying positions of each linkage to obtain the full pattern for a complete revolution of the crank. To do so efficiently, this linkage is modelled in its initial position and analyzed using the program System Advisor Model, SAM 7.0 (Figure 5-3). Using the built-in four-bar mechanism template, the coordinates of each node are entered into the system. The angular velocity, 1800 deg/s, and the number of increments for computation are then applied at node 1. Then, the mass, position of centre of gravity relative to the left node and the mass moment of inertia for each beam are defined. The red dots on each linkage in Figure 5-3 represent the relative positions of the centre of gravity.

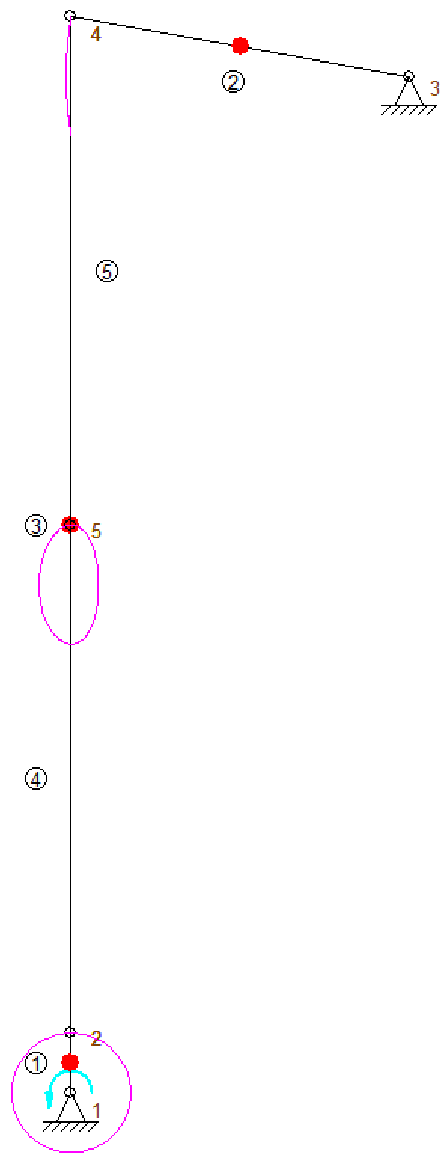

Figure 5-3: Four-bar linkage modelled in SAM 7.0

After defining the model, the analysis is run. Figures 5-4 to 5-6 are plots of the kinematic data required to perform the dynamic force analysis. As expected, the position of link 2 oscillates between 170° and 190° since the rocker is constrained to give an output angle of 20°. Link 3 is initially oriented at 90° and oscillates between 87° and 93°. These results correspond to the expected positions. Both the angular velocities and angular accelerations of links 2 and 3 correspond with the values shown in Table 5-1.

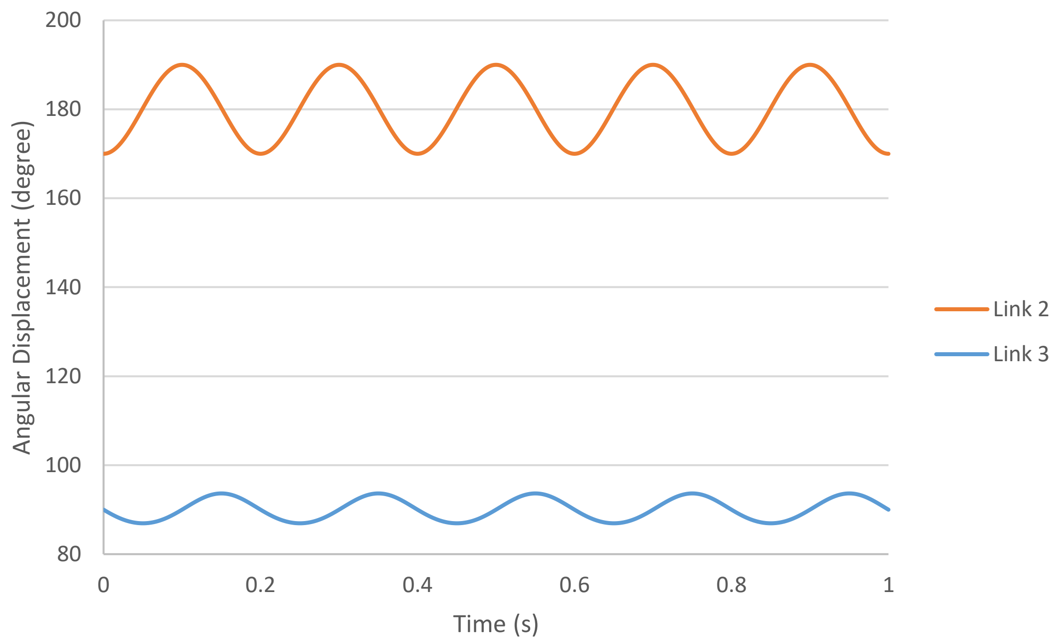

Figure 5-4: Angular position of links 2 and 3 with crank rotation

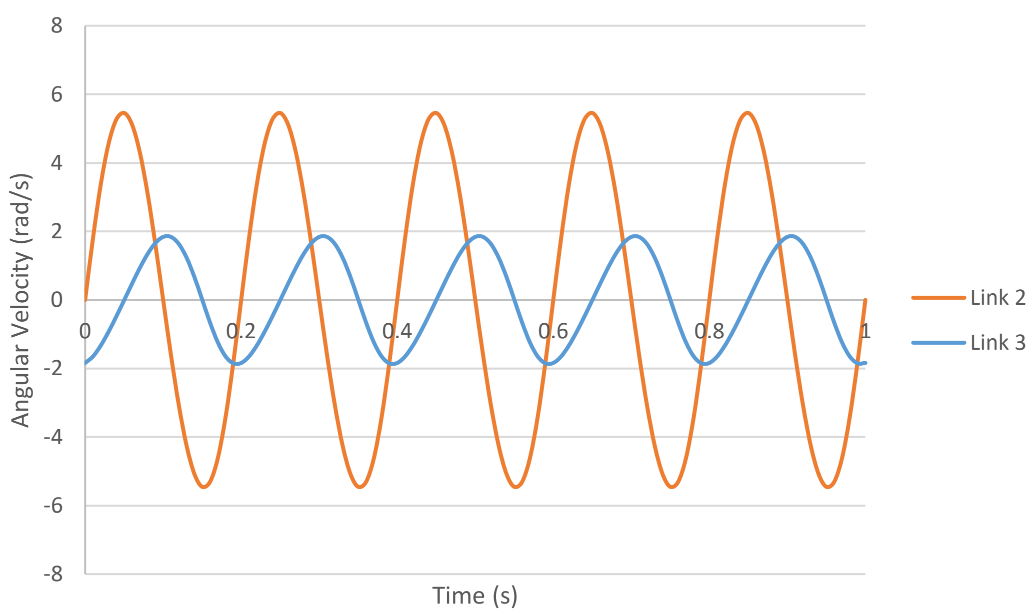

Figure 5-5: Angular velocity of links 2 and 3 with crank rotation

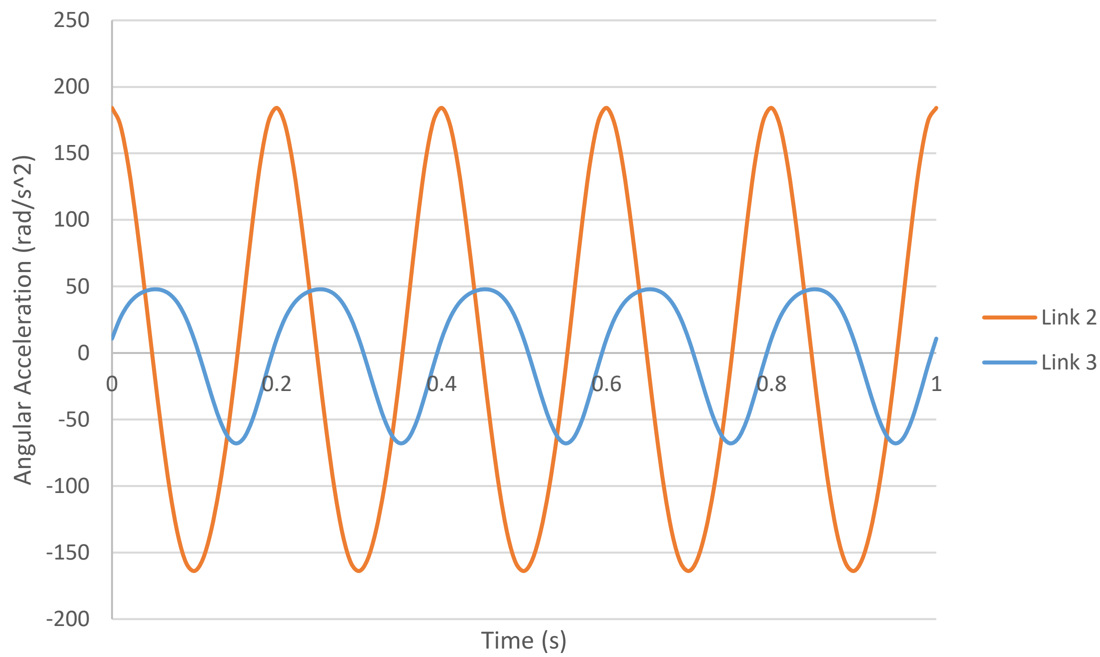

Figure 5-6: Angular acceleration of links 2 and 3 with crank rotation

5.3 Dynamic Force Analysis of Four-Bar Mechanism

Now that the change in acceleration and velocity of each linkage with time is known, Newtonian equations can be written for each linkage to find the change of the driving torque of the system with time. Keeping with consistency, the instant depicted in Figure 5-1 is analyzed as shown in Figure 5-7.

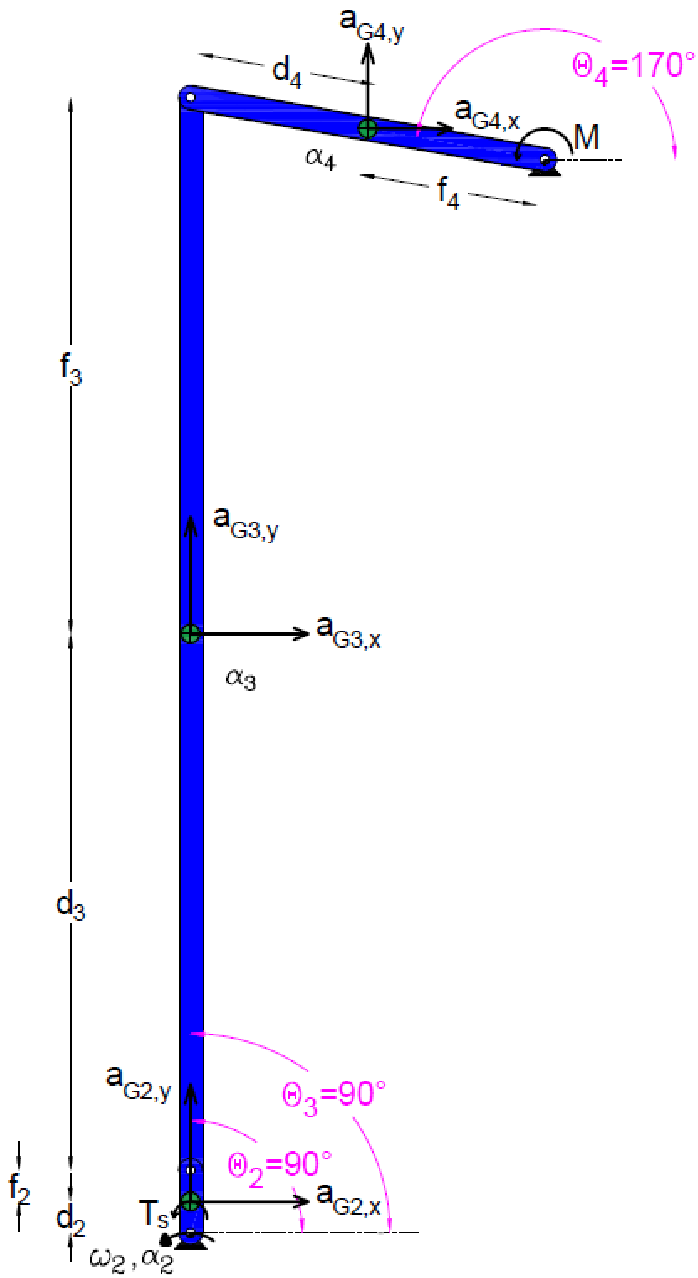

Figure 5-7: Diagram for dynamic force analysis at initial instant

A free body diagram (FBD) is drawn for links 2, 3 and 4 (Figures 5-8 to 5-10). The x and y components of the joint forces, any externally applied forces, location of centre of gravity, angular displacement from the x-axis and distances between the end points and centre of gravity are denoted on each FBD. Equations 5-11 to 5-19 are the Newtonian equations written for each linkage.

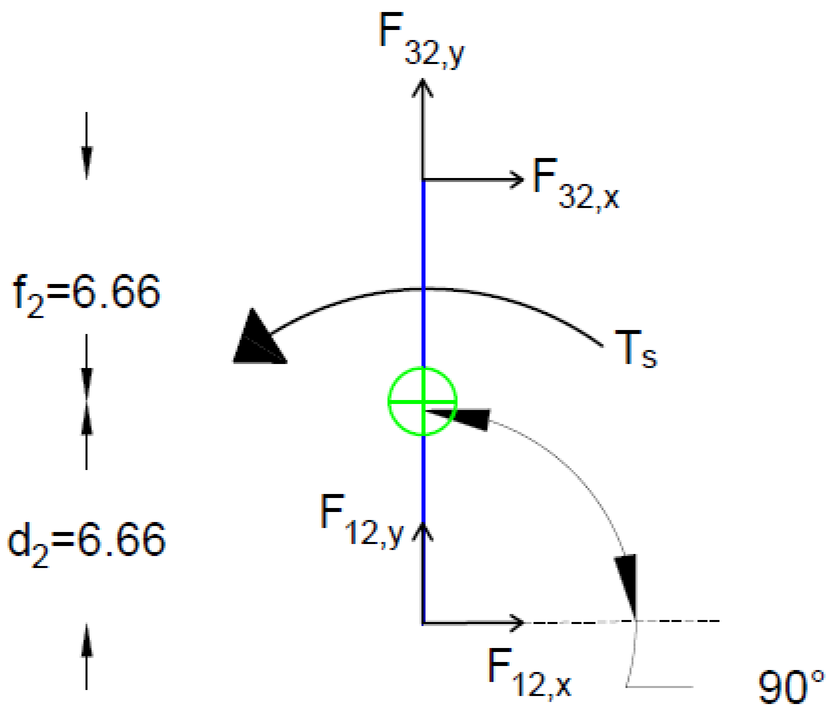

Figure 5-8: Free body diagram for Link 2

Link 2:

$$[Eq\ 5-11]\ \ F_{12,x} + F_{32,x} = m_2 a_{G2,x}$$

$$[Eq\ 5-12]\ \ F_{12,y} + F_{32,y} = m_2 a_{G2,y}$$

$$[Eq\ 5-13]\ \ F_{12,x} d_2 sin\theta_2 - F_{12,y} d_2 cos\theta_2 - F_{32,x} f_2 sin\theta_2 + F_{32,y} f_2 cos\theta_2 + T_s = m_2 I_{G2}$$

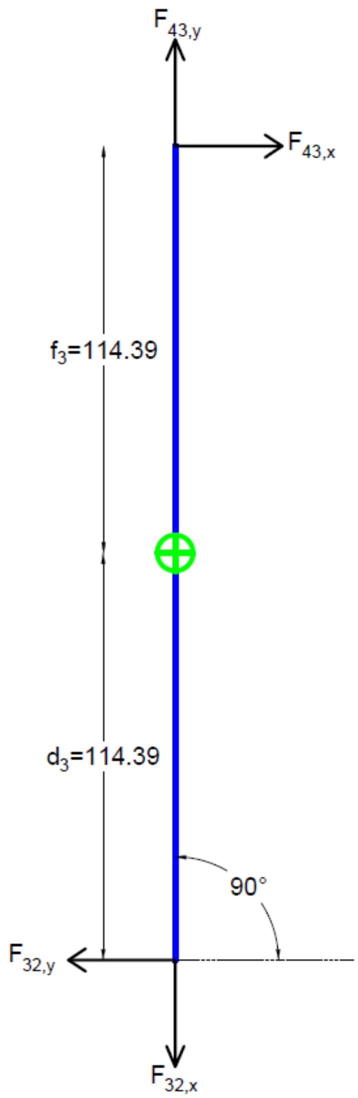

Figure 5-9: Free body diagram for Link 3

Link 3:

$$[Eq\ 5-14]\quad -F_{32,x}+F_{43,x}=m_3a_{G3,x}$$

$$[Eq\ 5-15]\quad -F_{32,y}+F_{43,y}=m_3a_{G3,y}$$

$$[Eq\ 5-16]\quad F_{43,x}f_3sin\theta_3+F_{43,y}f_3cos\theta_3-F_{32,x}d_3sin\theta_3+F_{32,y}d_3cos\theta_3=m_3I_{G3}$$

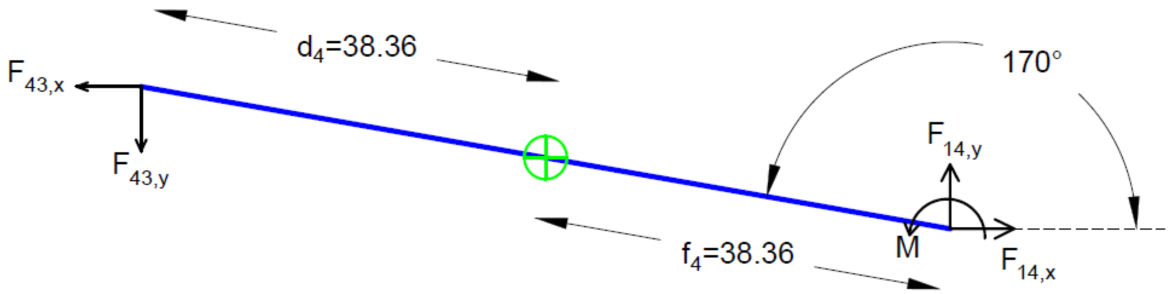

Figure 5-10: Free body diagram for Link 4

Link 4:

$$[Eq\ 5-17]\quad -F_{43,x}+F_{14,x}=m_4 a_{G4,x}$$

$$[Eq\ 5-18]\quad -F_{43,y}+F_{14,y}=m_4 a_{G4,y}$$

$$[Eq\ 5-19]\quad F_{43,x}d_4 sin\theta_4 - F_{43,y}d_4 cos\theta_4 - F_{14,x}f_4 sin\theta_4 - F_{14,y}f_4 cos\theta_4 + M = m_4 I_{G4}$$

As discussed in the previous chapter, the external torque, M, varies with time. To save computation time, this computation is not done by hand. Instead, the mechanism is modelled both in SAM 7.0 and an online program entitled Ch Mechanism Toolkit 3.0. This is necessary to validate the driving torque for this system using SAM 7.0. For the online version of Ch Mechanism Toolkit 3.0, Figure 5-11 depicts the graphic used to define the required parameters.

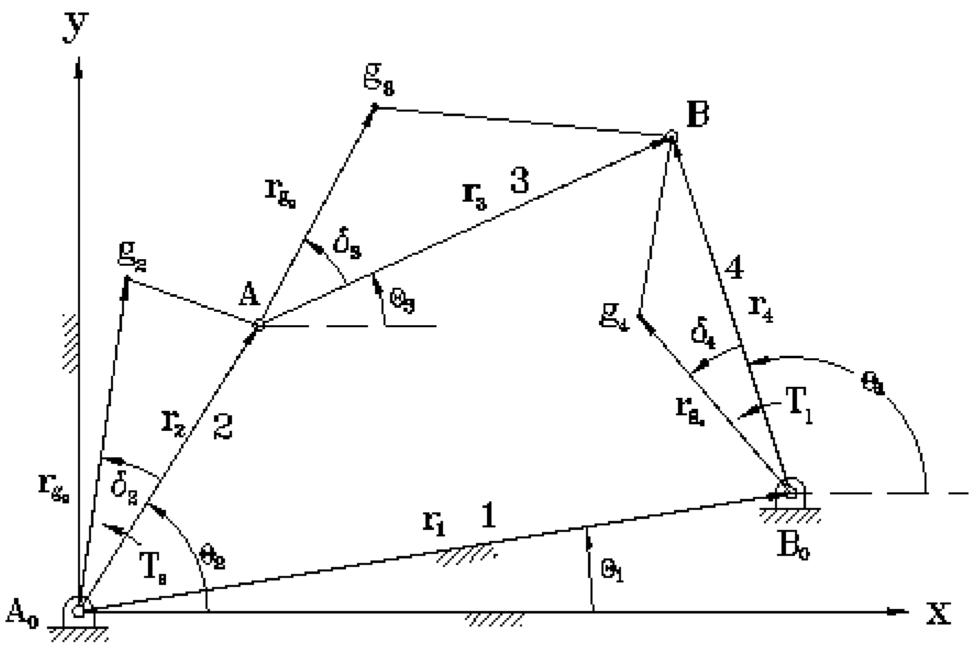

Figure 5-11: Parameters required for online program. Retrieved from softintegration.com

The following information is required:

1. Length of link 1 (r_1), link 2 (r_2), link 3 (r_3) and link 4 (r_4).
2. Mass of link 2 (m_2), link 3 (m_3) and link 4 (m_4).
3. Mass moment of inertia of link 2 (i_{g2}), link 3 (i_{g3}) and link 4 (i_{g4}).
4. Magnitude of position vector for link 2 (r_{g2}), link 3 (r_{g3}) and link 4 (r_{g4}).
5. Angular displacement of link 1, Θ_1.
6. Angular displacement of link 2, Θ_2.
7. Angular displacement of centre of gravity from link position for link 2 (δ_2), link 3 (δ_3) and link 4 (δ_4)
8. External torque on joint B_0.
9. Angular velocity of either link 2 (ω_2), link 3 (ω_3) or link 4 (ω_4).
10. Angular acceleration of either link 2 (α_2), link 3 (α_3) or link 4 (α_4).

The driving torque is calculated by keeping all the parameters constant except the angular displacement link and magnitude of the external moment at the pinned end of link 4, T_1. By varying the angular displacement of the crank at increments of 10° and using its corresponding applied moment from Figure 4-3, the driving torque for a complete revolution of the crank from its initial position is recorded. Since this program only requires the angle of one linkage to perform analyses, there are two possible answers for the driving torque obtained. These are labelled T1 and T2 on Figure 5-12.

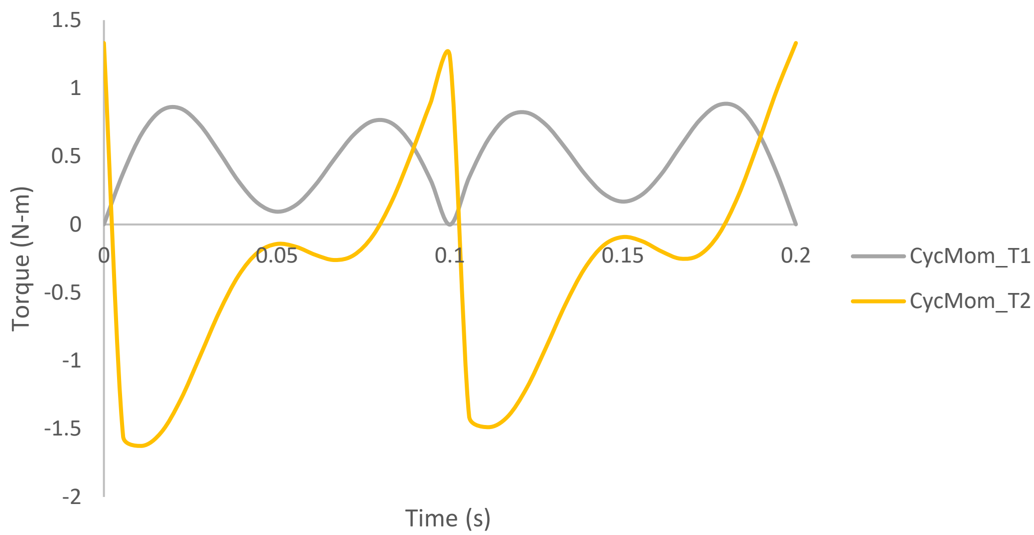

Figure 5-12: Driving torque obtained from Ch Mechanism Toolkit 3.0

It is not possible to paste a table of values for moment in SAM 7.0 as was done in Abaqus. To specify the varying moment with time for this case, the user should enter the initial moment and the amount it increases by every 0.01 seconds with one iteration. The number of increments used to describe the load should correspond to the number of increments used for the angular velocity of the crank. Otherwise, the analysis will not run. Figure 5-13 depicts the results obtained from this analysis. This corresponds to driving torque, T_1, of the two options obtained using the online program. This torque oscillates in a pattern similar to that of the graph of the applied moment. The magnitude of the torque ranges between a minimum of -0.001 N-m and a maximum of approximately 0.9 N-m.

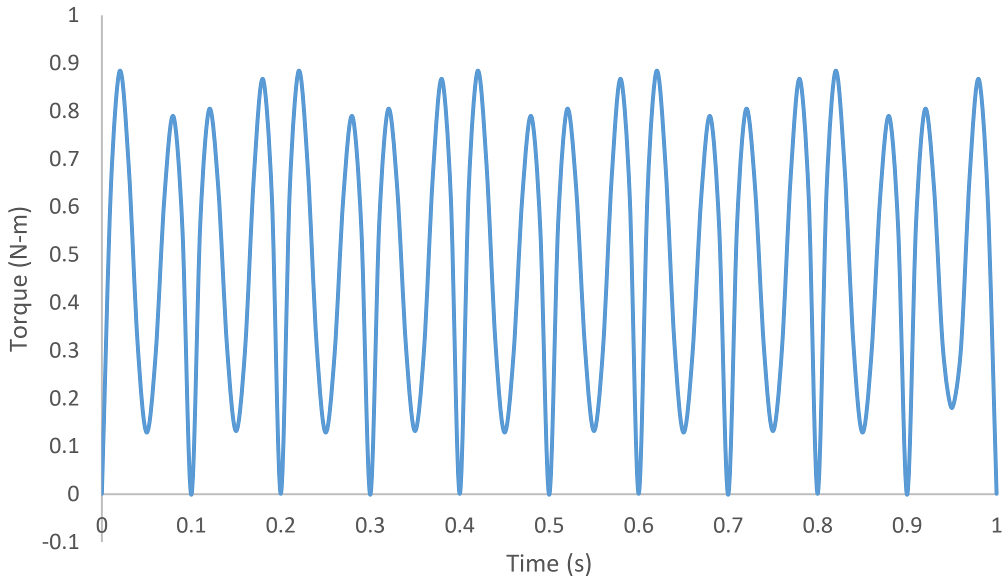

Figure 5-13: Driving torque obtained from SAM 7.0

5.4 Discussion/Comparison with Finite Element Analysis

Both SAM 7.0 and the online program produced a graph similar to that of the steady state portion of the driving torque graph obtained from Abaqus. However, Abaqus predicts a higher magnitude of torque in the initial stage (Figure 5-14). According to the Abaqus User Manual, a dynamic explicit analysis in Abaqus uses an explicit integration rule along with the lumped mass matrix of the elements. For this method, the equations of motion for the body are integrated using the explicit central difference integration rule. In addition, the initial values for velocity and acceleration are assumed to be 0 unless predefined by the user. This was not the case for all the linkages based on the values shown in Table 5-1 and the initial velocities were not defined for the dynamic explicit analysis. Therefore, a larger torque was required initially to accelerate the system from 0 velocity to the constant velocity required to keep the four-bar mechanism in motion.

Based on these results, performing a dynamic force analysis proved that Abaqus is sufficient to predict the torque required to drive the system. Therefore, it was not necessary to perform these calculations for the 3 Hz loading condition using a dynamic force analysis.

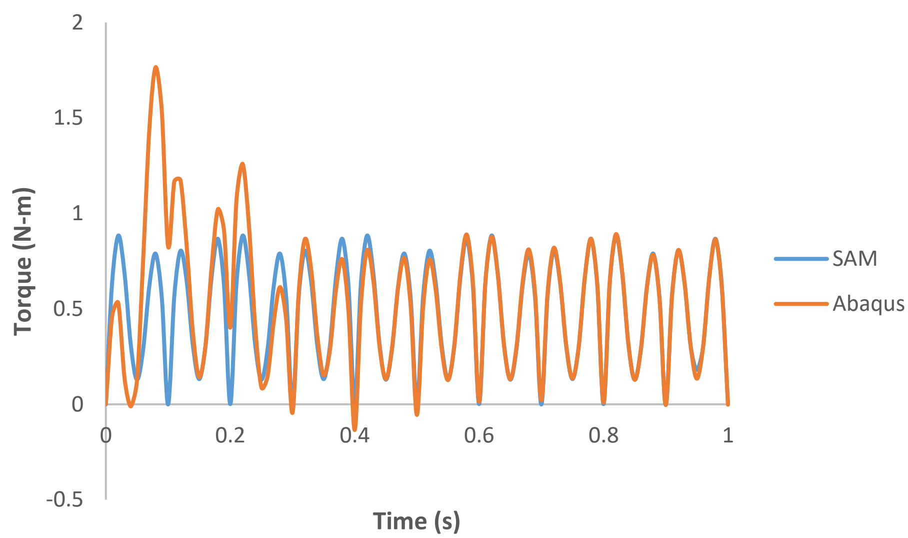

Figure 5-14: Comparison of driving torque obtained from Abaqus with SAM 7.0

Chapter 6 Experimental Procedure

6.1 Procedure

6.1.1 Preparation of Immersion Fluid

Based on ISO 14242-2 and wear testing done on TARs by other researchers, 20 g/l bovine serum diluted with deionized water was selected as the immersion fluid. To minimize microbial growth at this concentration, 0.2% sodium azide was added to the solution (Scholes et al, 2007). The protein concentration of the bovine serum supplied (Hyclone SH30073) contains 7 g/dl (70 g/l) of protein. Equation 6-1 was used to find the volume of solution needed to get the required 20 g/l concentration of bovine serum.

$$[Eq\ 6-1]\ \ C_1V_1 = C_2V_2$$

$$70\frac{g}{l} * (1\ L) = 20\frac{g}{l} *\ V_2$$

$$V_2 = 3.5\ L$$

where:

$C_1 = Given\ concentration\ \left(\frac{g}{l}\right)$

$C_2 = Desired\ concentration\ (\frac{g}{l})$

$V_1 = Given\ volume\ (L)$

$V_2 = Required\ volume\ (L)$

Therefore, 2.5 L of deionized water should be added to 1 L of 70 g/l bovine serum to obtain a 20 g/l protein concentration. Equation 6-2 was used to calculate the mass of sodium azide (NaN_3) that should be added to the 3.5 L solution to obtain 0.2% solution.

$$[Eq\ 6-2]\ \frac{mass}{volume}\% = \frac{mass\ of\ solute}{volume\ of\ solution}\ x\ 100\%$$

$$0.2\% = \frac{x}{3.5\ L}\ x\ 100\%$$

$$x = 7\ g$$

where:

$x = mass\ of\ solute\ required\ (g)$

Based on this calculation, 7 g of NaN_3 should be added to the 3.5 L solution of bovine serum and deionized water to obtain the desired percent solution. The test chamber requires 1 L of solution to fully submerge the implants in the immersion fluid during testing for 500,000 cycles. With this information, the solution can be prepared and divided into 500 ml aliquots for storage and testing. Personal Protective Equipment (PPE) and a chemical fume hood are required to prepare the solution. The following procedure was used to prepare the immersion fluid:

1. Add 2.5 L of deionized water to a 5 L beaker and place it on a stirrer.
2. Weigh 7 g of Sodium Azide and add it to the deionized water.
3. Mix the solution for about 30 minutes.
4. Add 1 L of bovine serum to the solution
5. Allow the solution to mix further for 20 minutes
6. Measure the pH of the solution. It should be about 8.1.
7. Filter the solution into 500 ml bottles through 2 micron (Grade 602-H) filter paper
8. Label the bottles with the contents of the solution, the volume and the date
9. Store the solution at -20°C until required

6.1.2 Initial Measurements & Cleaning Procedure

ISO 14242-2 requires the samples to be pre-soaked, cleaned, dried and weighed until a steady sorption rate has been obtained prior to initiating wear testing. This procedure was modified to suit the purpose of finding out the problems associated with performing wear testing using this test setup. No control specimen was used in this test run. This was due to the fact that the machine only has one test station and unforeseen delays due to manufacturing and machine failure cut down the allotted time for testing. Figure 6-1 shows the implants prior to testing.

Figure 6-1: Surface of implants prior to testing

The following is the regimen taken for cleaning, drying and weighing the implants after soaking:

1. Soak the implants in the immersion fluid for 42 hours.
2. Remove the specimens from the fluid and clean in an ultrasonic cleaner by taking the following steps:
    a. Vibrate in deionized water for 10 minutes
    b. Rinse in deionized water
    c. Vibrate in a mix of 10% detergent (Decon Contrad 70) and deionized water for 10 minutes
    d. Rinse in deionized water
    e. Vibrate in deionized water for 10 minutes
    f. Rinse in deionized water
    g. Vibrate in deionized water for 3 minutes
    h. Rinse in deionized water
3. Dry the specimens with a jet of filtered Nitrogen gas.
4. Soak the test specimen and control specimen in propan-2-ol for 5 minutes.
5. Dry the test specimen and soak control with a jet of filtered Nitrogen gas.
6. Dry the specimens further in a vacuum desiccator for 30 minutes.
7. Weigh the specimens on the balance twice in rotation within 90 minutes of removal from the vacuum. If the two readings are not identical within 100 micrograms, continue taking

readings in rotation until at least two readings per specimen are within 100 micrograms of each other. Store the specimen in a sealed, dust free container between weighing.

8. Repeat steps 2 to 6 at intervals until the incremental mass change of the specimen over 24 hours is less than 10% of the cumulative mass change.

6.2 Wear Testing

After weighing, the implants were taken for wear testing in the subtalar joint simulator. First, the talus and calcaneus implants were attached to their respective jigs and the test chamber was filled with the immersion fluid. Then, the mating surfaces of the implants were placed in contact with each other using a static load of approximately -150 N. The VFD was turned on so that rotary displacement (± 10°) at 3 Hz was applied to the calcaneus jig while the static load maintained contact between the two implants. Once the machine gave a satisfactory response to the rotary displacement, that is, if the static load applied did not fluctuate significantly and the machine maintained contact between the talus and calcaneus implants, wear testing could commence. The fatigue testing machine was programmed to apply a compressive sinusoidal load with peak values at -50 N and -800 N at 6 Hz for 1 million cycles. Load data was recorded to verify that testing was successfully carried out. In the event testing was interrupted, the implants were removed from the test fluid, rinsed in deionized water and stored in a sealed container until testing resumed.

6.2.1 Operation of the wear testing simulator

1. Turn on the fatigue testing machine.
2. Attach the implants to their respective jigs.
3. Add 1 L of the immersion fluid to the test chamber.
4. Loosen the bolts on the cross head and activate the lever to lower it so that there is approximately a 1-2 mm gap between the surfaces of the implants
5. Deactivate the lever and tighten the bolts on the crosshead.
6. Cover the test chamber. Figure 6-2 depicts the completed setup.
7. Launch Wintest 7 and open the project file for this test.
8. If the reading from the load meter does not fluctuate about 0 N, right-click on the load meter window, select “Tare” and then “Auto”.
9. Set “DirComA” as the command channel before turning on the mover power.

10. Press the arrow down button since the load cell is placed on the cross head and incrementally decrease the voltage until the talus and calcaneus jigs are in contact with each other, approximately -20 N.
11. Tune the machine for the loading that you wish to apply to the implants, in this case use a sine wave ranging from -50 N to -800 N at 6 Hz. Do not apply rotation to the calcaneus jig while tuning the machine.
12. After tuning is complete, change the compressive force on the implants to about -150 N by increasing the voltage. Before doing so, ensure that the control channel is set to DirCmdA.
13. Turn on the VFD and apply 6 Hz rotation to the calcaneus jig. As discussed in Chapter 3, this is equivalent to 3 Hz output from the motor shaft.
14. Keep the same waveform parameters from tuning and change the number of cycles of loading applied to the desired value, 1 million cycles, in this case. Reset the initial cycle count to zero.
15. Select "Standard Timed Data" and create a file for saving the test data. Ensure that all the parameters that you want recorded are selected and the number of scans are more than the duration of the test. Hit start.
16. Click "Run" and allow the test to run. Load and rotation should be applied simultaneously to the implant.
17. If an error occurs and the machine stops applying load, close the program and repeat steps 2 to 14. You may need to troubleshoot the machine or let it rest if the problem persists.
18. At the end of the test, turn off the mover power and VFD.
19. Loosen the bolts on the cross head and use the lever to raise it.
20. Remove the implants from the jigs and rinse them with deionized water before storing them in a closed, dust free container.
21. Use the siphon pump to remove the bulk of the immersion fluid from the test chamber. Place the fluid in the designated waste container. Refill the chamber several times with soapy water and then fresh water to clean the pump and chamber.
22. Wash the removable parts with soap and water and leave them to dry. Spray the test chamber with 70% Ethanol and wipe it down with clean napkins.
23. Take the implants to be cleaned, dried and weighed.

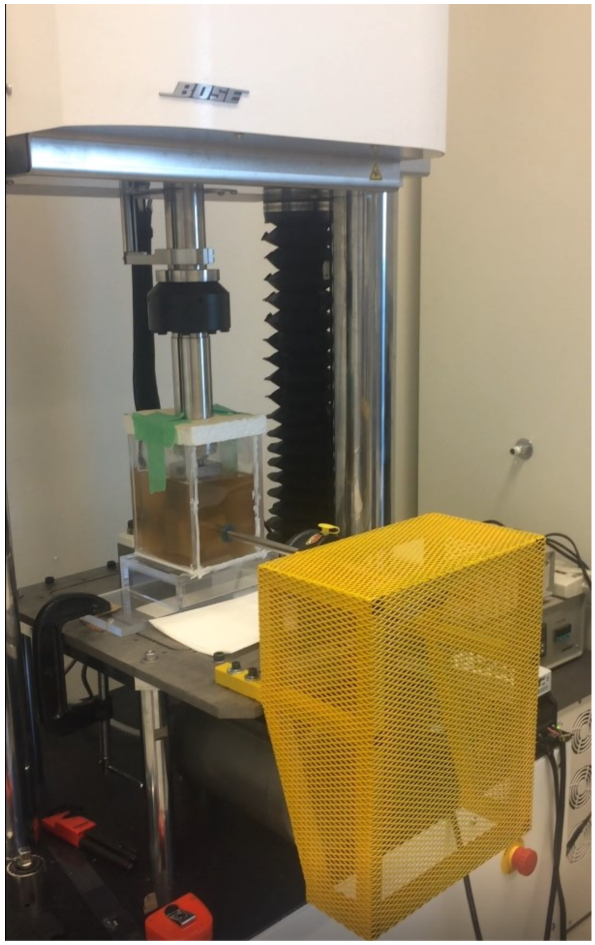

Figure 6-2: Complete setup for wear testing

6.3 Post Test

After testing, the samples are cleaned, dried and weighed following the procedure outlined in Section 6.1.2. In addition to the mass lost, the physical changes to the mating surfaces of the implants and the change in surface roughness of the implants were observed and measured.

6.3.1 Mass Measurement

After removing the implants from the vacuum desiccator, the implants were weighed in rotation every 10 minutes until the masses stabilized, i.e., the readings were within 0.1 mg of each other. No measurements were taken beyond 90 minutes after removal from the vacuum desiccator.

6.3.2 Surface Characterization

6.3.2.1 Microscope and Profilometer

A Zygo Optical Profilometer is selected to measure the initial roughness of the implants after 250,000 cycles, 500,000 cycles, 1,000,000 cycles and every 1 million cycles to the end of testing. The measurements after wear testing are taken after the cleaning, drying and weighing regimen. Since the implants are considerably large, 10x magnification and 1.0 zoom was used for the surface roughness measurements. It should be noted that this device is not built for specimens with steep slopes. In addition, it is impossible to take measurements at the exact spot without marking the implants. Therefore, the average of several measurements about the centre of both implants are calculated. Figures 6-3 and 6-4 are screenshots of the output displayed by the profilometer.

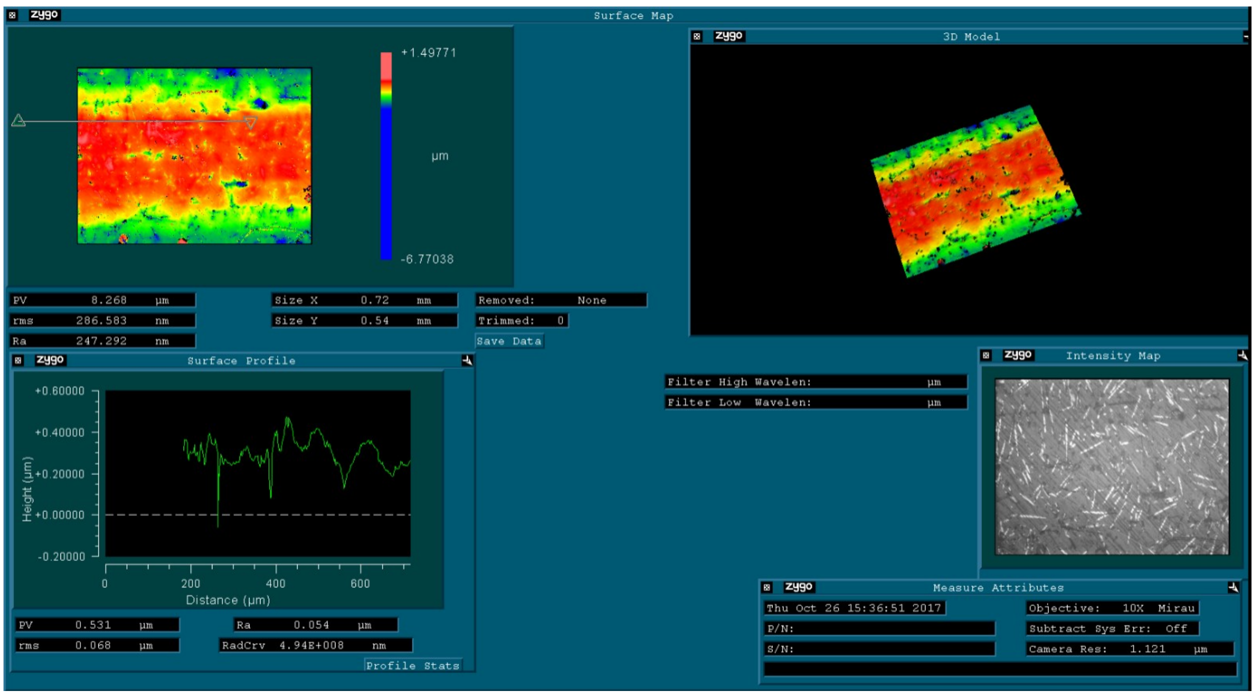

Figure 6-3: Sample of profilometer output for Calcaneus Implant prior to testing

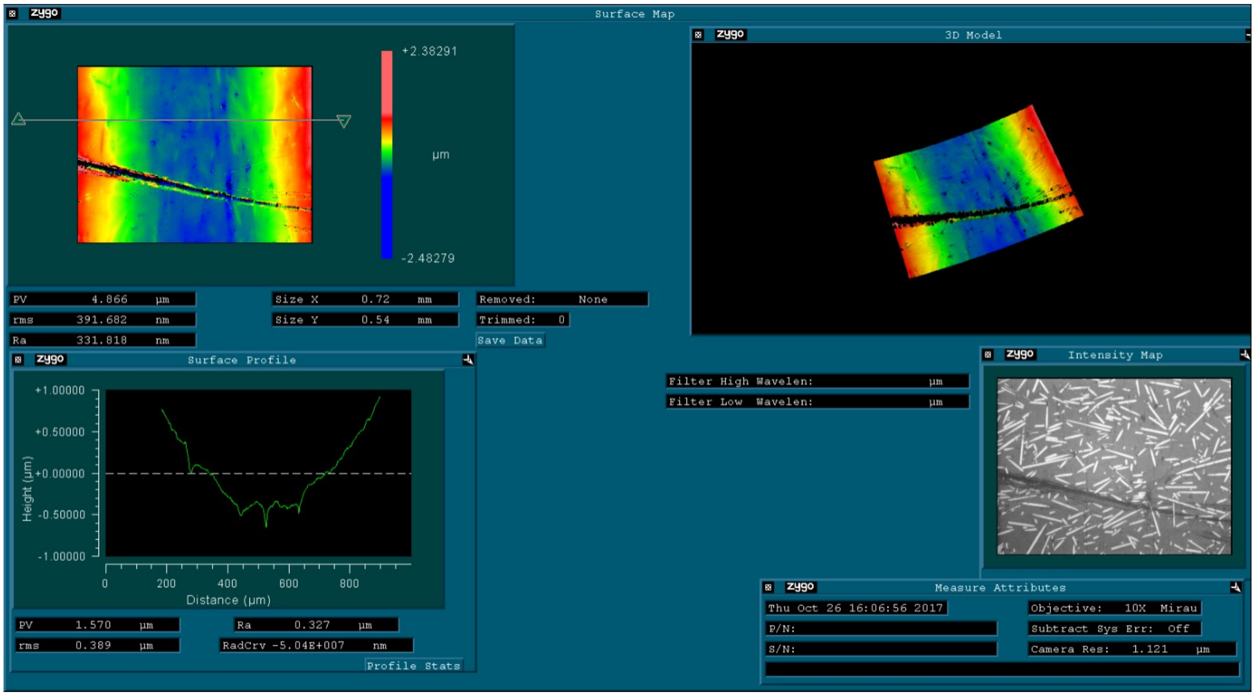

Figure 6-4: Sample of profilometer output for Talus Implant prior to testing

As seen from the above screenshots, this profilometer provides the roughness (Ra), root mean square (rms), maximum peak-to-valley height (PV), a surface profile, 2D model, 3D model and intensity map. The equations used to calculate these values were retrieved from the Zygo Surface Texture Parameters manual (Zygo, 2013). Ra is defined as the arithmetic mean roughness of the absolute value of the profile along the length of the sample being evaluated (Figure 6-5). Equation 6-3 is used to calculate Ra.

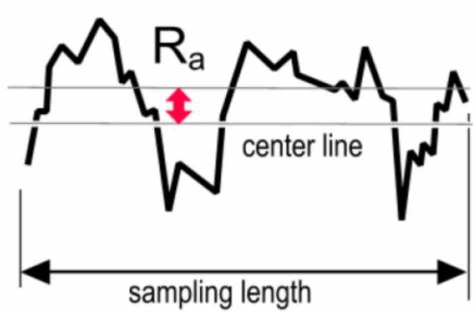

Figure 6-5: Roughness (Ra) measurement along a sampling length (Zygo, 2013)

$$[Eq\ 6-3]\ \ R_a = \frac{1}{L}\int_0^L |z(x)|\, dx$$

where:

$L = Sampling\ length$

The root-mean-square roughness, rms, is calculated using Equation 6-4 and corresponds to the Ra value.

$$[Eq\ 6-4]\ \ rms = \sqrt{\frac{1}{L}\int_0^L |z^2(x)|\, dx}$$

where:

$L = Sampling\ length$

PV (Figure 6-6) is the absolute value of the sum of the highest and lowest peaks along the length of the sample being evaluated. This roughness parameter is defined by Equation 6-5.

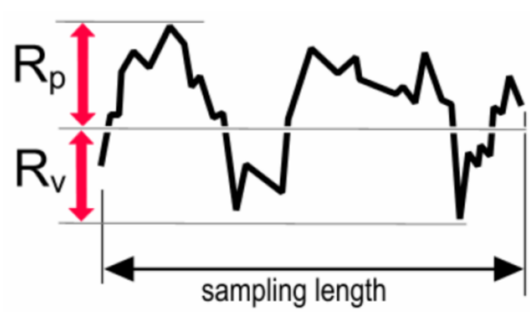

Figure 6-6: PV measurements along a sampling length. (Zygo, 2013)

$$[Eq\ 6-5]\ PV = R_p + R_v$$

where:

$R_p = Highest\ peak$

$R_v = Lowest\ peak$

Using a stereo microscope (ZEISS Stemi 508), microscale pictures of the surfaces of the implants were captured (Figures 6-7 and 6-8). Carbon fibre particles were seen. Initially, the surfaces were smooth and shiny. However, some minor scratches were observed on the mating surfaces of the implants from handling.

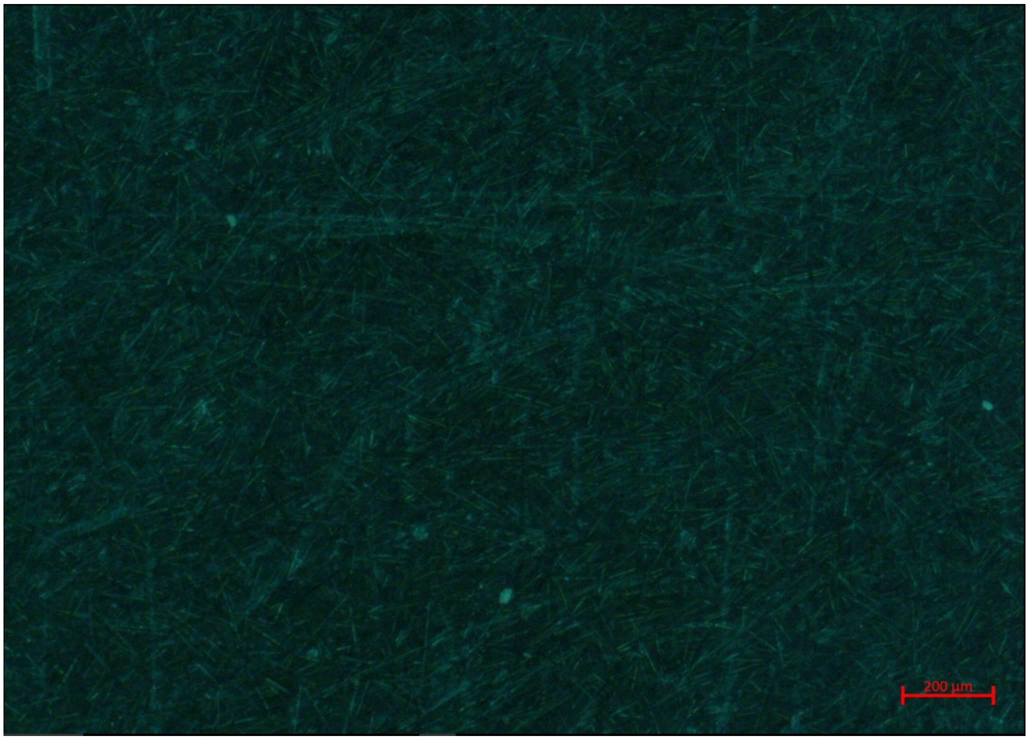

Figure 6-7: Surface of the calcaneus implant under the ZEISS Stemi 508

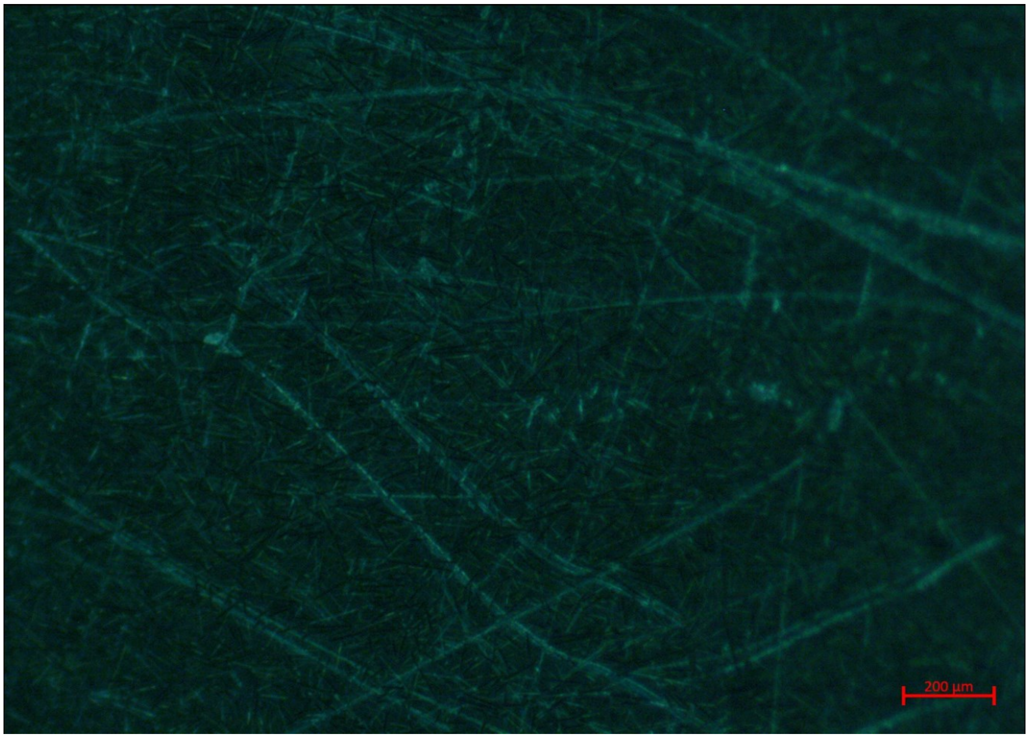

Figure 6-8: Surface of the talus implant under the ZEISS Stemi 508 microscope

Chapter 7 Results

7.1 Observations

Figure 7-1 gives a sample of the sinusoidal load output from the fatigue testing machine. When no rotation is applied, the machine outputs a smooth sinusoidal wave. Although a steady oscillation between -50 N and -800 N was maintained throughout testing, the sinusoidal wave was not smooth. Occasionally, the load rose to -35 N and dipped to -900 N. The values below -800 N were accompanied by noticeably louder sounds from the machine. This behaviour is expected since the fatigue-testing machine was designed for axial loading only. The rotation of the calcaneus jig causes lateral deflection of the shaft which is applying load from the crosshead of the fatigue-testing machine. Another observation is that the shaft connected to the crosshead of the machine was accumulating residue at the connection to the cross head of the fatigue-testing machine. This residue might be hydraulic fluid from the actuator, which might explain why the load dropped to -900 N and lower occasionally.

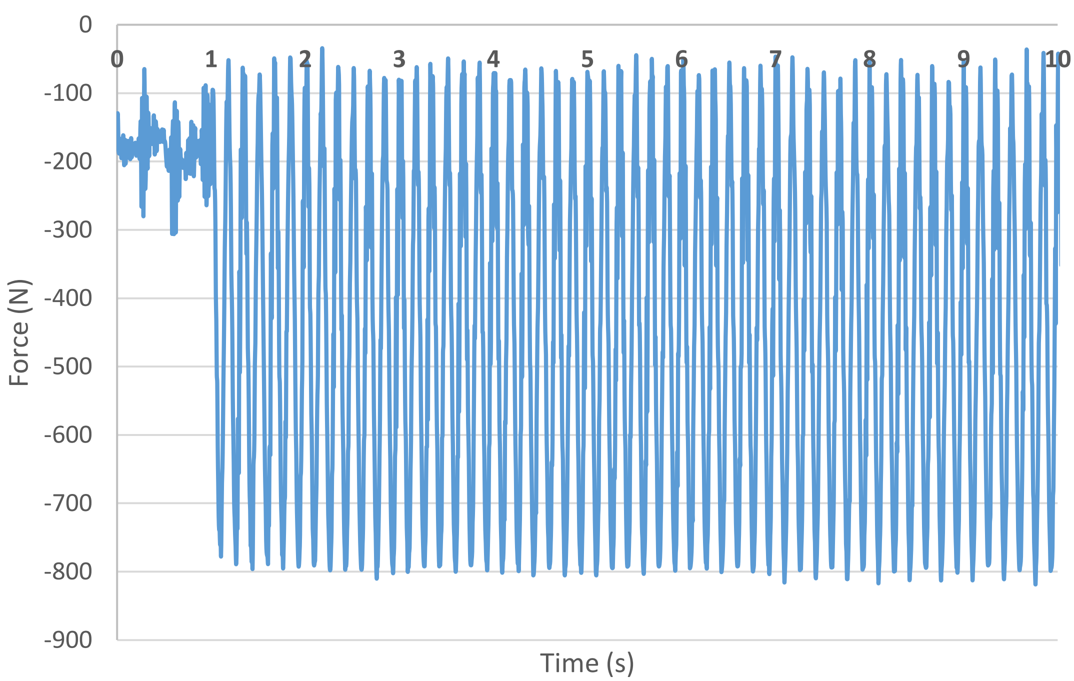

Figure 7-1: Sample load output from the fatigue-testing machine

The immersion fluid went from transparent (Figure 7-2) to cloudy at the end of testing (Figure 7-3). During the first 1.5 million cycles of testing, particles from the implants could be seen rising to the surface of the immersion fluid. This was not observed after 1.5 million cycles of testing, but it was observed from 2.5 to 3 million cycles of testing. It should be noted that approximately 0.15 litres, 15% of the fluid contained in the test chamber, leaked overnight from one the seals during the 2.5 to 3 million phase of testing. Deionized water was used to replace the fluid lost the next morning while testing was left to run to completion. Before the test from 3 to 3.5 million cycles was completed, the seal got damaged and the fluid leaking was contained. However, the bearing between the bushing and the coupler got damaged afterwards. This resulted in the implants being loaded without rotation for a few hours. At that point, testing was discontinued until the seals in the test chamber and the bearing were replaced. After testing was resumed, one of the seals got damaged again and the fluid leaking could not be contained. Therefore, the test chamber was constantly being refilled with the immersion fluid and deionized water until completion.

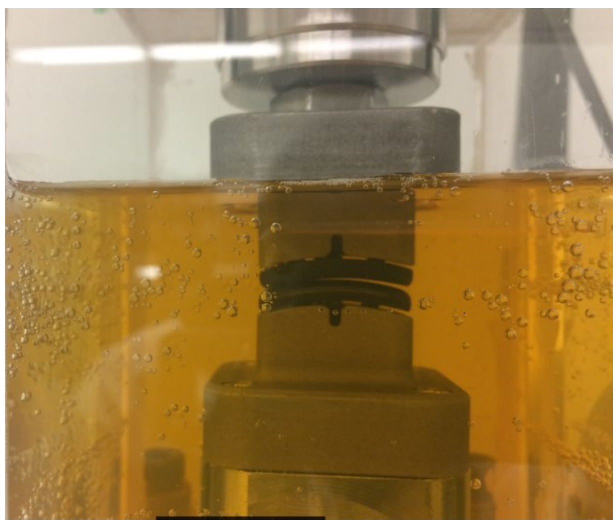

Figure 7-2: Transparent solution prior to testing

Figure 7-3: Cloudy solution after testing

7.2 Mass Measurement

Table 7-1 summarizes the change in mass of the talus and calcaneus implants after each interval of testing. Measurements were taken at 0.25 million, 0.5 million, 1 million, 2 million, 3 million and 4 million cycles.

Table 7-1: Masses of implants after each test

Cycles	Date	Mass (mg)		Mass Lost (mg)	
		Talus Implant	Calcaneus Implant	Talus Implant	Calcaneus Implant
Initial Mass	11/6/2017	4657.9	4889.25	-	-
Post-soak	11/8/2017	4635.5	4868.0	-	-
250,000	11/20/2017	4633.3	4865.1	1.1	2.1
500,000	11/27/2017	4627.9	4858.1	5.6	6.1
1,000,000	12/01/2017	4626.5	4855.9	1.4	2.2
2,000,000	12/14/2017	4619.7	4846.4	6.9	9.1
3,000,000	12/20/2017	4617.9	4844.0	1.8	2.5
4,000,000	01/15/2018	4615.3	4841.3	-2.8	-2.7

Figure 7-4 is a plot of the mean mass lost from Table 7-1. It should be noted that from 0.25 to 0.5 million cycles, testing was done intermittently instead of continuously. Initially, it was unclear whether intermittent testing caused a significantly larger loss in mass from 0.25 to 0.5 million cycles than the mass lost from inception to 0.25 million cycles and 0.5 to 1 million cycles. However, the cumulative mass lost from 0 to 1 million cycles is similar to the mass lost from 1 to 2 million cycles (Figure 7-5). Based on these results, continuous testing might not result in less mass loss than intermittent testing. Only continuous testing was done from 0.5 million cycles to completion. The mass loss of the implants was significantly less from 2 to 3 million cycles. After 4 million cycles of testing, the implants gained weight.

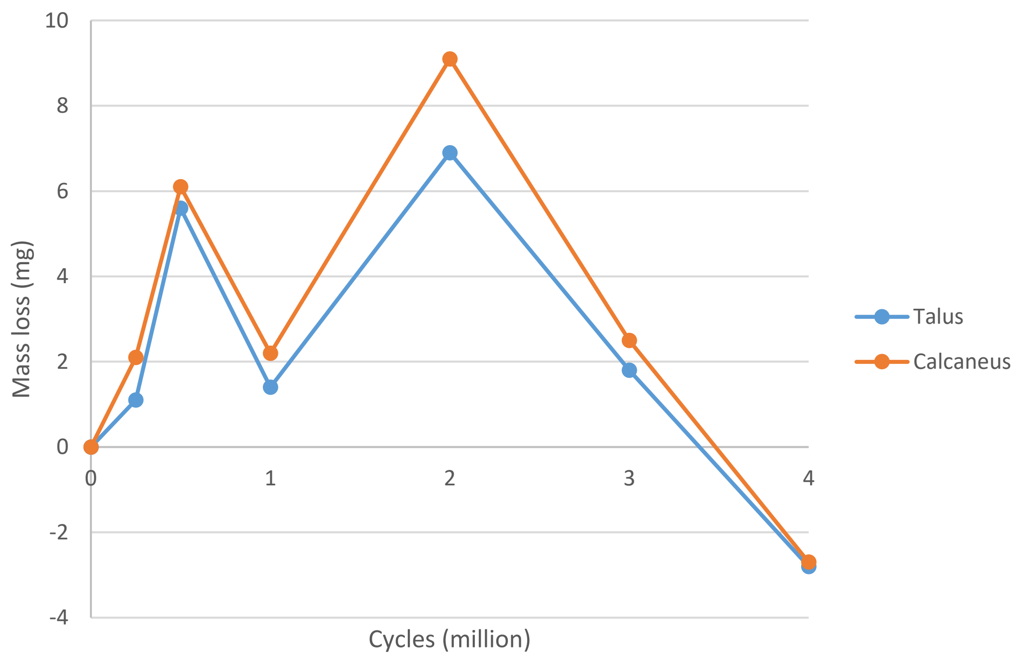

Figure 7-4: Mean mass loss of implants per million cycles of wear testing

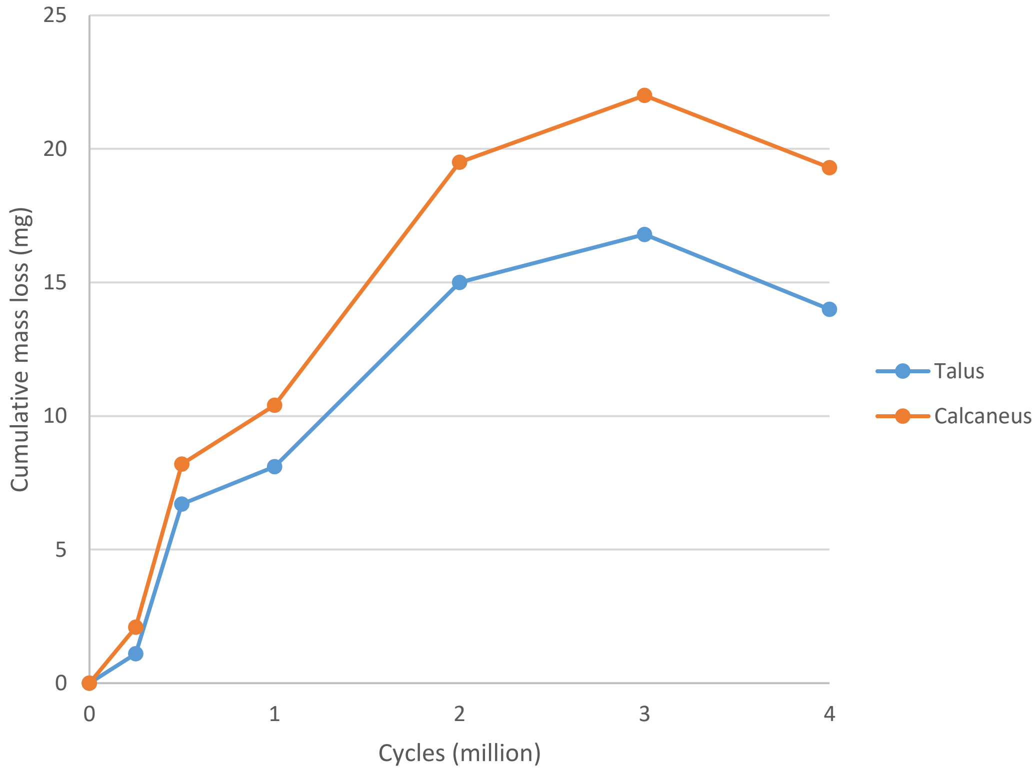

Figure 7-5: Cumulative mass loss of implants per million cycles of wear testing

Table 7-2 gives a more detailed account of the changing masses of the talus and calcaneus implants before testing, after conditioning the implants for testing and after every phase of wear testing. After conditioning, the talus and calcaneus implants were repeatedly cleaned, dried and weighed until the incremental mass difference was less than 10% of the cumulative mass difference (CMD). Weighing stopped after the masses stabilized, that is, at least two measurements were accurate within 0.1 mg of each other. The average of the accurate mass was rounded up and taken as the stable mass. Due to time constraints, it was not possible to test a control sample in this initial test.

Table 7-2: Detailed mass measurements of talus and calcaneus implants

Cycles	Date	Time	Mass (mg)	
			Talus	**Calcaneus**
Initial Mass	11/6/2017			
m1			4657.7	4889.1
m2			4657.8	4889.6
m3			4658.1	4889
m4			4658	4889.3
Average			**4657.9**	**4889.25**
Post-soak	11/8/2017		4637.9	4868.5
m10			4637	4869.4
m20			4637.1	4869.2
m30			4637	4869.1
m40			4637	4869.1
Stable Mass			**4637**	**4869.1**
CMD			0.004487	0.004121
Post soak cont'd	11/9/2017		4635.8	4868.7
m10			4636.1	4868
m20			4636	4868.2
m30			4636.1	4867.8
m40			4635.5	4867.9
m50			4635.4	4868
Stable Mass			**4635.5**	**4868**
CMD			0.000323	0.000226
% CMD			7.209382	5.481649
Pre-test	11/16/2017			
Initial Mass			**4634.4**	**4867.2**
Post Test	11/20/2017			
Pre-vacuum			4634.4	4866
m10			4633	4865.6
m20			4633.4	4865.2
m30			4633.3	4865.1
Stable Mass			**4633.3**	**4865.1**
Mass lost after 250,000 cycles			**1.1**	**2.1**
Pre-Test	11/23/2017			
Initial Mass			**4633.5**	**4864.2**

Post Test	11/27/2017			
Pre-vacuum			4628.5	4858.5
m10			4627.9	4859.4
m20			4627.8	4858.1
m30			4627.5	4858.3
m40			4627.9	4858.0
m50			4627.5	4857.8
m60			4627.9	4858.2
m70			4628.4	4858.4
m80			4627.9	4858.1
m90			4627.9	4858.1
Stable Mass			**4627.9**	**4858.1**
Mass lost after 500,000 cycles			**5.6**	**6.1**
Pre-Test	11/28/2017			
Initial Mass			4627.9	4858.1
Post Test	12/01/2017			
Pre-vacuum			4626.7	4857.2
m10			4626.4	4856.2
m20			4626.7	4856.1
m30			4626.5	4855.8
m40			4626.5	4855.9
m50			4626.5	4855.9
Stable Mass			**4626.5**	**4855.9**
Mass lost after 1,000,000 cycles			**1.4**	**2.2**
Pre-Test	12/06/2017			
Initial Mass			4626.6	4855.8
Post Test	12/14/2017			
Pre-vacuum			4620.2	4847.3
m10			4620.1	4847.5
m20			4620.1	4846.7
m30			4619.8	4846.7
m40			4619.6	4846.5
m50			4619.7	4846.4
Stable Mass			**4619.7**	**4846.5**
Mass lost after 2,000,000 cycles			**6.9**	**9.1**

Pre-Test	12/15/2017			
Initial Mass			4619.7	4846.5
Post Test	12/20/2017			
Pre-vacuum			4620.7	4846.6
m10			4619.7	4845.0
m20			4619.9	4846.2
m30			4619.7	4845.9
m40			4619.7	4845.8
m50			4617.6	4843.9
m60			4618.1	4844.1
m70			4618.1	4843.8
m80			4617.9	4844.1
m90			4617.9	4844.0
Stable Mass			4617.9	4844.0
Mass lost after 3,000,000 cycles			**1.8**	**2.5**
Pre-Test	01/08/2018			
Initial Mass			4612.5	4838.6
Post Test	01/15/2018			
Pre-vacuum			4615.9	4842.0
m10			4615.4	4842.3
m20			4615.1	4841.4
m30			4615.0	4841.5
m40			4615.3	4840.8
m50			4615.3	4841.4
m60			4615.3	4841.3
Stable Mass			4615.3	4841.3
Mass lost after 4,000,000 cycles			**-2.8**	**-2.7**

7.3 Visual Inspection of Surfaces

Throughout testing, the mating surfaces of the implants obtained white wear marks along the path of eversion/inversion. From 0 to 0.25 million cycles, the calcaneus jig slid backwards on the shaft and was slightly offset. This is the reason why wear marks are not seen on the lower portion of the calcaneus implant (Figure 7-6). After preventing the calcaneus jig from slipping with shaft collars and Velcro tape, the implants were aligned for the remainder of testing. Consequently, the worn area on the mating surfaces of the implants kept expanding further as testing continued. However, the intensity of the wear marks decreased as testing continued. This trend is depicted in Figures 7-6 to 7-10.

Figure 7-6: Implants after 250,000 cycles of testing

Figure 7-7: Surfaces of implants after 500,000 cycles of testing

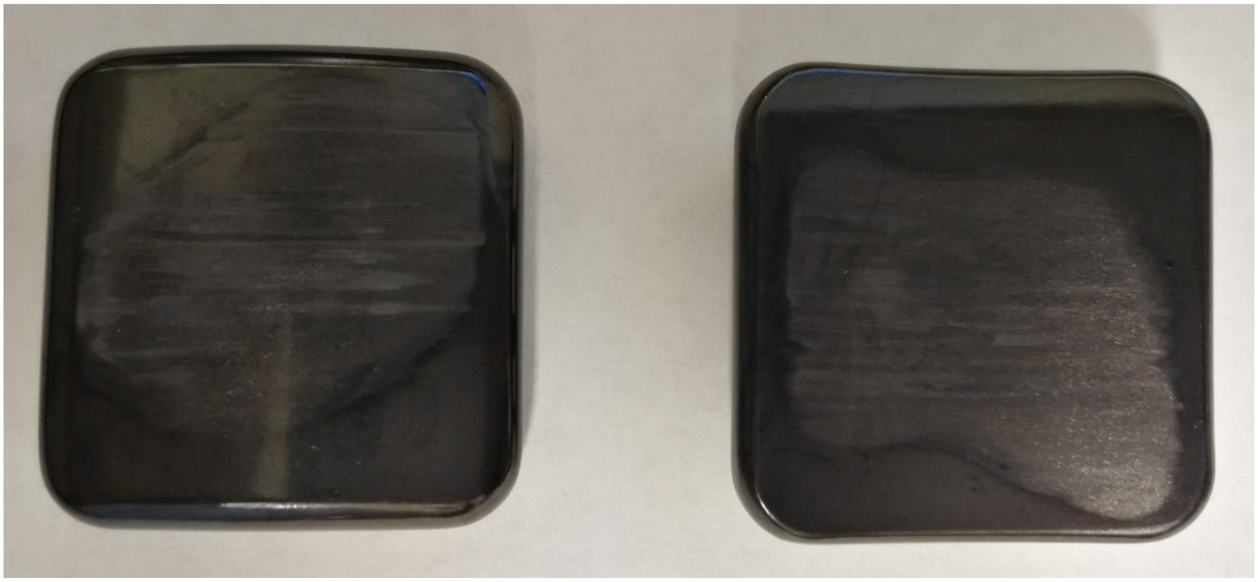

Figure 7-8: Surfaces of implants after 1,000,000 cycles of testing

Figure 7-9: Surfaces of implants after 2,000,000 cycles of testing

Figure 7-10: Surfaces of implants after 3,000,000 cycles of testing

Figure 7-11: Surfaces of implants after 4,000,000 cycles of testing

7.4 Roughness & Surface Characterization

Table 7-3 summarizes the roughness measurements after every phase of testing. After 0.25 million cycles of testing, the roughness increased slightly from the initial values, which is confirmed in the relatively small loss in mass. The roughness of both implants significantly increased from 0.25 million to 0.5 million cycles of testing. This corresponds to the significant mass lost during this phase of testing. Thus, there may be a relationship between increase in roughness and the magnitude of the mass lost.

Based on the values obtained, the roughness may have stabilized after 0.5 million cycles for both implants. Fluid leaked profusely during the 3.5 to 4 million cycles test phase due to a damaged seal which caused a layer of film to form between the mating surfaces of the implants. After four million cycles, the roughness significantly decreased for both implants as seen in Table 7-4 which gives a clearer idea of the variance in the values of the roughness in comparison to the mean calculated in Table 7-3.

Table 7-3: Mean roughness measurements for talus and calcaneus implants

No. of Test Cycles	**Talus Implant**			**Calcaneus Implant**		
	Ra (nm)	*rms (nm)*	*PV (μm)*	*Ra (nm)*	*rms (nm)*	*PV (μm)*
0	329.25	389.90	7.44	239.48	284.19	8.27
250,000	476.7	627.23	15.78	609.46	783.87	15.01
500,000	1851.0	2463.9	133.37	1394.38	1732.15	150.27
1,000,000	1651.06	2190.95	154.11	1555.80	2190.87	133.99
2,000,000	1204.44	1626.03	130.41	1344.27	1751.36	113.74
3,000,000	1695.51	2069.42	68.37	1321.00	1722.25	137.37
4,000,000	591.26	848.27	82.36	1145.99	1486.32	129.37

Table 7-4: Variation of roughness measurements per implant

No. of Test Cycles	Talus Implant			Calcaneus Implant		
	Ra (nm)	*rms (nm)*	*PV (μm)*	*Ra (nm)*	*rms (nm)*	*PV (μm)*
0	327.87	387.11	6.24	242.23	286.85	4.12
	325.14	386.64	4.60	228.94	279.13	6.95
	332.16	394.19	7.44	247.29	286.58	8.27
500,000	2559.60	3166.61	69.857	1803.86	2163.92	111.59
	1383.03	1925.44	73.31	1231.53	1550.52	105.72
	1851.00	2299.50	133.37	1262.45	1603.55	148.67
1,000,000	1629.09	2069.79	154.11	1858.01	2927.88	133.99
	1918.96	2438.61	129.90	2752.07	3687.43	131.23
	1405.14	1821.44	130.79	1086.86	1334.56	70.23
2,000,000	1154.01	1610.42	130.41	1074.43	1424.63	113.74
	1253.23	1707.87	61.49	1345.36	1659.32	22.65
	647.75	998.38	95.08	1363.17	1801.68	41.51
	1762.77	2187.44	24.26	1594.11	2119.82	79.93
3,000,000	2111.19	2525.53	22.86	2807.96	3340.68	25.63
	1941.49	2349.14	23.96	799.79	1164.69	52.59
	1838.55	2226.08	20.58	621.97	980.16	137.37
	1052.14	1371.33	68.37	714.46	1079.63	122.96
	1534.2	1875.00	19.96	1660.81	2046.10	29.07
4,000,000	557.09	787.79	20.10	1631.89	1962.00	37.17
	556.95	759.34	56.42	797.65	1045.36	42.16
	543.02	795.17	19.98	976.35	1277.73	72.09
	707.98	1050.79	82.36	842.83	1240.13	105.19

The intensity maps from the profilometer scans give a clearer picture of the evolution of the mating surfaces of the calcaneus (Figure 7-11) and talus (Figure 7-12) implants. The intensity of the wear marks correspond to the significant increase in roughness for both the talus and calcaneus implants after 0.5 million cycles of testing. However, as testing continued to 4 million cycles, the intensity of the wear marks on the surfaces of both implants varied.

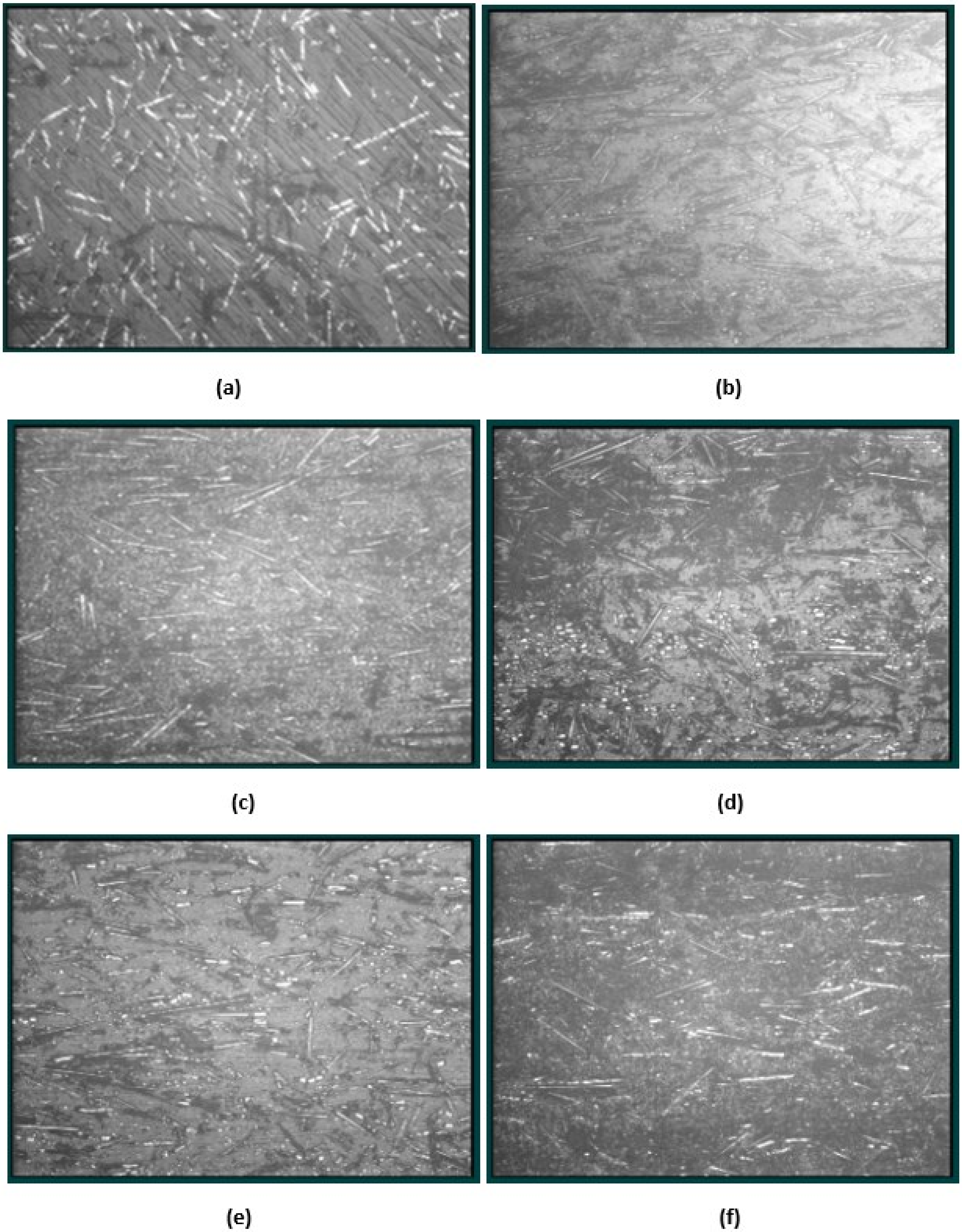

Figure 7-12: Intensity map of Calcaneus Implant (a) Pre-Testing (b) 500,000 cycles (c) 1,000,000 cycles (d) 2,000,000 cycles (e) 3,000,000 cycles (f) 4,000,000 cycles

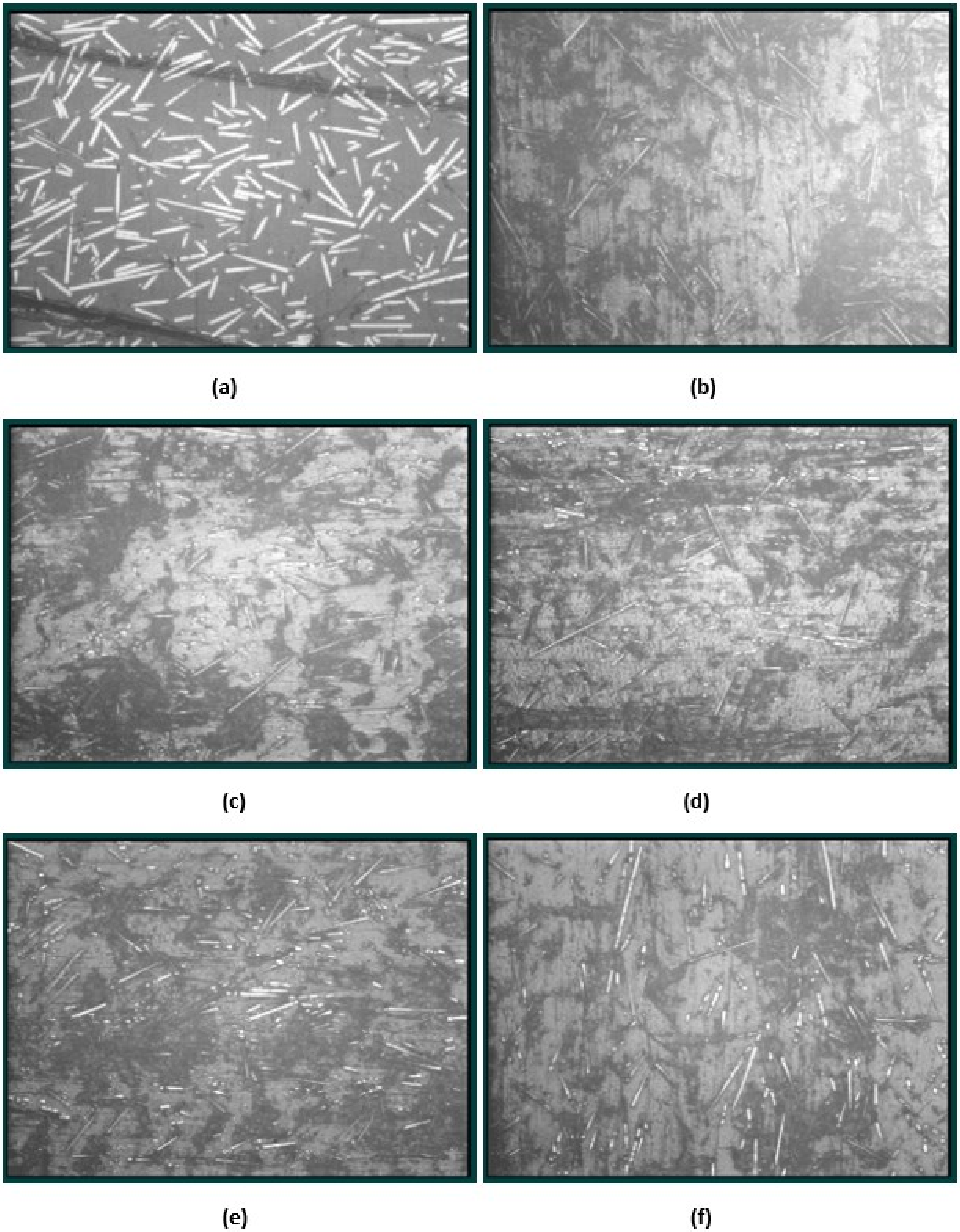

Figure 7-13: Intensity map of Talus Implant (a) Pre-Testing (b) 500,000 cycles (c) 1,000,000 cycles (d) 2,000,000 cycles (e) 3,000,000 cycles (f) 4,000,000 cycles

7.5 Discussion

According to the supplier, the implants were specially manufactured to have some micro-porousity. Therefore, the implants were expected to gain weight after being pre-soaked and conditioned for testing. However, this was not the case. Several balances were used to measure the mass of the implants prior to soaking and they all gave approximately the same result. The readings on the balances were also zeroed prior to taking mass measurements of the implants before and after soaking. To validate these results, this pre-soaking procedure should be repeated on more implants to see if a similar trend occurs. If this is the case, then it would indicate that the implants did not have any micro porosity.

Inconsistent trends were observed during the first 1 million cycles of testing. After 0.25 million cycles, the mass lost was significantly less than the mass lost after 0.5 million cycles. Then, the mass lost from 0.5 to 1 million cycles was similar to the mass lost after 0.25 million cycles. It should be noted that intermittent testing was done over a period of 3 days from 0.25 to 0.5 million cycles. The machine was left to run for 3.5 hours the first day, 11.5 hours the second day and 8 hours on the third day. This was done to monitor the machine throughout the day because loosening of the four-bar mechanism from 0 to 0.25 million cycles caused a significant delay with repairs. It was initially assumed that the mass lost was higher during this phase due to the possibility that particles could have gotten built up between the mating surfaces of the implants and result in abrasion. However, this may not have been the case.

The machine was left to run continuously from 1 to 1.5 million cycles, approximately two days. After this, the fluid was removed from the test chamber. The implants were rinsed with deionized water and stored in a sealed, dust free container until testing from 1.5 to 2 million cycles resumed two days later. During the two days, the mechanical seals for the test chamber were replaced. After 2 million cycles of testing, the mass lost from the talus and calcaneus implants (6.9 mg and 9.1 mg respectively) was comparable to the sum of the mass lost from 0 to 1 million cycles (8.1 mg and 10.4 mg respectively).

Unfortunately, the fluid in the bath leaked during the 2 to 3 million cycles and even more profusely during 3.75 to 4 million cycles. Consequently, significantly less mass was lost from the talus and calcaneus implants after 3 million cycles (1.8 mg and 2.5 mg respectively) in comparison to the mass lost after 1 and 2 million cycles. Initially, it was expected that a comparable mass loss would be observed after 1, 2, 3 and 4 million cycles. Reinders et al (2015b) performed wear testing on knee replacement implants which were immersed in different levels of fluid. The findings of these experiments showed that the lower levels of fluid had lower wear rates. A probable reason for this could be that the lower volumes of fluid were more turbid and had more precipitation than the higher volumes of fluid. Therefore, with lower volumes of fluid the bovine serum degraded faster. A lower volume of fluid would also get to higher temperatures within the same amount of time. Higher temperatures encourage the degradation of bovine serum. Thus, the reduction in fluid level may have been the cause of the lower wear rate observed during this phase of testing.

In addition to the profuse leaking during 3.75 to 4 million cycles, the bearing between the taper-lock bushing and the coupler got damaged overnight during 3.25 to 3.5 million cycles. Therefore, the implants were loaded without rotation for a several hours. The immersion fluid after 4 million cycles was also observed to be the most turbid upon completion of testing in comparison to the previous tests when the fluid was changed. In addition to the very turbid solution, a layer of film was discovered on the surfaces of the implants and calcaneus jig after the completion of 4 million cycles of testing. This layer of film in addition to the period of non-articulating loading might be the reason why both the talus and calcaneus implants gained weight after 4 million cycles of testing. A similar trend was observed by Scholes et al, (2008). An overall increase in mass was accompanied with a white film on the area of contact of the acetabular cup.

Xin et al (2013) performed wear testing of PEEK based self-mating total cervical disc replacements. The results confirmed a higher wear rate, 4.8 ± 1.5 mg/10^6 cycles, during the run-in phase (0 to 2 million cycles) in comparison to 1.0 ± 0.9 mg/10^6 cycles during the steady state phase (3 to 5 million cycles). Further testing under the same conditions should be done to confirm the trends observed during this test. Then, one would be able to determine whether the reduction in mass lost after 2 million cycles was a result of the transition from the run-in to the steady state phase or the fluid leaked.

It is unclear why discrepancies in the mass lost occurred from 0 to 1 million cycles of testing. However, a notable observation is that the implants were not tested within the same time frame due to failures. In the future, any delays between testing should be made as consistent as possible in order to establish consistency. The cleaning, drying and weighing procedure should also be strictly adhered to in order to minimize error. Another thing to note is that the standards require a loaded soak control, (i.e. implants subjected to load and no rotation) to be tested simultaneously. This is necessary to correct the mass lost. With this experiment, it was not possible to do so within the allotted time for testing and the fact that the machine was designed with only one station for testing.

Initially, the roughness (Ra) of the implants increased after 0.5 million cycles and varied between 1000 and 2600 nm up to 3 million cycles of testing. However, the implants appeared to be smoothing after 2 million cycles of testing based on the decreasing intensity of the white wear marks. This may be indicative of a change in the layers within the implants. After 4 million cycles of testing, the intensity of the white wear marks increased. Xin et al (2013) observed that the roughness of mating surfaces of the PEEK cervical disc replacements decreased after testing. This observation was confirmed with a visual inspection of the mating surfaces. Machining marks which were present prior to testing were removed and the surface appeared to be polished after the completion of testing.

The profilometer does not give the appropriate output required to specify the wear mechanism failure such as pitting, delamination, and abrasion to name a few. Any black spots in the 2D and 3D diagrams are an indication of missing data, not holes in the surfaces of the implants. Scanning electron microscopy (SEM) would indicate the wear mechanism failure for the implants. However, this should be done after the completion of testing, since the implants would need to be coated with gold prior to using the appropriate SEM machine.

Chapter 8 Conclusion

8.1 Summary

The aim of this research was to design a wear testing simulator specifically for the subtalar joint and to perform wear testing on a pair of carbon fiber reinforced polyether-ether-ketone (PEEK) subtalar joint prostheses. Wear testing typically involves the application of load and rotary displacement to implants. A fatigue-testing machine was available for applying load only. Therefore, a detachable mechanism was needed to apply rotary displacement to samples tested in the fatigue-testing machine. A four-bar crank rocker mechanism was selected and designed to provide rotary displacement.

The first stage of the design phase was to create a 3D model of the fatigue-testing machine and the four-bar mechanism and assemble all the parts together. This was done to minimize the manufacturing errors and get a general idea of how the parts would fit in the available space of the machine. Then, numerical analysis was used to optimize the operation of the mechanism and ensure that it does not fail. Several methods were used to validate the results from the numerical analyses. To address fatigue, Finite Element Analysis (FEA) was used to estimate the principal stresses in the four-bar mechanism. The torque required to drive the mechanism was also validated using FEA and a dynamic force analysis.

After confirming that the device would work on paper, the parts were purchased or machined and assembled. Several adjustments were made to account for manufacturing and calculation errors. Initial testing was done with 3D printed subtalar joint implants to get an idea of what problems may arise during actual testing.

During the actual test phase, unforeseen problems came up with the simulator. These problems were all dealt with and the simulator functioned well. The mass lost and change in roughness were measured for the pair of implants after each interval of testing. In summary, the machine worked for the loading conditions that it was designed for.

8.2 Conclusion

Creating a 3D model prior to building the mechanism was very useful. However, parallax errors with measurements of the fatigue-testing machine, manufacturing errors and calculation errors resulted in hole misalignments. Finite Element Analysis is a very concise tool for validating mechanical design. Abaqus CAE 6.14 is able to provide deflection, displacement, stress and torque of a model during a dynamic analysis. The results compared well with SAM 7.0 and a traditional dynamic force analysis.

Using a four-bar crank rocker mechanism was sufficient for testing to run continuously for 0.5 million cycles of rotation, approximately 2 days, without failing from fatigue. However, unexpected means of failure and difficulties which were not considered during the design phase were encountered. Some failures include leaks as a result of hole misalignments, bolts getting loose and causing the mechanism to disassemble, awkward positions to work in and the inconvenience of having to disassemble the entire test set up to replace failed parts. While it is necessary to have some play in the design of machines so that parts would fit better, precision is absolutely necessary for some parts to operate optimally. These factors should be taken into consideration for the design of any mechanical part. The fatigue-testing machine is also not designed for anything other than axial loading. Sometimes, the machine did not respond well after rotation was applied. Either significantly higher loads than the load programmed was being output or the implants lost contact. Several attempts had to be made to remediate these problems.

The mass lost from 0 to 1 million was comparable to the mass lost from 1 to 2 million cycles. However, there was a considerable reduction in the mass loss after 3 million cycles and a mass gain after 4 million cycles. More samples should be tested to observe whether this trend continues or not. Having a loaded soak control tested simultaneously would help to correct the mass lost and calculate the wear rate per million cycles as it is expected to gain mass from absorbing the test fluid. Measuring the surface roughness of the implants was difficult since the implants had convex/concave surfaces and they were also tilted in another direction. The profilometer used was not designed for measuring sloped samples. The roughness increased and varied between 1000 and 2600 nm from 0.5 million to 3 million cycles of testing. However, the roughness decreased after 4 million cycles of testing.

It is too early to conclude whether the suggested implants are adequate as surface reconstructs for the subtalar joint. The machine should also be improved so that the likelihood of leakage from the shaft seals and mechanical failure of the ball bearings at the connections of the four-bar mechanism is minimized. One suggestion to increase the lifespan of the shaft seals would be to ensure that all the holes on the test chamber and mounted ball bearings are aligned to minimize damage. The ball bearings should also be replaced periodically as they are inexpensive. As previously mentioned, further testing needs to be done at 1 Hz, 37°C and with a load pattern that is comparable to that of the ankle joint. Several pairs of implants of the same CFR PEEK composition should be tested in order to validate the wear rate obtained in this test and get an idea of the wear mechanisms that the implants will be subject to. Other commonly used materials for orthopaedic implants such as UHMWPE should be tested to determine which one would have the lowest wear rate and as a result, is best suited for a subtalar joint surface reconstruct.

8.3 Recommendations for Future Research

During the testing phase, the limitations of the subtalar joint prostheses wear testing simulator were identified. There were several times when various mechanical parts loosened or got damaged and interrupted experiments. Thus, the most important recommendation is to synchronize the VFD to the data acquisition box of the fatigue-testing machine. In doing so, the rotation will stop once the fatigue-testing machine is completed with testing. It would be helpful if a conditional statement could be programmed into the machine so that if at any point the four-bar mechanism loosens, and no rotation is being applied to the calcaneus jig, the experiment would stop. However, one would need some sort of sensor to detect the detachment of the four-bar mechanism from the motor in order to do so.

Another recommendation is to ensure that the heights of the holes in the mounted ball bearings and test chamber are aligned. Misalignment of these holes damaged the seals in the test chamber and testing was delayed so that the seals could be replaced frequently. Although the seals were inexpensive, it is convenient to disassemble the entire setup just to change the seals so frequently.

There is a need to maintain the level of the immersion fluid as this results in less mass lost during wear testing. Another requirement, according to ISO 14242-1, is to maintain the temperature at 37°C throughout wear testing. This is the normal temperature of the human body. On the contrary, heating the immersion fluid increases microbial growth and the buildup of protein precipitation which may form a layer between the articulating surfaces of the implants and reduce the wear rate (Liao et al, 2003). The temperature of the immersion fluid also rises from the heat accompanying the frictional forces from articulation and the constant running of wear testing simulators. When the change in temperature is high enough, the properties of the lubricant and articulating surfaces can also change and lead to unexpected wear mechanisms (Liao et al, 2003). For this reason, there have been debates concerning whether the temperature of the immersion fluid should be heated to 37°C or not (Smith et al, 2016).

Since a considerably thick steel plate was placed on top of the original plate and the test chamber was elevated from the ground to reduce the amount of fluid required in our design, we lost the ability to regulate the temperature of the immersion fluid, which is a feature of the fatigue-testing machine. However, the temperature of the fluid did rise from the frictional forces generated between the mating surfaces of the implants and the mechanical parts during testing. A suggestion would be to have the smaller test chamber bolted on to the original plate and small enough so that it can be placed inside the original test chamber. In doing so, the original test chamber can be filled with distilled water to the level of the immersion fluid and the temperature of the test chamber could be regulated. A thermocouple can also be attached to the smaller chamber to monitor the temperature of the immersion fluid and the articulating parts.

On the other hand, designing a test setup in which the shaft goes through so many test chambers might cause issues with alignment. An alternate solution is to use a shaft with a larger diameter and replace the test chamber for the immersion fluid with a bag of a strong enough elastic material that can stretch without breaking and will not melt at temperatures around 37°C (Figure 8-1). This bag should be fastened around the talus and calcaneus jigs to hold the immersion fluid. In this way, the amount of fluid required for testing can be further minimized in addition to minimizing issues with misalignments of holes.

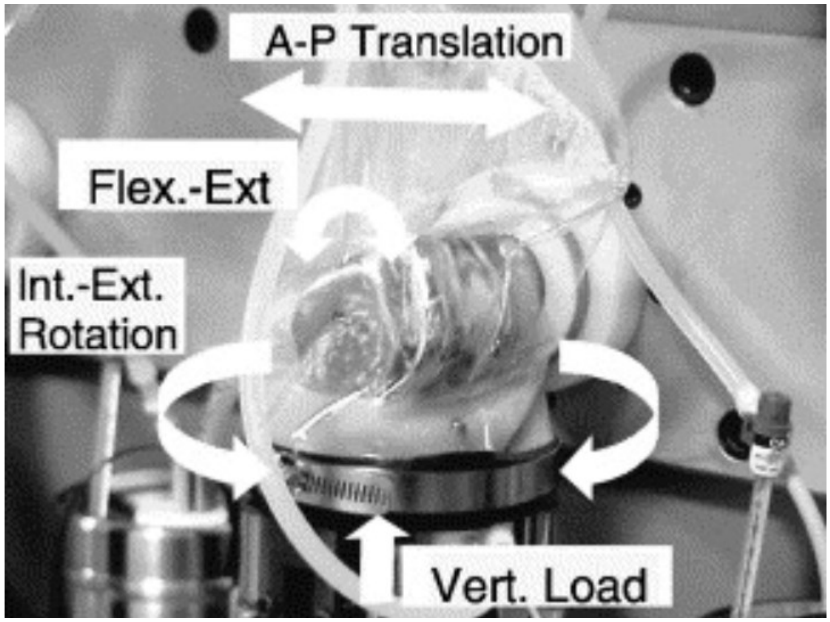

Figure 8-1: Knee simulator wear test setup (Laurent et al, 2003)

The attachment of the talus jig to the extension shaft also needs improvement as aligning it perfectly proved difficult with a threaded bolt and nut. A viable suggestion is to use a snap lock, so that it just locks into position and can be easily removed. In addition, the loading shaft can be braced to minimize deflection.

Continuous testing at 1 Hz is recommended so that the mass lost during testing can be reduced. A machine designed for measuring the roughness of sloped implants should be used to get more accurate readings for surface roughness parameters. The implants should also be tested using other materials such as ultra-high molecular weight polyethylene (UHMWPE) to see determine which material would be best suited for subtalar joint implants. Finally, it would be ideal to use another fatigue-testing machine so that a loaded control sample can be tested simultaneously. In doing so, the mass lost during testing can be corrected in real time and the wear rate can be measured using the gravimetric method.

References

Adeeb, S. M. (2005). Load bearing across diarthrodial joints with special reference to peripheral structures and the menisci of the knee.

Affatato, S., Leardini, A., Leardini, W., Giannini, S., & Viceconti, M., (2007). Meniscal wear at a three-component total ankle prosthesis by a knee joint simulator. *J. Biomech.* 40, 1871-1876.

Arthritis of the foot and ankle. April 20, 2016. Retrieved from http://orthoinfo.aaos.org/topic.cfm?topic=a00209

Bandhyopadhya, A., & Bose, S. (2013). Characterization of biomaterials. Amsterdam: Elsevier.

Barton, T., Lintz, F., & Winson, I. (2011). Biomechanical changes associated with the osteoarthritic, arthrodesed, and prosthetic ankle joint. *Foot Ankle Surg* 17 (2): 52-7.

Bell, C. J., & Fisher, J. (2007). Simulation of polyethylene wear in ankle joint prostheses. *J. Biomed. Mater. Res. Par B: Appl. Biomater.* 81B, 162-167.

Bhandari, M. & Adili, A., (2011). Evidence-based Orthopedics. Oxford: John Wiley & Sons.

Bragdon, C. R., O'Connor, D. O., Lowenstein, J. D., Jasty, M., Biggs, S. A., & Harris, W. H., (2001). A new pin-on-disk wear testing method for simulating wear of polyethylene on cobalt-chrone alloy in total hip arthroplasty. *J. Arthroplasty,* 16, 658-665.

Bragdon, C. R., O'Connor, D. O., Lowenstein, J. D., Jasty, M., & Syniuta, W. D. (1996). The importance of multidirectional motion on the wear of polyethylene. *Proc. Inst. Mech. Eng. Part H. J. Eng. Med.* 2110, 157-165.

Brockett, C. L., & Chapman, G. J. (2016). Basic science: Biomechanics of the ankle. *Orthopaedics And Trauma*, *30*232-238. doi:10.1016/j.mporth.2016.04.015

Brockett, C., John, G., Williams, S., Jin, Z., Isaac, G., & Fisher, J. (n.d). Wear of ceramic-on-carbon fiber-reinforced poly-ether ether ketone hip replacements. *Journal Of Biomedical Materials Research Part B-Applied Biomaterials*, 100B(6), 1459-1465.

BS ISO 14242-2:2000 Implants for surgery. Wear of total hip-joint prostheses. Methods of Measurement. (2000). BSI Standards Limited.

BS ISO 14242-1:2014 Implants for surgery. Wear of total hip-joint prostheses. Loading and displacement parameters for wear-testing machines and corresponding environmental conditions for test. (2014). BSI Standards Limited.

Burdett, R. G. (1982). Forces predicted at the ankle during running. *Medicine & Science In Sports & Exercise*, (4), 308.

Brodner, W., Bitzan, P., Meisinger, V., Kaider, A., Gottsauner-Wolf, F., & Kotz, R. (2003). Serum cobalt levels after metal-on-metal total hip arthroplasty. *Journal of Bone and Joint Surgery-American Volume*, 85(11), 2168-2173.

Chi, K. J. & Schmitt, D. (2005). Mechanical energy and effective foot mass during impact loading of walking and running. *Journal of Biomechanics*, 38: 1387-1395.

Chyr, A., Qiu, M., Speltz, J. W., Jacobsen, R. L., Sanders, A. P., & Raeymaekers, B. (2014). A patterned microtexture to reduce friction and increase longevity of prosthetic hip joints. Wear, 31551-57. doi:10.1016/j.wear.2014.04.001

Deland, J. T., Morris, G.D. & Sung, I. H. (2000). Biomechanics of the ankle joint. A perspective on total ankle replacement. Foot Ankle Clin 2000;5:747–59.

Drake, R. L., Vogl, W., & Mitchell, A. M. (2014). Gray's anatomy for students. Edinburgh: Churchill Livingstone, 2014.

Dynamic force analysis. July 26, 2017. Retrieved from http://ocw.metu.edu.tr/pluginfile.php/6467/mod_resource/content/6/ch6/6-5.htm

Early, J. S. (2008). Talus fracture management. Foot Ankle Clin N Am, 13:635-657.

Eloesser, L. (1913). Implantation of Joints. *California State Journal of Medicine*, 11(12), 485-491.

Goetz, J., Baeurle, M., Dullien, S., Grifka, J., Koeck, F., & Baier, C. (2017). Postural Stability after Unicondylar Knee Arthroplasty and Patient-Specific Interpositional Knee Spacer. Biomed Research International, 1-9. doi:10.1155/2017/5836025

Goetz, J., Schiessl, S., Baier, C., Dullien, S., Mueller, K., Grifka, J., & Koeck, F. (2017). Postural stability after patient-specific interpositional knee spacer or total knee arthroplasty: a comparative study. International Orthopaedics, 41(1), 67-73. doi:10.1007/s00264-016-3266-4

Gougoulias, N., & Maffulli, N. (2013). History of total ankle replacement. Clinics In Podiatric Medicine & Surgery, 30(1), 1-20. doi:10.1016/j.cpm.2012.08.005

Gougoulias, N., Khanna, A. & Maffulli, N. (2010). How successful are current ankle replacements? A systematic review of the literature. *Clinical Orthopaedics and Related Research*, 468(1):199–208

Haddad, S. L., Coetzee, J. C., Estok, R., Fahrbach, K., Banel, D., and Nalysnyk, L., (2007). Intermediate and long-term outcomes of total ankle arthroplasty and ankle arthrodesis. A systematic review of the literature. *J Bone Joint Surg Am*, 89 (9): 1899-905.

Interactive Four-Bar Linkage Dynamic Force Analysis. August 4, 2017. Retrieved from https://www.softintegration.com/chhtml/toolkit/mechanism/fourbar/fourbardynamics.html

Jastifer, J. R., & Gustafson, P. A. (2014). The subtalar joint: biomechanics and functional representations in the literature. Foot (Edinburgh, Scotland), 24(4), 203-209. doi:10.1016/j.foot.2014.06.003

Kapandji, A. I. (2011). The Physiology of the Joints Volume Two The Lower Limb. Toronto: Elsevier.

Kohlrusz, G. & Fodor, D. (2011). Comparison of scalar and vector control strategies of induction motors. *Hungarian Journal of Industrial Chemistry Veszprem*, 39(2), 265-270.

Kretzer, J. P., Jakubowitz, E., Reinders, J., Lietz, E., Moradi, B., Hofmann, K., & Sonntag, R. (2011). Wear analysis of unicondylar mobile bearing and fixed bearing knee systems: A knee simulator study. Acta Biomaterialia, 7710-715. doi:10.1016/j.actbio.2010.09.031

Labek, G., Thaler, M., Janda, W., et al. (2011). Revision rates after total joint replacement: cumulative results from worldwide joint register datasets. *Journal of Bone & Joint Surgery Br* 2011;93(3):293–7.

Laurent, M., Johnson, T., Yao, J., Blanchard, C. & Crowninshield, R. (2003). Case study: In vitro lateral versus medial wear of a knee prosthesis. *Wear, 255*(14th International Conference on Wear of Materials), 1101-1106. doi:10.1016/S0043-1648(03)00271-0.

Liao, Y., McKellop, H., Lu, Z., Campbell, P., & Benya, P. (2003). The effect of frictional heating and forced cooling on the serum lubricant and wear of UHMW polyethylene cups against cobalt–chromium and zirconia balls. Biomaterials, 243047-3059. doi:10.1016/S0142-9612(03)00148-0

Lord, G., & Marotte, J. H. (1980). [Total ankle replacement (author's transl)]. Revue De Chirurgie Orthopedique Et Reparatrice De L'appareil Moteur, 66(8), 527-530.

Lyons, M., MacDonald, S., Somerville, L., Naudie, D., & McCalden, R. (n.d). Unicompartmental Versus Total Knee Arthroplasty Database Analysis: Is There a Winner?. Clinical Orthopaedics And Related Research, 470(1), 84-90.

Mahato, N. K. and Murthy, S. N., (2012). Articular and angular dimensions of the talus: inter-relationship and biomechanical significance. *The Foot*, 22: 85-89.

Michael, J. M., Golshani, A., Gargac, S., & Goswami, T. (2008). Review article: Biomechanics of the ankle joint and clinical outcomes of total ankle replacement. *Journal of The Mechanical Behavior of Biomedical Materials*, *1*276-294. doi:10.1016/j.jmbbm.2008.01.005

Myszka, D. H. (2012). *Machines and mechanisms: applied kinematic analysis.* 4th ed. Upper Saddle River, N.J.: Pearson Prentice Hall.

Nebergall, A. K., Rader, K., Palm, H., Malchau, H., & Greene, M. E. (2015). Precision of radiostereometric analysis (RSA) of acetabular cup stability and polyethylene wear improved by adding tantalum beads to the liner. Acta Orthopaedica, 86(5), 563-568. doi:10.3109/17453674.2015.1054255

Nikolaos E., G., Anil, K., & Nicola, M. (2009). History and evolution in total ankle arthroplasty. British Medical Bulletin, (1), 111.

Nishikawa, K., Okazaki, K., Matsuda, S., Tashiro, Y., Kawahara, S., Nakahara, H., & ... Iwamoto, Y. (2014). Improved design decreases wear in total knee arthroplasty with varus malalignment. Knee Surgery, Sports Traumatology, Arthroscopy, 22(11), 2635-2640.

Norton, R. L. (2014). *Machine design: an integrated approach.* Fifth edition. Boston: Prentice Hall.

Norton, R. L. (2008). *Design of machinery: an introduction to the synthesis and analysis of mechanisms and machines.* 4th ed. Dubuque, IA: McGraw-Hill.

Pappas, M. J., Makris, G., & Buechel, F. F., (1995). Titanium nitride ceramic film against polyethylene. A 48 million cycle wear test. *Clin. Orthop. Relat. R.* 317, 64-70.

Pal, G. P., & Routal, R. V. (1998). Architecture of the cancellous bone of the human talus. Anatomical Record, 252(2), 185-193. doi:10.1002/(SICI)1097-0185(199810)252:2<185::AID-AR4>3.0.CO;2-2

Pivec, R., Johnson, A. J., Mears, S. C., & Mont, M. A. (2012). Seminar: Hip arthroplasty. The Lancet, 3801768-1777. doi:10.1016/S0140-6736(12)60607-2

Price, A., Waite, J., & Svard, U. (n.d). Long-term clinical results of the medial Oxford unicompartmental knee arthroplasty. Clinical Orthopaedics and Related Research, (435), 171-180

Reinders, J., von Stillfried, F., Altan, E., Sonntag, R., Heitzmann, D. W., & Kretzer, J. P. (2015a). Force-controlled dynamic wear testing of total ankle replacements. Acta Biomaterialia, 12332-340. doi:10.1016/j.actbio.2014.10.036

Reinders, J., Sonntag, R., & Kretzer, J. P. (2015b). Synovial fluid replication in knee wear testing: An investigation of the fluid volume. *Journal of Orthopaedic Research,* (1), 92. doi: 10.1002/jor.22736

Rockar, P. J. (1995). The subtalar joint: anatomy and joint motion. The Journal of Orthopaedic and Sports Physical Therapy, 21(6), 361-372.

S., A., P., T., A., L., S., G., M., S., & M., V. (2009). Wear behaviour in total ankle replacement: A comparison between an in vitro simulation and retrieved prostheses. Clinical Biomechanics, (8), 661. doi:10.1016/j.clinbiomech.2009.06.006

Saikko, V. (2017). High frequency circular translation pin-on-disc wear testing of UHMWPE using a ball-on-flat contact along a hypotrochoidal track. *Polymer Testing*, *60*149-152. doi:10.1016/j.polymertesting.2017.03.024

Scholes, S. C., Unsworth, A., & Jones, E. (2007). Polyurethane unicondylar knee prostheses: simulator wear tests and lubrication studies. *Physics In Medicine And Biology*, *52*(1), 197-212.

Scholes, S., Inman, I., Unsworth, A., & Jones, E. (2008). Tribological assessment of a flexible carbon-fibre-reinforced poly(ether-ether-ketone) acetabular cup articulating against an alumina femoral head. Proceedings of The Institution Of Mechanical Engineers -- Part H -- Journal Of Engineering In Medicine (Professional Engineering Publishing), 222(3), 273-283.

Scholes, S., & Unsworth, A. (2009). Pitch-based carbon-fibre-reinforced poly (ether-ether-ketone) OPTIMA (R) assessed as a bearing material in a mobile bearing unicondylar knee joint. Proceedings of the Institution of Mechanical Engineers Part H-Journal of Engineering in Medicine, 223(H1), 13-25.

Screw and clearance hole. July 5, 2017. Retrieved from https://www.nmri.go.jp/eng/khirata/metalwork/basic/bolt/index_e.html

Seals, P. (1992). Parker o-ring handbook (ORD 5700). *Parker Seal Group, Lexington, KY*.

Sellam, J., & Berenbaum, F. (2013). Is osteoarthritis a metabolic disease? Joint Bone Spine, 80(6), 568-573. doi:10.1016/j.jbspin.2013.09.007

Single phase to Three Phase VFD Wiring. June 20, 2017. Retrieved from https://www.youtube.com/watch?v=nL-VSw-r4DY

Smith, S. L., Li, L., & Joyce, T. J. (2016). Engineering of a multi-station shoulder simulator. *Proceedings Of The Institution Of Mechanical Engineers. Part H, Journal Of Engineering In Medicine, 230*(5), 470-480. doi: 10.1177/0954411915611161

Socket head screws. July 15, 2017. Retrieved from http://www.sandhuautoengineers.com/socket-head-screws.htm

Synovial joints. August 28, 2017. Retrieved from http://cnx.org/contents/bFtYymxt@4/Synovial-Joints

Tachometer. June 19, 2017. Retrieved from http://www.nidec-shimpokeisoku.jp/en/products/04/02/dt-205z/000.html

Takakura Y, Tanaka Y, Kumai T, et al. (2004). Ankle arthroplasty using three generations of metal and ceramic prostheses. Clin Orthop Relat Res 2004;424: 130–6.

Threading a hole. June 28, 2017. Retrieved from http://web.mit.edu/course/other/machineshop/Drilling/threading.html

VFD Phase Conversion. June 20, 2017. Retrieved from http://www.phasetechnologies.com/phaseconverterinfo/phaseconverter_vfd.htm

Wang, A., Lin, R., Polineni, V., Essner, A., Stark, C., & Dumbleton, J. (n.d). Carbon fiber reinforced polyether ether ketone composite as a bearing surface for total hip replacement. Tribology International, 31(11), 661-667.

Wiring code. June 20, 2017. Retrieved from https://www.allaboutcircuits.com/textbook/reference/chpt-2/wiring-color-codes/

Xin, H., Shepherd, D., & Dearn, K. (2013). A tribological assessment of a PEEK based self-mating total cervical disc replacement. *Wear*, 303473-479. doi:10.1016/j.wear.2013.03.052.

Yang, C., Xu, X., Zhu, Y., Liu, J., & Wei, B. (2016). A Long-Term Study of the Effect of Subtalar Arthrodesis on the Ankle and Hindfoot Joints. *Journal of the American Podiatric Medical Association, 106*(1), 47-53. doi:10.7547/14-002

Ziegler, P., Friederichs, J., & Hungerer, S. (2017). Fusion of the subtalar joint for post-traumatic arthrosis: a study of functional outcomes and non-unions. International Orthopaedics, 41(7), 1387-1393. doi:10.1007/s00264-017-3493-3

Zygo. (2013). *Surface Texture Parameters*. Retrieved from https://www.zygo.com/library/papers/SurfText.pdf